nature methods

Article

https://doi.org/10.1038/s41592-024-02476-3

# Long-term optical imaging of the spinal cord in awake behaving mice

Received: 9 June 2023

Accepted: 16 September 2024

Published online: 12 November 2024

Check for updates

Biafra Ahanonu[1,5], Andrew Crowther[1,5], Artur Kania[2,3], Mariela Rosa-Casillas[4] & Allan I. Basbaum[1]

Advances in optical imaging and fluorescent biosensors enable study of the spatiotemporal and long-term neural dynamics in the brain of awake animals. However, methodological difficulties and fibrosis limit similar advances in the spinal cord. Here, to overcome these obstacles, we combined in vivo application of fluoropolymer membranes that inhibit fibrosis, a redesigned implantable spinal imaging chamber and improved motion correction methods that together permit imaging of the spinal cord in awake behaving mice, for months to over a year. We demonstrated a robust ability to monitor axons, identified a spinal cord somatotopic map, performed months-long imaging in freely moving mice, conducted $Ca^{2+}$ imaging of neural dynamics in behaving mice responding to pain-provoking stimuli and observed persistent microglial changes after nerve injury. The ability to couple in vivo imaging and behavior at the spinal cord level will drive insights not previously possible at a key location for somatosensory transmission to the brain.

Understanding neural computation mechanisms and their relation to perception and behavior necessitates recording neural activity in awake behaving animals, ideally along all points of the neuroaxis. Although almost all studies at the level of the spinal cord have relied on recordings in anesthetized preparations, spinal cord neural activity recordings in the awake behaving animal, although rare[1–4], have clear advantages[5–7]. Awake-state recording performed repeatedly over months makes it possible to track neural circuit activity before, during and after the development of neurological disorders, such as the transition from acute to chronic pain. Long-term optical access to the spinal cord also allows one to observe disease progression in non-neural cells (for example, microglia). Moreover, stimulus–behavior relationships help identify psychophysical thresholds that can be compared with the activity of single neurons. For example, animals do not always respond to every noxious stimulus or elicit the same behavior to the same stimulus. The ability to couple behavior to neural activity at the spinal cord level will provide important insights as to where this variability in pain perception and behavior arises and also introduces an ability to study analgesic manipulations that target spinal circuits.

A major impediment to long-term optical recording is the inevitable postlaminectomy fibrosis, which occurs in both anesthetized and awake preparations. More recent long-term imaging methods have implanted a small metal chamber overlying the spinal cord segment of interest[2,8–11] (Supplementary Note 1). Following laminectomy and adherence of a cover glass over the exposed spinal cord, a continually accessible spinal cord window provided the ability to follow injury-associated axonal regeneration over time[8,12,13]. However, postlaminectomy fibrosis often occurred and frequently necessitated repreparation, with the associated risk of spinal cord damage.

Here, we address experimental and computational challenges that now enable reliable, long-term spinal cord imaging (Fig. 1 and Extended Data Fig. 1a). We demonstrate that polytetrafluoroethylene (PTFE)-based inhibition of the postlaminectomy fibrosis preserves long-term spinal cord window clarity, making it possible to record, for months, from defined populations of spinal cord neuronal and

[1]Department of Anatomy, University of California, San Francisco, CA, USA. [2]Institut de Recherches Cliniques de Montréal, Montreal, Quebec, Canada. [3]Department of Cell Biology and Anatomy, and Division of Experimental Medicine, McGill University, Montreal, Quebec, Canada. [4]Neuroscience Graduate Program, University of California, San Francisco, CA, USA. [5]These authors contributed equally: Biafra Ahanonu, Andrew Crowther.
e-mail: allan.basbaum@ucsf.edu

https://doi.org/10.1038/s41592-024-02476-3

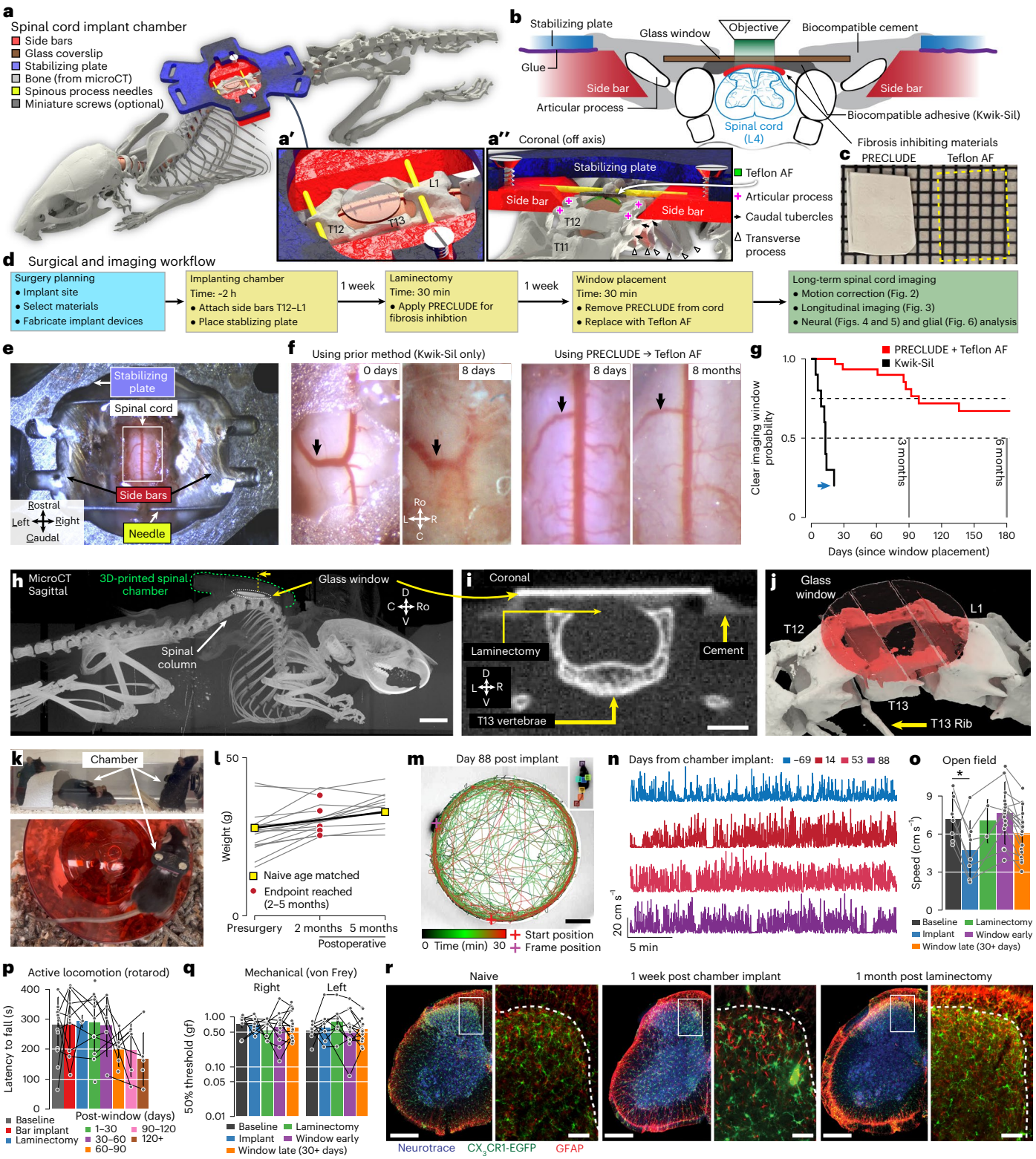


nonneuronal (microglial) cells, without repreparation. Implanted mice display normal locomotion and sensory sensitivity, without evidence of spinal cord pathology. To handle the extensive spinal cord motion, we combined deep learning feature identification[14] and control point registration along with nonrigid diffeomorphic[15] and rigid image registration algorithms[16]. We demonstrate repeated imaging (over months) of large numbers of individual, genetically defined lamina I dorsal horn projection neurons, as well as high-quality imaging of axons (Thy1–green fluorescent protein (GFP) mouse lines and tdTomato expressed in sensory neurons), cell bodies (GFP expression pan-neuronally) and microglia ($CX_3CR1$–EGFP mice). Importantly, this method achieves cellular imaging in behaving mice and is fully compatible with freely moving miniature microscope imaging studies that can investigate not only the transition from acute to chronic pain but also pharmacological interventions and even regeneration after spinal cord injury.

**Fig. 1 | Surgical design and health validation for long-term spinal cord optical access in awake mice. a**, A 3D model of the recording chamber implanted at the T12–L1 vertebrae (skeleton from Extended Data Fig. 3g). **a′**, Optical access to the dorsal spinal cord post T13 laminectomy. **a″**, Side bar placement adjacent to the articular processes and Teflon AF location (green film). **b**, Spinal cord imaging of chamber components. **c**, Two Teflon materials inhibit postlaminectomy fibrosis. **d**, The workflow for long-term imaging includes three surgical steps. **e**, The spinal chamber 1 week after window placement. The anatomy axes abbreviations in all figures: C, caudal; D, dorsal; L, left; La, lateral; M, medial; R, right; Ro, rostral; V, ventral. **f**, PRECLUDE and Teflon AF inhibit fibrosis compared with a silicone-only approach. **g**, Survival curves (Kaplan–Meier estimator) of the fibrosis onset probability of PRECLUDE + Teflon AF ($n = 36$) or only Kwik-Sil ($n = 10$) surgeries (the Kwik-Sil curve is not at zero (blue arrow) as two mice were fibrosis free or deceased at the time of analysis). **h**, Whole-body microCT sagittal max projection after implanting chamber (3D printed radiotransparent material). Scale bar, 5.0 mm. **i**, Coronal slice from microCT, postlaminectomy, shows the intact surrounding bone. Scale bar, 1.0 mm. **j**, A multivertebral 3D reconstruction of microCT data in **h** and **i** confirms T13 window placement and bone integrity. **k**, Normal behaviors after chamber implant. **l**, The weight of chamber-implanted mice ($n = 17$) compared with age-matched controls ($n = 2$). **m**, Open field locomotion (30 min) after chamber implant. Inset: open field tracking markers. Scale bar, 10 cm. **n**, Locomotor speed of **m** pre and post surgery (30-min sessions). **o**, The mean open field locomotor speed comparing naive ($n = 7$) and postsurgery mice at different stages ($n = 7, 2, 18$ and 19). Most mice in **o**–**q** were used for imaging. The bar plot and error bars in **o**–**q** show the mean ± s.d., and gray lines are mice measured across multiple stages. The statistics in **o**–**q** are from one-way ANOVA with Dunnett's post hoc. $^*P < 0.05$. **p**, The mean latency to fall in accelerating rotarod (third trial) comparing naive ($n = 14$) and different postsurgery times ($n = 8, 2, 10, 5, 5, 5$ and 5). **q**, Von Frey mechanical thresholds comparing naive ($n = 9$) and different postsurgery times ($n = 7, 6, 13$ and 19). **r**, L4 microglia ($CX_3CR1$–EGFP) and astrocyte (anti-GFAP) immunofluorescence (100 µm sections). Scale bars, 300 µm and 50 µm (magnified).

## Results

### Spinal chamber design and implant procedures

To gain stable access to the lumbar spinal cord, we fabricated three implant components that together form a spinal chamber used with a redesigned surgical setup (Fig. 1a and Extended Data Fig. 1b–k). Specifically, we use two metal or three-dimensional (3D) printed ~9 × 10 mm pieces (side bars), one on each side of the vertebrae, and a third ~20 × 24 mm piece (stabilizing plate) that connects the side bars over the top, forming an elevated platform across the spinal column (Fig. 1b,c). Although the stabilizing plate design is highly customizable (Extended Data Fig. 1f and Supplementary Note 2), we recommend a wide inner cutout that provides ample working area for the subsequent procedures and at least one handle, in the rostral direction to clamp the animal. To place the chamber over the lumbar enlargement, we recommend designs 4 and 6 in Extended Data Fig. 1f. The combined metal components weigh ~1.3–1.9 g, comparable to material implants developed for head-mounted imaging[17] (Supplementary Video 1).

To achieve a continually accessible window to the lumbar enlargement, we perform three separate surgical procedures (Fig. 1d,e), over 3 weeks, totaling ~5 h of general anesthesia per animal. In the first surgery (2–3 h) (Supplementary Fig. 1 and Supplementary Video 2), we expose and fuse three vertebrae (T12–T13–L1) using the side bars and the stabilizing plate as structural supports. To position the side bars, we first clamp them to the side posts and then, with a micromanipulator, position them against the vertebral wall of T13 (Extended Data Fig. 2a–i), directly below the T12 and L1 dorsal spinous process needles (33G, 0.2-mm OD), which are crucial for implant stability (Extended Data Fig. 2e,f). We manually taper the stainless steel side bars before surgery for paravertebral fitting (Extended Data Fig. 2c). Before freeing the side bars from the clamps, we superglue the 33G needles to the side bars and seal the edges of the incised tissue with sutures and VetBond. We then superglue the stabilizing plate over both side bars, which completes the metal assembly. Subsequent steps fix the bone and implant using resin polymethyl methacrylate (PMMA, C&B Metabond kit). Importantly, we uncover the laminar bone of the middle vertebra (T13) before the PMMA cement sets, allowing for the subsequent laminectomy, which is generally performed 1 week after the chamber implantation (Supplementary Table 1 and Supplementary Fig. 1).

As emphasized above, a major impediment to chronic spinal cord recordings is the postlaminectomy fibrosis, which rapidly obscures the dorsal surface of the spinal cord. Although filling the space directly above the spinal cord with transparent silicone adhesive can abate fibrosis and maintain window clarity for a short period of time[8,9,13], we found that fibrosis impedes long-term imaging of the dorsal horn in ~80% of preparations (Fig. 1f,g and Supplementary Note 3). Unlike silicone-only preparations, here we report that fluoropolymer-based fibrosis inhibition provides clear optical access to the dorsal horn, on both sides of the cord, for greater than 3 months in 75% of preparations (Fig. 1f,g and Extended Data Fig. 1l).

We initially tested a cohort of artificial dura plastic materials for their efficacy and permanence as a dural substitute (Duraseal, Gelfoam and ePTFE). The synthetic fluoropolymer, ePTFE (Gore Medical, GORE PRECLUDE membrane; Extended Data Fig. 2j) stood out, inhibiting fibrotic and dural regrowth for months. A major limitation, however, is that the GORE PRECLUDE membrane is opaque (Fig. 1c), which is incompatible with optical imaging. In its place, we identified an amorphous synthetic fluoropolymer, Teflon AF 2400 (Fig. 1c and Extended Data Fig. 2k), which when placed over the spinal cord also displayed long-term regrowth inhibitory properties (Fig. 1f). As Teflon AF has a visible and near-infrared (NIR) refractive index of $n_{TAF} \approx 1.28–1.29$ compared with nervous system tissue of $n_{brain} \approx 1.35–1.38$ (ref. 18) and water of $n_{water} \approx 1.33$, we predicted that Teflon AF would minimally affect optical access and imaging quality, which we confirmed by one- and two-photon imaging of 1 µm fluorospheres on glass slides

**Fig. 2 | Computational correction of spinal cord motion in awake mice.** **a**, Imaging a large spinal cord field is subject to various motion artifacts. **b**, The modular motion correction pipeline that addresses issues outlined in **a**: correct large rostrocaudal movement using LD-MCM with deformation and cross-session correction using displacement fields and CS-MCM. **c**, LD-MCM utilizes deep learning to identify features that are used to register frames to a reference frame. Point clouds in the reference frame show per frame rostrocaudal and mediolateral motion (2.31 min, 20 Hz). Inset: markers on distinct vasculature features. Scale bar, 300 µm. **d**, Mean projection images (all frames) for the raw movie and after TurboReg or LD-MCM. The arrows indicate features seen only in LD-MCM (yellow) and partially visible after TurboReg (white). Scale bar, 300 µm. **e**, Point clouds of per frame rostrocaudal and mediolateral movement of feature 3 (session as in **c**, 2.31 min, 20 Hz) after TurboReg, NoRMCorre and LD-MCM (black arrow). **f**, Rostrocaudal displacement relative to the median location in the raw and motion corrected movies over all features ($n = 2$ mice, statistics based on ten movies total). The box plots in all figures display the first, second (median) and third quartiles, with whiskers indicating 1.5× the interquartile range. Outliers are omitted. The statistics in **f** and **k** are from one-way ANOVA with Dunnett's post hoc. $^*P < 0.05$, $^{**}P < 0.01$ and $^{***}P < 0.001$. **g**, A synthetic image (116 × 77 pixels) before and after registration using displacement fields (the red vectors indicate orientation and magnitude, 5× subsampled and magnitude scaled for display purposes). **h**, Displacement field motion correction (as in **g**) in an example frame from one-photon fluorescence imaging of spinal cord GCaMP6s-expressing neurons (mouse in Fig. 5d). The yellow arrows indicate postregistration aligned features. Scale bar, 300 µm. **i**, Mean projection images (first 5,000 frames, ~12.5 min, 20 Hz) before and after (the yellow arrows indicate stable features) motion correction. Scale bar, 300 µm. **j**, The 2D correlation (corr) coefficient of all frames to the mean frame of the movie (as in **i**) before and after each method. Inset: a histogram of correlation coefficients across all frames. **k**, A box plot summarizing the results, as in **j** ($n = 2$ mice, statistics based on three movies).

https://doi.org/10.1038/s41592-024-02476-3

(Extended Data Fig. 2l–o). To skip the intermediate PRECLUDE membrane step entirely, we attempted Teflon AF placement immediately after laminectomy, but this approach provided less fibrosis inhibition. Applying a hydrophilic surface coating to Teflon AF may improve its effectiveness in the postlaminectomy period, similar to reports of polyethylene-oxide-coated CYTOP (PEO-CYTOP), an amorphous synthetic fluoropolymer, which has been used in cranial imaging[19] (Supplementary Note 3). However, for a strategy that does not require sophisticated material fabrication, we applied the microporous PRECLUDE membrane immediately after laminectomy and then swapped for the Teflon AF membrane during window placement.

In the second surgical procedure (0.5–1 h) (Supplementary Fig. 2, Supplementary Table 2 and Supplementary Video 3), we expose the spinal cord (L4/5) by laminectomy of the middle vertebra (T13). Using fine forceps, we delicately incise the dura and then place GORE PRECLUDE over the exposed cord, surround it with a gelatin sponge

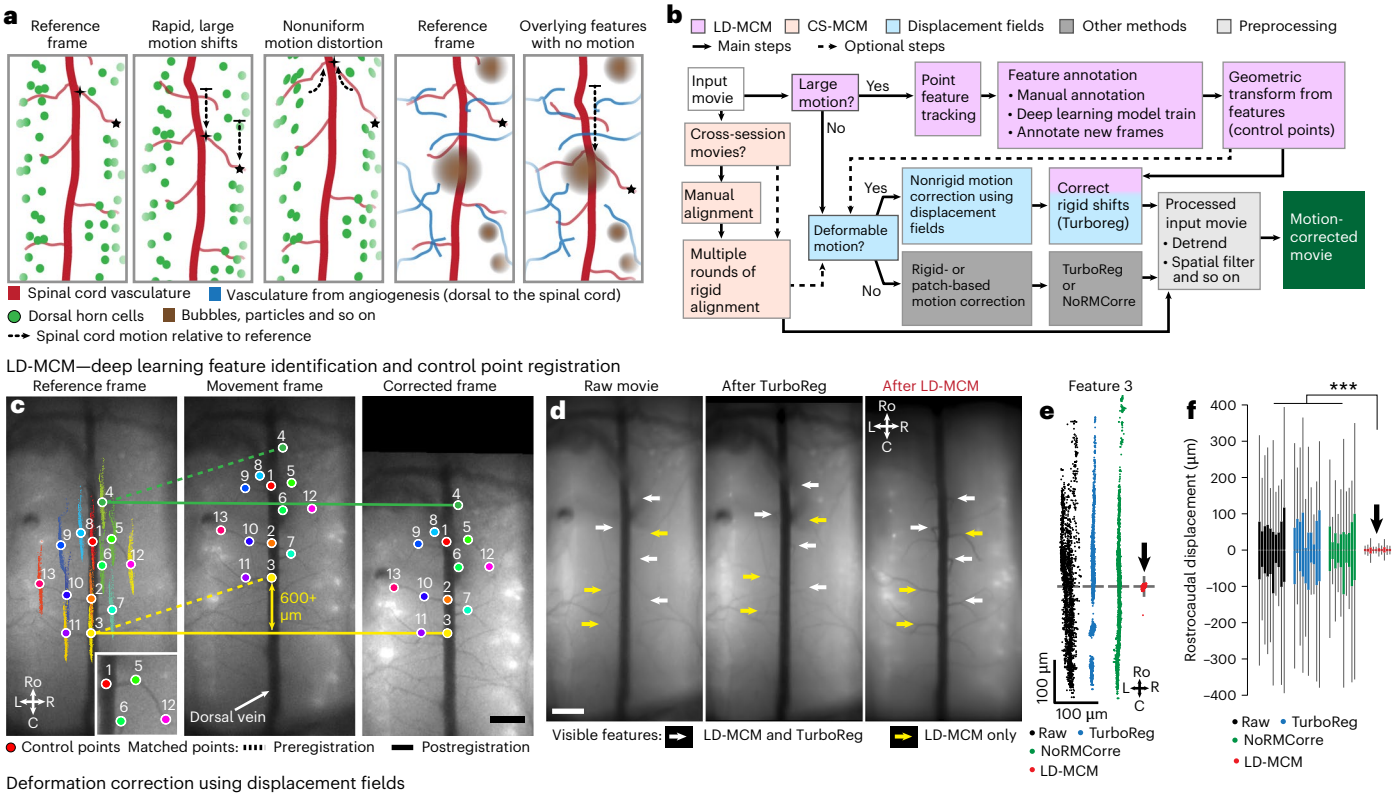

and set PRECLUDE in place with Kwik-Sil. Although we typically proceed to the third step within a week, this procedure can be performed up to a month after placing the PRECLUDE membrane (Supplementary Note 4).

In the final surgical procedure (0.5–1.0 h) (Supplementary Fig. 3, Supplementary Table 3 and Supplementary Video 4), we swap out the opaque PRECLUDE Teflon for the transparent form, Teflon AF 2400. We then set a #0 glass coverslip over the Teflon AF using Kwik-Sil as an adhesive between these layers. Finally, we stabilize this configuration with bone cement. With the Teflon AF material set and sealed from the environment, the window provides long-term optical access to the dorsal spinal cord (Fig. 1f,g). The materials needed for all procedures are detailed in Supplementary Notes 5 and 6 and Supplementary Table 4.

### Preserved behavior and spinal cord integrity post-implant

Noninvasive imaging modalities (for example, functional magnetic resonance imaging (MRI)) can be combined with fluorescence (for example, $Ca^{2+}$) imaging[20]. However, most existing spinal cord implant devices use materials that are incompatible with MRI or micro X-ray computed tomography (microCT) (Extended Data Fig. 3a–d). We identified certain 3D printed materials, for example, FormLab's Surgical Guide and BioMED clear resins, that are bio- and microCT-compatible (Extended Data Fig. 3e,f). Attaching stabilizing plates to the side bars with adhesives, instead of metallic miniature screws, also improves microCT compatibility (Extended Data Fig. 3g–i and Supplementary Video 2). To verify the laminectomy and spine structural integrity, we performed the implant surgery and laminectomy, then conducted microCT imaging (Fig. 1h–j and Supplementary Videos 5 and 6). The 3D-printed side bars and stabilizing plate did not occlude bone or soft tissue. Future studies can use contrast agents or MRI to visualize the spinal cord and dorsal root health and anatomy over time.

Postoperative weight did not decline at 2 or 5 months ($n = 22$ mice; Fig. 1k,l and Extended Data Fig. 3j). After the final surgery, the implanted mice achieved similar open field speeds as their presurgery baseline (Fig. 1m–o, Extended Data Fig. 3k and Supplementary Video 7) and can repeatedly perform the rotarod task, with a trend toward decreasing performance after 2 months (Fig. 1p and Extended Data Fig. 3l). Importantly, implanted mice displayed normal mechanical sensitivity for months after surgery (Fig. 1q).

Postmortem examination of the lumbar enlargement did not reveal histopathological signs due to the implant unless signs of fibrosis were present (Fig. 1r and Extended Data Fig. 4a–c). Between 2 and 5 months after implantation, we only observed fibrosis development in 6 of 26 preparations. These mice with fibrosis showed spinal cord pathology (Supplementary Fig. 4) accompanied by various behavioral signs (paralysis, altered gait and skin lesions). At time points after laminectomy, we did observe expected astrogliosis at the surface of the cord; however, within the dorsal horn, signs of microgliosis, evidenced by microglial reporter expression, were only transiently above normal (Extended Data Fig. 4c).

### Motion correction of the spinal cord in awake mice

Awake-state spinal cord recordings have challenges compared with recordings in the brain: locomotion-driven spinal cord movement leading to rapid, large rostrocaudal shifts (>650 µm in certain mice within and across sessions), rapid nonrigid deformations of the field of view (FOV) and presence of obstacles—such as neovascularizations, bubbles and so on—that move differently from the primary tissue of interest (Fig. 2a). Here, we developed and validated a multistep, hierarchical workflow (Fig. 2b). The workflow consists of a large displacement motion correction method (LD-MCM), a modification of an existing nonrigid motion correction method and a semi- or fully automated cross-session motion correction method (CS-MCM).

To automate the correction of large rostrocaudal shifts, LD-MCM uses deep learning (for example, DeepLabCut[21]) to track features followed by control point and rigid registration (Fig. 2c). Although image alignment can be done using feature detectors[22], spinal cord imaging movies contain varied features across multiple focal planes. As a result, these methods can identify nonrelevant features. Here, we manually annotated vasculature features in movies, then trained deep learning models that tracked consistent vasculature as a proxy for spinal cord motion (Extended Data Fig. 5). We found that LD-MCM significantly improved motion correction in spinal cord imaging movies compared with widely used TurboReg[16] or NoRMCorre[23] methods ($P < 0.0001$, post hoc Dunnett's test LD-MCM compared with TurboReg/NoRMCorre (ten movies from two mice); Fig. 2d–f and Supplementary Video 8). With minimal training (20 frames from one session), we can consistently identify vasculature features and correct motion across months of imaging (Extended Data Fig. 5g) and need only six to ten features to achieve high accuracy (Extended Data Fig. 5h–j).

To handle nonrigid motion, we adapted displacement field-based registration based on Maxwell's Demons[15,24]. These techniques can lead to the registration of movies containing a mix of deformations and spatial shifts of features in the imaging FOV (Fig. 2g,h) and have been used in brain $Ca^{2+}$ imaging[25]. This nonrigid method implemented for the spinal cord imaging movies in awake mice significantly ($P = 0.0105$ (LD-MCM versus TurboReg) and $P = 0.0009$ (LD-MCM versus NoRMCorre), post hoc Dunnett's test, three movies from two mice) improved registration compared with TurboReg and NoRMCorre (Fig. 2i–k, Extended Data Fig. 6 and Supplementary Video 9).

To compare imaging across sessions, we developed a multistep motion correction protocol. This protocol involved manual correction for large shifts, rotations and other FOV changes (for example, horizontal or vertical mirroring) followed by multiple rounds of rigid registration, which led to improved alignment (Fig. 3a–e). We also employed a modified LD-MCM protocol to track individual features across months to over a year (Supplementary Video 10).

### Long-term optical access in behaving mice

Animal attachment to the imaging setup typically takes less than a minute, aided by the use of clamps (Fig. 3a) and the fact that mice do not need to be anesthetized. To reduce lateral movements by the animal while maintaining camera visibility of mice, we placed the mice in an imaging apparatus with infrared transmitting acrylic blinders. This apparatus reduced the strain on the implant produced by excess lateral animal motion and enabled hours-long sessions in this setup. To maximize the signal-to-noise ratio (SNR) while maintaining an exposure of ≤10 ms, which minimizes motion blur (Extended Data Fig. 7a) and thus improves motion correction, we optimized several aspects of the preparation (Supplementary Notes 7–9) on the basis of our prior awake animal imaging apparatus[26].

Absent injury, ascending and descending axons should be intact. Therefore, to demonstrate long-term optical clarity, we recorded axonal GFP expression in Thy1–GFP mice for months to over a year (Fig. 3a–c and Supplementary Video 10). During these long-term recordings, in some mice the spinal cord would shift tens to hundreds of micrometers and stay stable around the new position, regardless of animal motion on a given day (Fig. 3d). To correct for these shifts, we used CS-MCM and confirmed stable image quality and fluorescence intensity with one- or two-photon imaging up to ~1.5 years (557 days) of imaging (Fig. 3e–h and Extended Data Fig. 7b,c). Repeated awake imaging of the same animal is stable across dozens to hundreds of recording sessions (>260 sessions; Supplementary Fig. 5).

Long-term awake imaging of the spinal cord enables monitoring of protein expression over time—including changes after injury and during disease progression—without the confounds of anesthesia and with detailed spatiotemporal information. Here, we monitored green (nuclearly localized GFP) and red (tdTomato) fluorescent proteins after retro-orbital injection of AAV-PHP.eB-CAG-NLS-GFP and AAV-PHP.S-CAG-tdTomato (Fig. 3i–m), which preferentially target central and peripheral nervous systems, respectively[27]. We primarily

https://doi.org/10.1038/s41592-024-02476-3

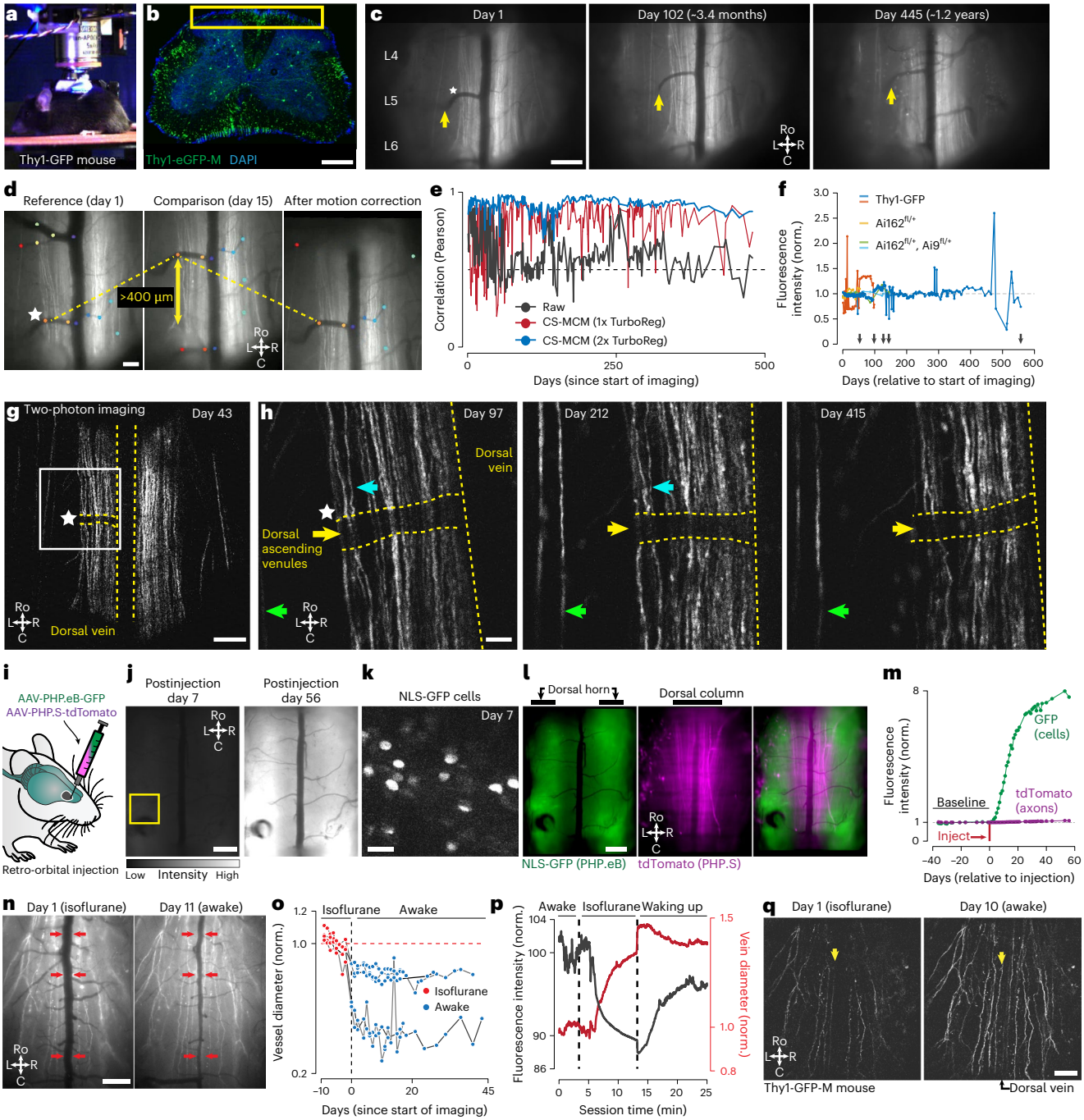


**Fig. 3 | Long-term axonal and neuronal cell body imaging in awake mice.** **a**, A chamber-implanted mouse for one- and two-photon imaging. **b**, Thy1–GFP$^+$ dorsal column axons (100-µm coronal section). The yellow box shows the approximate region imaged in Fig. 3. Scale bar, 300 µm. **c**, One-photon imaging over ~1.2 years in a behaving Thy1–GFP mouse. The yellow arrows show the dAV. The white star in **c** and **d** is the same dAV as in **g** and **h**. Scale bar, 300 µm. **d**, Frames from two different imaging sessions in a Thy1–GFP mouse (as in **c**). The yellow arrow indicates rostrocaudal shifts that can occur during long-term imaging. The colored dots show vascular features used for motion correction. Scale bar, 100 µm. **e**, Pearson correlation to the mean frame of raw movie after CS-MCM. **f**, Fluorescence intensity of Thy1–GFP and background (Ai162$^{fl/+}$; Ai9$^{fl/+}$) mice ($n = 5$) normalized (norm.) by mean intensity across equivalent acquisition cameras. The gray arrow shows the animals' last imaging session. **g**, Two-photon fluorescence imaging of GFP$^+$ axons 43 days after starting imaging. Scale bar, 200 µm. **h**, Magnification of the white box in **g** over time. Similar color arrows identify axons common across sessions. Scale bar, 50 µm. **i**, Retro-orbital virus injection enables concurrent imaging of dorsal horn neurons (GFP) and dorsal column axons (tdTomato). **j**, One-photon imaging of GFP expression in the spinal cord over time after retro-orbital injection. The yellow box is magnified in **k**. Scale bar, 300 µm. **k**, Two-photon imaging of nuclear localization signal (NLS)-tagged GFP in the dorsal horn. Scale bar, 100 µm. **l**, One-photon, simultaneous imaging of NLS–GFP$^+$ dorsal horn neurons and tdTomato$^+$ dorsal column axons. Scale bar, 300 µm. **m**, GFP and tdTomato fluorescence (mouse in **j**–**l**) normalized to baseline. **n**, Imaging under 2% isoflurane versus awake Thy1–GFP mouse. The red arrows show the reduced dorsal vein diameter in the awake mouse. Scale bar, 300 µm. **o**, Vessel diameter (normalized per animal to isoflurane baseline sessions) in anesthetized or awake mice ($n = 5$, gray lines from Thy1–GFP, $CX_3CR1$–GFP and Phox2a–Cre; Ai162 mice). **p**, Vessel diameter and whole-frame fluorescence (normalized to 4 min awake baseline) within a single imaging session (Thy1–GFP mouse as in **n**) before, during and after anesthesia (2% isoflurane). **q**, Two-photon imaging of midline Thy1–GFP$^+$ axons in the awake compared with anesthesia imaging (yellow arrows show a single animal). Scale bars, 300 µm.

https://doi.org/10.1038/s41592-024-02476-3

observed upregulated GFP expression in the dorsal horn and, with two-photon imaging, verified nuclear expression of the construct (Fig. 3k). TdTomato expression also increased over time, including in presumed primary sensory axons in the dorsal columns (Fig. 3l, Extended Data Fig. 7d,e and Supplementary Video 11). This indicates that our approach can be used to conduct simultaneous imaging of spinal neurons and sensory neuron inputs using appropriate green and red calcium indicators.

Anesthesia alters vascular dynamics in addition to neural activity; for example, isoflurane causes vasodilation[28]. Such dilation

**Fig. 4 | Somatotopy and freely moving neural activity identified using large-scale spinal cord imaging. a**, Bulk expression of GCaMP6s throughout the spinal cord dorsal horn achieved after intraspinal injection of AAV2retro-hSyn-Cre virus (AAV2retro-) into Ai9 and Ai162 (Cre-dependent tdTomato and GCaMP6s) mice. **b**, Neuronal GCaMP6s and tdTomato expression in the sacral spinal cord after the procedure in **a**, showing a representative section from a single experiment. Scale bar, 100 µm. **c**, A 3D model of the vertebral-fixed setup for neural and behavior imaging along with stimulus delivery. **d**, Bilateral spinal cord imaging using one-photon microscopy. Miniscope 1 is Inscopix nVista, Miniscope 2 is Open Ephys Miniscope v4.4 and Miniscope 3 is Inscopix LScape module for nVue 2.0. **e**, Tail pinch induces bulk GCaMP6s fluorescence and locomotion. The arrow shows the session time point in **g**. Scale bar, 300 µm. **f**, Stimulus-evoked dorsal horn GCaMP6s fluorescence under minimal locomotion conditions. The arrow is as in **e**. Scale bar, 300 µm. **g**, Neural activity (GCaMP6s, whole-frame fluorescence) aligned to locomotion, body part movement (heat map) and force of pinch (force-sensitive resistor) applied to the tail (T) or back (B) or by innocuous tactile stimulation to the forepaw (F). The numbers below heat map highlight when (1) neural activity correlated with increased behavior, and (2) the stimulus did not induce locomotion, but there was head movement. The white stars show time points without usable tracking. **h**, A schematic illustrating location of body parts stimulated in **i**–**k**. Inset: **h′**, the dorsal horn primary afferent terminal map[29,30,32]. **i**, A mean projection image from one-photon imaging of GCaMP6s mouse (as in **a**) recorded in **j** and **k**. Scale bar, 200 µm. **j**, Neural activity (GCaMP6s, mean projection image) in response to pinch of different body parts. Scale bar, 300 µm. **k**, Neural activity (GCaMP6s) maps from **j** superimposed to show dorsal horn somatotopy. Scale bar, 300 µm. **l**, An image of a mouse with a spinally mounted miniature microscope. **m**, Open field activity during freely moving spinal cord imaging (124.8 min). **n**, Spinal cord imaging of GCaMP6f and tdTomato in a freely moving mouse across >9 months (267 days since start of imaging, 308 days after window placement) from a Phox2a–Cre; Ai148; Ai9 mouse. The yellow arrows show the vasculature or cell bodies matched across sessions. Scale bar, 300 µm. **o**, Active cells (GCaMP6s, Phox2a–Cre; Ai162 mouse) in response to noxious (nox.) cold stimulus. Scale bar, 300 µm.

of the midline spinal cord dorsal vein and dorsal ascending venules (dAVs) could alter optical access to underlying gray and white matter. To compare the influence of anesthesia on dorsal vein diameter, we imaged the spinal cord under both anesthesia and awake behaving conditions (Fig. 3n). As expected, the dorsal vein diameter was larger under isoflurane anesthesia (Fig. 3o and Extended Data Fig. 8a,b). When imaging the anesthetized and awake states in the same session, we observed that isoflurane induced a rapid and smooth reduction in fluorescence intensity, which correlated with the increased vascular diameter ($R^2 = 0.98$ during induction of general anesthesia; Fig. 3p, Extended Data Fig. 8c–e and Supplementary Video 12). Emergence from isoflurane led to a return of the fluorescence toward baseline. Two-photon imaging in the awake state revealed additional Thy1–GFP axons, not detected during anesthesia (Fig. 3q).

To directly assess the topographic organization of inputs into the lumbar enlargement[29–32], we used bulk $Ca^{2+}$ imaging of neurons in the lumbosacral dorsal horn (Fig. 4a–c) and we took advantage of the large FOV provided by the spinal window (Fig. 4d). We tracked individual body parts (Extended Data Fig. 9a–d) and found that mice showed consistent behavioral responses to tail stimulation, but at times we observed $Ca^{2+}$ transients in the absence of stimulus-induced locomotion (Fig. 4e–g). We observed a somatotopic organization of the $Ca^{2+}$ imaging responses to tail and hindlimb stimulation, with a rostrocaudal and mediolateral orientation that is consistent with termination zones of primary afferents (Fig. 4h–k and Supplementary Video 13). This approach is particularly relevant to studies of the reorganization of afferent inputs, for example, after peripheral nerve injury[33–35].

Animals exhibit many nocifensive[36,37] and itch-related[38] behaviors that are state dependent (for example, grooming, sleeping and so on)[39]. Many of these behaviors are more likely to, or can only, occur in freely moving animals. We monitored the behavior of freely moving mice while conducting bilateral spinal cord imaging of $Ca^{2+}$ dynamics or static fluorescence during hours-long recording sessions (Fig. 4l–m and Extended Data Fig. 9e–q) and for months (for example, >8 months; Fig. 4n–o) as mice received pain-provoking stimuli. Our approach can be used to study complex behavior dynamics in long-term studies of injury or analgesic efficacy.

Spinal imaging in awake mice is key to understanding the neural code that spinal cord projection neurons (SCPNs) transmit to the brain. Using a transgenic approach combining the SCPN-biased Cre-driver line (Phox2a–Cre[40]) and a Cre-dependent GCaMP6s line (Ai148 or Ai162 (ref. 41)), we gained access to $SCPN^{Phox2a}$ throughout lamina I of the dorsal horn (Fig. 5a,b and Supplementary Fig. 4b). Using one-photon microscopy, we consistently imaged these superficially located neurons for months ($n = 6$ mice; Fig. 5c). To address the longstanding question about the polymodality of lamina I SCPNs, we applied different noxious stimuli while monitoring animal behavior. We identified animal body parts with DeepLabCut and processed GCaMP6s/f movies using CIAtah[26]. With this approach, we observed increased neuronal activity that coincided with escape-related behavior and/or head movements (Fig. 5d and Supplementary Video 14). As expected, responses were consistent across repeated applications of the same stimulus (Extended Data Fig. 10a–d) and the side of the spinal cord ipsilateral to the stimulated hindpaw showed increased activity relative to the contralateral side (Fig. 5d,e and Extended Data Fig. 10e–h). On multiple occasions, however, we observed $SCPN^{Phox2a}$ activity in awake mice contralateral to the stimulated hindpaw (Fig. 5f and Extended Data Fig. 10c,d). We also consistently found $SCPN^{Phox2a}$ activated during animal motion, whether or not we delivered a stimulus, an observation of particular interest as lamina I SCPNs do not directly receive innocuous tactile or proprioceptive input in uninjured animals (Fig. 5f and Extended Data Fig. 10c,d). Occasionally,

**Fig. 5 | Long-term bilateral imaging of spinal cord dorsal horn neural activity in awake mice. a**, The genetic approach to image activity of individual SCPNs ($SCPN^{Phox2a}$) that express GCaMP6s/f and/or tdTomato in Phox2a–Cre; Ai162/Ai148; Ai9 mice. **b**, Left: GCaMP6s and tdTomato in dorsal horn $SCPN^{Phox2a}$ (50-µm-thick coronal sections), representative sections from a single experiment. Right: magnification of the white box. Scale bars, 300 µm (left) and 100 µm (right). **c**, One-photon fluorescence intensity over time in $SCPN^{Phox2a}$-GCaMP6s mice ($n = 6$), normalized (norm.) as in Fig. 3f. **d**, Simultaneous monitoring of behavior (yellow boxes, body part tracking) and L4–L6 spinal cord neuronal activity 214 days after the first imaging session. **d′**, Neural activity (GCaMP6s) in individual $SCPN^{Phox2a}$ in response to noxious heat (L, left hind paw) from the raw and $\Delta F/F$ movies. **d″**, Noxious stimulus-induced locomotion and head movement. Scale bar in **d′**, 500 µm. **e**, $SCPN^{Phox2a}$ neural activity (GCaMP6s) from mice responding to stimuli under anesthesia (2% isoflurane) or while awake. U, hindpaw suction. **f**, $SCPN^{Phox2a}$ neural activity (GCaMP6s, as in **d**) during stimulus application (black arrows). **g**, Locomotion and body part speed (heat map, tracking as in **d**) aligned to $SCPN^{Phox2a}$ neural activity (GCaMP6s) and stimuli as in **f**. The numbers below the heat map indicate (1) head movement correlated $SCPN^{Phox2a}$ activity, (2) stimulus-induced locomotion and ipsilateral-only $SCPN^{Phox2a}$ activity, (3) poststimulus pause in behavior after ipsilateral $SCPN^{Phox2a}$ activity followed by movement that correlates with secondary burst of $SCPN^{Phox2a}$ activity, (4) sound-induced locomotion with minimal $SCPN^{Phox2a}$ activation and (5) ipsilateral-only $SCPN^{Phox2a}$ activity after heat stimuli. **h**, $SCPN^{Phox2a}$ aligned across anesthetized (day 8) or awake animal imaging sessions (median filtered cell images from CELLMax). **h′**, Magnification of three cells tracked from day 8 to 123. Scale bars, 100 (**h**) and 50 (**h′**) µm. **i**, $SCPN^{Phox2a}$ neural activity (GCaMP6s), as in **h**, to noxious stimuli across ~4 months. Each row indicates a neuron aligned across time; the summaries on the right show the mean post- (0 to 2 s) minus pre- (−4 to −0.25 s) stimulus response across all days for the same neurons.

https://doi.org/10.1038/s41592-024-02476-3

the mice exhibited minimal escape-like nocifensive behavior, yet we still observed robust SCPN$^{Phox2a}$ activity. Tracking of individual animal body parts helped identify instances in which head movement without locomotion correlated with SCPN$^{Phox2a}$ activity (Fig. 5g). Importantly, a subset of SCPN$^{Phox2a}$ consistently responds to the same stimulus across weeks to months (Fig. 5h,i, Extended Data Fig. 10i,j and Supplementary Video 15). In contrast to consistent contralateral activity in the awake preparation, we observed only ipsilateral-side SCPN$^{Phox2a}$ activity in anesthetized preparations (Fig. 5e, Extended Data Fig. 10e–h and Supplementary Fig. 6). Further, we did not observe spontaneous activity

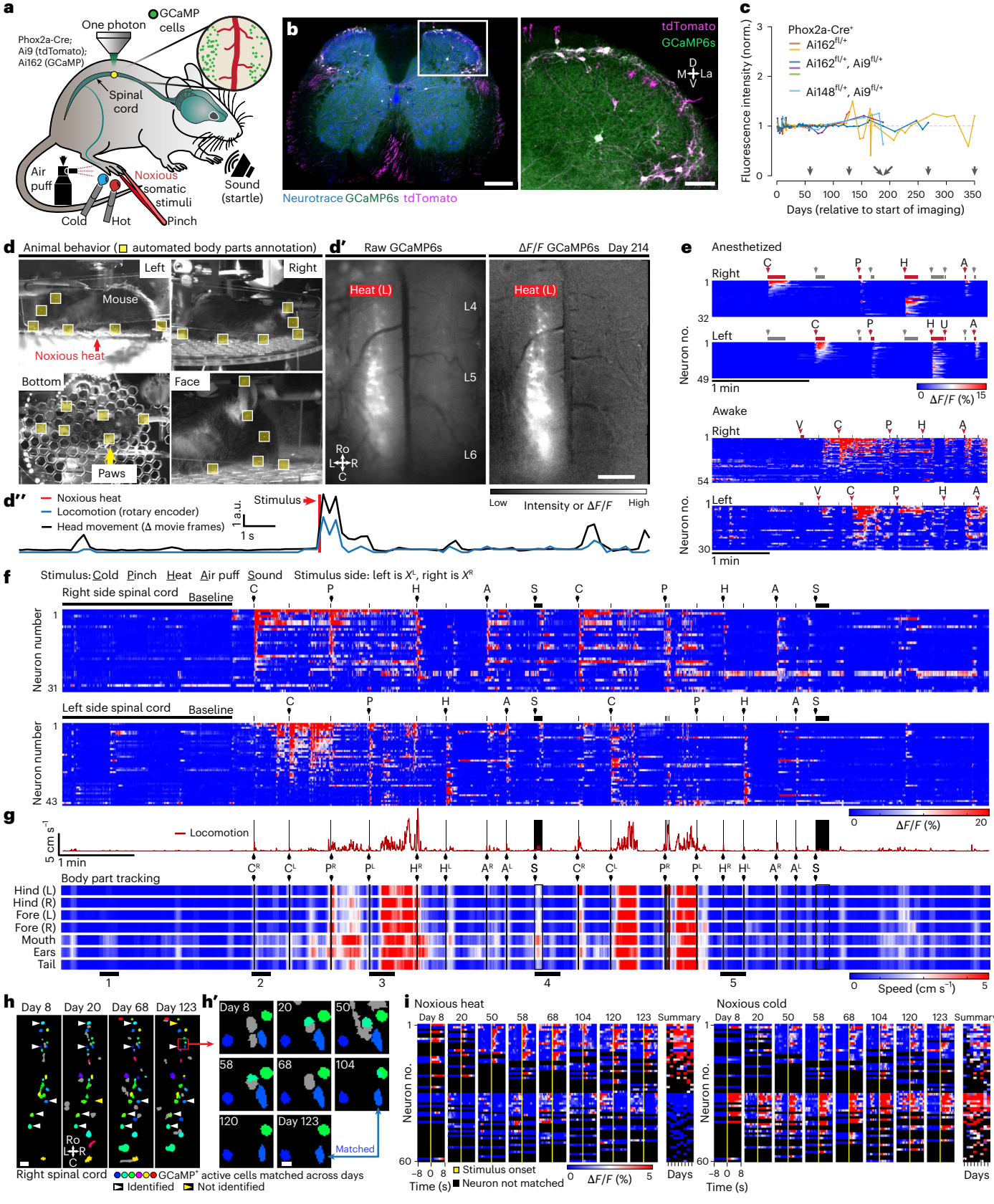

https://doi.org/10.1038/s41592-024-02476-3

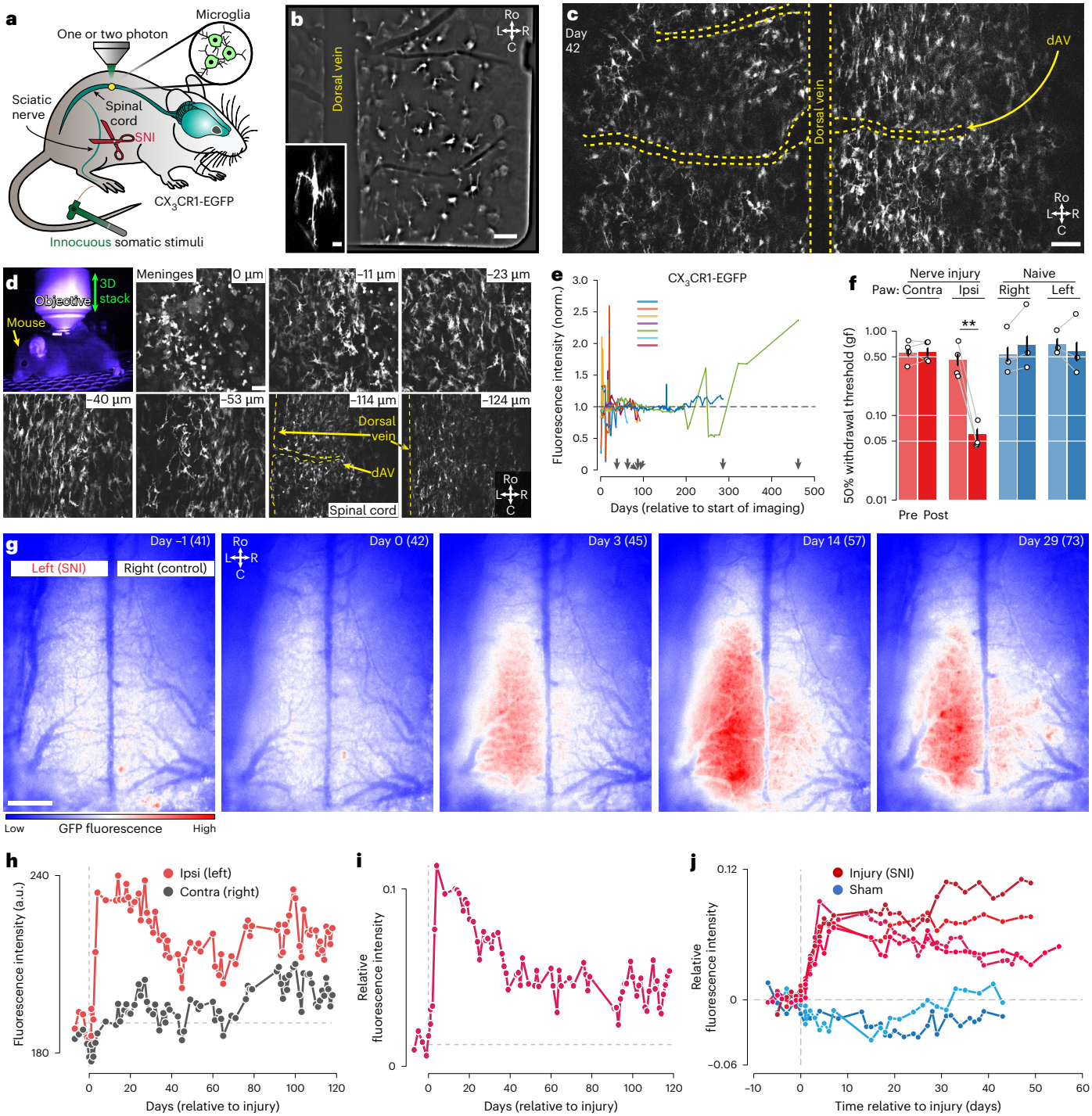


**Fig. 6 | Long-term imaging of spinal cord microglia before and after injury in awake mice. a**, The strategy for longitudinal imaging of microglia ($CX_3CR1$–EGFP) before and after inducing a neuropathic pain model (SNI[36]). **b**, A one-photon mean projection image (816 s, 1 Hz movie, bandpass filtered) of $EGFP^+$ microglia in an acute spinal preparation. Inset: two-photon image of a single microglial cell. Scale bar, 50 µm and 20 µm (inset). **c**, Two-photon fluorescence imaging (20×/1.0 NA objective, single plane montage of left and right spinal cord) of $EGFP^+$ spinal microglia in an awake mouse. Scale bar, 50 µm. **d**, Multiplane, two-photon imaging of monocytes (meninges, top left) and microglia (spinal cord, bottom right) in an awake mouse. Scale bar, 50 µm. **e**, Fluorescence intensity of the spinal cord parenchyma over time in $CX_3CR1$–EGFP mice ($n = 7$), normalized as in Fig. 3f. **f**, Mechanical sensitivity (von Frey method) of naive ($n = 3$ mice) or injured ($n = 4$) mice in **g**–**j**. Each dot is the mean of each animal's thresholds before (pre) or after (post) surgery (SNI) or in an anesthesia-only procedure (naive). The bar plot and error are mean ± s.d. The statistics in **f** are from one-way ANOVA with Dunnett's post hoc. $^{**}P < 0.01$. **g**, One-photon fluorescence imaging of spinal cord microglia EGFP intensity before and after left-side SNI. The numbers in parentheses are the imaging session days relative to the start of imaging of this mouse. Scale bar, 300 µm. **h**, Fluorescence intensity (a.u., constant imaging parameters) of each side of the spinal cord, before and after injury in a $CX_3CR1$–EGFP mouse, as in **g**. Vertical and horizontal dashed gray lines in **h**–**j** indicate day of injury (day 0) and the mean baseline intensity, respectively. **i**, The relative GFP fluorescence intensity (same mouse as in **g** and **h**) is defined as $(I - C)/(I + C)$ where $I$ and $C$ are the mean intensity on the ipsi- (injured) and contralateral side of the cord. **j**, Relative intensity, same as in **i**, for injured ($n = 4$) and naive ($n = 2$) mice.

in the anesthetized preparation, underscoring the importance of recordings in the awake mouse.

In the context of pain, spinal cord microglia proliferate and undergo changes in molecular composition and morphology[42–44]. Using $CX_3CR1$–EGFP mice[45], we monitored microglia changes long term, before and after inducing a neuropathic pain model (spared nerve injury (SNI))[36,46] (Fig. 6a). The $CX_3CR1$–EGFP line expresses enhanced green fluorescent protein (EGFP) in all monocytes, including microglia, in the meninges and spinal cord parenchyma. One- and two-photon in vivo imaging confirmed the morphological features of the different monocyte populations in both acute and long-term preparations (Fig. 6b–d, Supplementary Fig. 7 and Supplementary Video 16). Using one-photon imaging, we tracked microglial EGFP expression across months (Fig. 6e). After inducing SNI, we observed persistent mechanical hypersensitivity in the injured cohort (Fig. 6f) and imaged experimental ($n = 4$) and control ($n = 3$) mice. Consistent with cross-sectional analyses in histochemical preparations after SNI[43], $CX_3CR1$–EGFP fluorescence increased ipsilateral to the injury (Fig. 6g,h). The difference in EGFP intensity between the two sides of the cord persisted for over 4 months, with a clear increase ipsilateral to the nerve injury by 3 days post-SNI (Fig. 6i–j and Supplementary Video 17). Interestingly, over time, we detected increased fluorescence contralateral to the nerve injury, an observation that may be relevant to the contralateral spread of pain in patients with, for example, complex regional pain syndrome[47,48].

## Discussion

We have demonstrated surgical, experimental and computational methods that overcome major limitations to long-term spinal cord imaging in awake behaving mice. By incorporating fluoropolymer membranes, which provide long-term fibrosis regrowth inhibition, we reliably maintain clear optical access to the spinal cord for months. We envision that these fluoropolymers (PRECLUDE and Teflon AF 2400) will also improve the longevity and health of cranial windows and suggest that the Kaplan–Meier fibrosis onset curves be routinely used to display changes or improvements to spinal cord imaging and other preparations.

There is complex and large spinal cord motion during awake behaving spinal cord imaging. To correct this motion, we developed an image registration pipeline that combines deep learning control point feature tracking (LD-MCM), deformation-based nonrigid, rigid and cross-session (CS-MCM) methods. The pipeline is available within CIAtah, our existing $Ca^{2+}$ imaging analysis pipeline[26,36]. To improve usability and robustness, our pipeline can be extended and further automated using advances in zero-shot foundational models[49,50], large-language model-guided feature annotation[51] and self-supervised machine vision methods[52]. This approach can be combined with simultaneous multicolor imaging of fluorescent fiducial markers placed on the spinal cord, which will allow improved LD-MCM and CS-MCM correction, enabling improved cross-day cell matching[53]. Improved speed and numerical accuracy of nonrigid motion correction can also be achieved by integrating deformation-based methods that are more computationally efficient and mass preserving[54]. To date, our design enables imaging from the superficial dorsal horn continuously in the awake behaving mouse. However, we anticipate that advances in optical and computational techniques combined with our imaging approach will allow routine imaging and analysis of deep dorsal horn cells. These techniques include three-photon imaging[55], kilohertz two-photon imaging[56], adaptive optics[57], targeted illumination[58] and their integration[59].

We demonstrate long-term, bilateral imaging in freely moving mice using advances in miniature microscope designs[60,61], broadening the repertoire of behaviors that we can correlate with spinal cord neuronal or glial activity. By monitoring the activity of the same population of neurons, as well as nonneural cells, before, during and after injuries, we are now able to address longstanding questions about the transition from acute to chronic pain in the awake behaving mouse. Of particular interest will be tests of the effects of existing and novel analgesics[62,63] across different stages of disease progression.

As expected, we found that isoflurane anesthesia reduces the excitability of dorsal horn neurons. Particularly notable was the spontaneous activity in the awake preparation and the reduced response of neurons in the anesthetized state. Neural activity contralateral to the side of stimulation in the awake state was readily apparent and clearly contrasted the minimal or nonexistence of stimulus-evoked contralateral activity under anesthesia. How the emergence of these commissural neural dynamics in the awake state regulates somatosensation is unknown. Importantly, studies in the same mouse, with and without anesthesia, are now possible and will expand our understanding of the basic physiology of spinal cord nociceptive processing. Our technique is best suited to longitudinal imaging using animal models that do not require invasive access to the spinal cord.

Our focus on lamina I dorsal horn projection neurons is particularly notable as these neurons transmit information used by the brain to generate pain, itch and other percepts. We recognize that the Phox2a-expressing neurons only constitute ~50% of all dorsal horn projection neurons, but do display substantial overlap of Gpr83-, Tacr1- and Tac1-expressing subpopulations[64]. Nevertheless, our initial findings are relevant to the labeled line versus patterning (population coding) question, namely, the extent to which SCPNs are polymodal or only respond to one input modality. In fact, we identified a heterogeneous population of lamina I $SCPN^{Phox2a}$, including many responding to cold, heat and noxious mechanical stimulation. The results presented here provide compelling in vivo evidence that supports previous recordings from ex vivo spinal preparations[65,66], intravital anesthetized imaging[67] and a ribosomal profiling analysis[68] that collectively suggest that a large population of superficial dorsal horn SCPNs are polymodal, responding not only to different modalities of pain-inducing stimuli but also to pruritogens that induce itch. To what extent the polymodality of the Phox2a-expressing population extends to the projection neurons that do not express this gene remains to be determined.

In summary, our methodological achievements showcase spinal projection neuron activity dynamics in tandem with complex behavioral measures and illustrate the postinjury activation of nonneuronal cells, namely microglia, which together contribute to chronic pain initiation and maintenance. These technological advances will illuminate the tissue and nerve injury-induced changes during the transition from acute to chronic pain. Notably, although applying a noxious stimulus normally evokes behavioral responses in the mouse and activity of the projection neurons, in several instances we observed that the stimulus-evoked activity did not occur concomitantly with behavior. We presume that this unexpected dissociation of activity and behavior reflects a mix of the brain's complex descending controls on the activity of dorsal horn neurons, along with the gating of nociceptive information within various nodes of the pain neuroaxis. These findings would never be detected in anesthetized mice. In the future, we anticipate studies combining analyses of spinal cord dorsal horn activity in behaving mice with dorsal root ganglia studies[69,70] and more common brain imaging or electrophysiology protocols.

## Online content

Any methods, additional references, Nature Portfolio reporting summaries, source data, extended data, supplementary information, acknowledgements, peer review information; details of author contributions and competing interests; and statements of data and code availability are available at https://doi.org/10.1038/s41592-024-02476-3.

## References

1. Sekiguchi, K. J. et al. Imaging large-scale cellular activity in spinal cord of freely behaving mice. *Nat. Commun.* **7**, 11450 (2016).

2. Ju, F. et al. Long-term two-photon imaging of spinal cord in freely behaving mice. Preprint at *bioRxiv* https://doi.org/10.1101/2022.01.09.475306 (2022).
3. Cheng, Y. T. et al. In-vivo three-photon excited fluorescence imaging in the spinal cord of awake, locomoting mouse. In *Frontiers in Optics* 2016 https://doi.org/10.1364/FIO.2016.JTh2A.183 (Optica Publishing Group, 2016).
4. Shekhtmeyster, P. et al. Trans-segmental imaging in the spinal cord of behaving mice. *Nat. Biotechnol.* **41**, 1729–1733 (2023).
5. Cheng, Y.-T., Lett, K. M. & Schaffer, C. B. Surgical preparations, labeling strategies, and optical techniques for cell-resolved, in vivo imaging in the mouse spinal cord. *Exp. Neurol.* **318**, 192–204 (2019).
6. Iseppon, F., Linley, J. E. & Wood, J. N. Calcium imaging for analgesic drug discovery. *Neurobiol. Pain* **11**, 100083 (2022).
7. Nelson, N. A., Wang, X., Cook, D., Carey, E. M. & Nimmerjahn, A. Imaging spinal cord activity in behaving animals. *Exp. Neurol.* **320**, 112974 (2019).
8. Farrar, M. J. et al. Chronic in vivo imaging in the mouse spinal cord using an implanted chamber. *Nat. Methods* **9**, 297–302 (2012).
9. Figley, S. A. et al. A spinal cord window chamber model for in vivo longitudinal multimodal optical and acoustic imaging in a murine model. *PLoS ONE* **8**, e58081 (2013).
10. Wu, W. et al. Long-term in vivo imaging of mouse spinal cord through an optically cleared intervertebral window. *Nat. Commun.* **13**, 1959 (2022).
11. Yarmolinsky, D. A. et al. Selective modification of ascending spinal outputs in acute and neuropathic pain states. Preprint at *bioRxiv* https://doi.org/10.1101/2024.04.08.588581 (2024).
12. Kerschensteiner, M., Schwab, M. E., Lichtman, J. W. & Misgeld, T. In vivo imaging of axonal degeneration and regeneration in the injured spinal cord. *Nat. Med.* **11**, 572–577 (2005).
13. Fenrich, K. K. et al. Long-term in vivo imaging of normal and pathological mouse spinal cord with subcellular resolution using implanted glass windows. *J. Physiol.* **590**, 3665–3675 (2012).
14. Mathis, A. et al. DeepLabCut: markerless pose estimation of user-defined body parts with deep learning. *Nat. Neurosci.* **21**, 1281–1289 (2018).
15. Vercauteren, T., Pennec, X., Perchant, A. & Ayache, N. Diffeomorphic demons: efficient non-parametric image registration. *Neuroimage* **45**, S61–S72 (2009).
16. Thévenaz, P., Ruttimann, U. E. & Unser, M. A pyramid approach to subpixel registration based on intensity. *IEEE Trans. Image Process.* **7**, 27–41 (1998).
17. Ghosh, K. K. et al. Miniaturized integration of a fluorescence microscope. *Nat. Methods* **8**, 871–878 (2011).
18. Binding, J. et al. Brain refractive index measured in vivo with high-NA defocus-corrected full-field OCT and consequences for two-photon microscopy. *Opt. Express* **19**, 4833–4847 (2011).
19. Takahashi, T. et al. PEO-CYTOP fluoropolymer nanosheets as a novel open-skull window for imaging of the living mouse brain. *iScience* **23**, 101579 (2020).
20. Lake, E. M. R. et al. Simultaneous cortex-wide fluorescence $Ca^{2+}$ imaging and whole-brain fMRI. *Nat. Methods* **17**, 1262–1271 (2020).
21. Mathis, A., Schneider, S., Lauer, J. & Mathis, M. W. A primer on motion capture with deep learning: principles, pitfalls, and perspectives. *Neuron* **108**, 44–65 (2020).
22. Liu, C., Xu, J. & Wang, F. A review of keypoints' detection and feature description in image registration. *Sci. Program.* **2021**, 1–25 (2021).
23. Pnevmatikakis, E. A. & Giovannucci, A. NoRMCorre: an online algorithm for piecewise rigid motion correction of calcium imaging data. *J. Neurosci. Methods* **291**, 83–94 (2017).
24. Thirion, J. P. Image matching as a diffusion process: an analogy with Maxwell's demons. *Med. Image Anal.* **2**, 243–260 (1998).
25. Reggiani, J. D. S. et al. Brainstem serotonin neurons selectively gate retinal information flow to thalamus. *Neuron* **111**, 711–726.e11 (2023).
26. Ahanonu, B. & Corder, G. in *Contemporary Approaches to the Study of Pain: from Molecules to Neural Networks* (ed. Seal, R. P.) 217–276 (Springer, 2022).
27. Chan, K. Y. et al. Engineered AAVs for efficient noninvasive gene delivery to the central and peripheral nervous systems. *Nat. Neurosci.* **20**, 1172–1179 (2017).
28. Schwinn, D. A., McIntyre, R. W. & Reves, J. G. Isoflurane-induced vasodilation: role of the α-adrenergic nervous system. *Anesth. Analg.* **71**, 451–459 (1990).
29. Takahashi, Y. et al. Organization of cutaneous ventrodorsal and rostrocaudal axial lines in the rat hindlimb and trunk in the dorsal horn of the spinal cord. *J. Comp. Neurol.* **445**, 133–144 (2002).
30. Odagaki, K., Kameda, H., Hayashi, T. & Sakurai, M. Mediolateral and dorsoventral projection patterns of cutaneous afferents within transverse planes of the mouse spinal dorsal horn. *J. Comp. Neurol.* **527**, 972–984 (2019).
31. Swett, J. E. & Woolf, C. J. The somatotopic organization of primary afferent terminals in the superficial laminae of the dorsal horn of the rat spinal cord. *J. Comp. Neurol.* **231**, 66–77 (1985).
32. Takahashi, Y., Chiba, T., Kurokawa, M. & Aoki, Y. Dermatomes and the central organization of dermatomes and body surface regions in the spinal cord dorsal horn in rats. *J. Comp. Neurol.* **462**, 29–41 (2003).
33. Li, P. & Zhuo, M. Silent glutamatergic synapses and nociception in mammalian spinal cord. *Nature* **393**, 695–698 (1998).
34. Basbaum, A. I. & Wall, P. D. Chronic changes in the response of cells in adult cat dorsal horn following partial deafferentation: the appearance of responding cells in a previously non-responsive region. *Brain Res.* **116**, 181–204 (1976).
35. Merrill, E. G. & Wall, P. D. Factors forming the edge of a receptive field: the presence of relatively ineffective afferent terminals. *J. Physiol.* **226**, 825–846 (1972).
36. Corder, G. et al. An amygdalar neural ensemble that encodes the unpleasantness of pain. *Science* **363**, 276–281 (2019).
37. Corder, G. et al. Loss of μ opioid receptor signaling in nociceptors, but not microglia, abrogates morphine tolerance without disrupting analgesia. *Nat. Med.* **23**, 164–173 (2017).
38. LaMotte, R. H., Shimada, S. G. & Sikand, P. Mouse models of acute, chemical itch and pain in humans. *Exp. Dermatol.* **20**, 778–782 (2011).
39. Callahan, B. L., Gil, A. S. C., Levesque, A. & Mogil, J. S. Modulation of mechanical and thermal nociceptive sensitivity in the laboratory mouse by behavioral state. *J. Pain* **9**, 174–184 (2008).
40. Roome, R. B. et al. Phox2a defines a developmental origin of the anterolateral system in mice and humans. *Cell Rep.* **33**, 108425 (2020).
41. Daigle, T. L. et al. A suite of transgenic driver and reporter mouse lines with enhanced brain-cell-type targeting and functionality. *Cell* **174**, 465–480.e22 (2018).
42. Ji, R.-R., Donnelly, C. R. & Nedergaard, M. Astrocytes in chronic pain and itch. *Nat. Rev. Neurosci.* **20**, 667–685 (2019).
43. Donnelly, C. R. et al. Central nervous system targets: glial cell mechanisms in chronic pain. *Neurotherapeutics* **17**, 846–860 (2020).
44. Guan, Z. et al. Injured sensory neuron-derived CSF1 induces microglial proliferation and DAP12-dependent pain. *Nat. Neurosci.* **19**, 94–101 (2016).
45. Jung, S. et al. Analysis of fractalkine receptor $CX_3CR1$ function by targeted deletion and green fluorescent protein reporter gene insertion. *Mol. Cell. Biol.* **20**, 4106–4114 (2000).

46. Shields, S. D., Eckert, W. A. III & Basbaum, A. I. Spared nerve injury model of neuropathic pain in the mouse: a behavioral and anatomic analysis. *J. Pain* **4**, 465–470 (2003).
47. Dietz, C. et al. Complex regional pain syndrome: role of contralateral sensitisation. *Br. J. Anaesth.* **127**, e1–e3 (2021).
48. van Rijn, M. A. et al. Spreading of complex regional pain syndrome: not a random process. *J. Neural Transm.* **118**, 1301–1309 (2011).
49. Kirillov, A. et al. Segment anything. In *2023 IEEE/CVF International Conf. Computer Vision (ICCV)* 3992–4003 (IEEE, 2023).
50. Bommasani, R. et al. On the opportunities and risks of foundation models. Preprint at https://doi.org/10.48550/arXiv.2108.07258 (2021).
51. Lai, X. et al. LISA: Reasoning segmentation via large language model. In *2024 IEEE/CVF Conf. Computer Vision and Pattern Recognition (CVPR)* 9579–9589 (IEEE, 2024).
52. Sun, J. J. et al. Self-supervised keypoint discovery in behavioral videos. In *2022 IEEE/CVF Conf. Computer Vision and Pattern Recognition* (IEEE, 2022).
53. Tasci, T. *Iterative Cell Extraction and Registration for Analysis of Time-Lapse Neural Calcium Imaging Datasets*. PhD thesis, Stanford Univ. (2020); https://doi.org/10.25740/rt839xk2428
54. Emond, E. C., Bousse, A., Brusaferri, L., Hutton, B. F. & Thielemans, K. Improved PET/CT respiratory motion compensation by incorporating changes in lung density. *IEEE Trans. Radiat. Plasma Med. Sci.* **4**, 594–602 (2020).
55. Cheng, Y.-T., Lett, K. M., Xu, C. & Schaffer, B. Three-photon excited fluorescence microscopy enables imaging of blood flow, neural structure and inflammatory response deep into mouse spinal cord in vivo. *eLife* **13**, RP95804 (2024).
56. Zhang, T. et al. Kilohertz two-photon brain imaging in awake mice. *Nat. Methods* **16**, 1119–1122 (2019).
57. Rodríguez, C. et al. An adaptive optics module for deep tissue multiphoton imaging in vivo. *Nat. Methods* **18**, 1259–1264 (2021).
58. Xiao, S. et al. Large-scale voltage imaging in behaving mice using targeted illumination. *iScience* **24**, 103263 (2021).
59. Streich, L. et al. High-resolution structural and functional deep brain imaging using adaptive optics three-photon microscopy. *Nat. Methods* **18**, 1253–1258 (2021).
60. Scherrer, J. R., Lynch, G. F., Zhang, J. J. & Fee, M. S. An optical design enabling lightweight and large field-of-view head-mounted microscopes. *Nat. Methods* **20**, 546–549 (2023).
61. Zhao, P. et al. MiniXL: an open-source, large field-of-view epifluorescence miniature microscope for mice capable of single-cell resolution and multi-brain region imaging. Preprint at *bioRxiv* https://doi.org/10.1101/2024.08.16.608328 (2024).
62. Fink, E. A. et al. Structure-based discovery of nonopioid analgesics acting through the α2A-adrenergic receptor. *Science* **377**, eabn7065 (2022).
63. Yekkirala, A. S., Roberson, D. P., Bean, B. P. & Woolf, C. J. Breaking barriers to novel analgesic drug development. *Nat. Rev. Drug Discov.* **16**, 545–564 (2017).
64. Alsulaiman, W. A. A. et al. Characterisation of lamina I anterolateral system neurons that express Cre in a Phox2a-Cre mouse line. *Sci. Rep.* **11**, 17912 (2021).
65. Hachisuka, J. et al. Semi-intact ex vivo approach to investigate spinal somatosensory circuits. *eLife* https://doi.org/10.7554/eLife.22866 (2016).
66. Warwick, C. et al. Cell type-specific calcium imaging of central sensitization in mouse dorsal horn. *Nat. Commun.* **13**, 5199 (2022).
67. Chisholm, K. I. et al. Encoding of cutaneous stimuli by lamina I projection neurons. *Pain* **162**, 2405–2417 (2021).
68. Wercberger, R., Braz, J. M., Weinrich, J. A. & Basbaum, A. I. Pain and itch processing by subpopulations of molecularly diverse spinal and trigeminal projection neurons. *Proc. Natl Acad. Sci. USA* **118**, e2105732118 (2021).
69. Chen, C. et al. Long-term imaging of dorsal root ganglia in awake behaving mice. *Nat. Commun.* **10**, 3087 (2019).
70. Turecek, J. & Ginty, D. D. Coding of self and environment by Pacinian neurons in freely moving animals. *Neuron* **112**, 3267–3277.e6 (2024).

# Methods

## Animals

We conducted all animal experiments in accordance with protocols approved by the University of California, San Francisco (UCSF) Institutional Animal Care and Use Committee under protocol numbers AN183265 and AN199730. We used the following mouse lines: C57BL6 (000664, JAX); Phox2a–Cre[40], provided by A. Kania (Institut de Recherches Cliniques de Montréal); Ai162 floxed-GCAMP6s[41], obtained from JAX (031562); Ai148 floxed-GCaMP6f[41], obtained from JAX (030328); Ai9 floxed-tdTomato, obtained from JAX (007909); $CX_3CR1$–EGFP mice[45], provided by J. Braz and Z. Guan (UCSF, JAX 005582); Thy1-YFP-H[71], provided by J. Chan (UCSF) and Thy1–GFP-M[71], provided by R. Liang (UCSF). We studied both male and female mice (~70:30 sex ratio). Mice used in this study were 4.9 ± 2.2 months old (mean ± s.d.). Mice were individually or group housed with ad libitum food and water access on a 12 h light–dark cycle at a room temperature of ~19–23 °C and relative humidity of 30–70%. For primers used for genotyping, please see the relevant protocols on JAX or for Phox2a–Cre, generic Cre primers, see ref. 40.

## Viruses

The nomenclature for all adeno-associated viruses (AAVs) used in this study refers to the AAV capsid. All AAVs used in this study contained the AAV2 inverted terminal repeat unless otherwise specified, for example, AAV9 indicates AAV2/9 for AAV2 inverted terminal repeat sequence and AAV9 capsid.

## Custom fabrication of spinal implant chamber components

To reduce cost and increase accessibility, we optimized the design (using PTC Creo Parametric 6.0–9.0) and fabrication of the spinal implant chamber and used standard components and widely accessible fabrication technologies. We laser cut the side bars from multipurpose 304 stainless steel, purchased as 0.048-inch/1.2192-mm (McMaster-Carr, 8983K114), 0.036-inch/0.9144-mm (McMaster, 8983K113), 0.024-inch/0.6096-mm (McMaster, 8983K111) or 0.01-inch/0.254-mm (McMaster, 3254K322) thick sheets. We predominantly used 0.036-inch (0.9144-mm) thick side bars. We outsourced custom metal laser cutting (Laser Alliance LLC), using a laser beam kerf of 0.008 inches and the design files provided in the GitHub repository. Cost can come out to ~US$10 per side bar or stabilizing plate. Using the provided designs (Extended Data Fig. 1d,e) and files, it is possible to use any laser cutting contractor after adjusting the dimensions to take into account the beam diameter. We then manually tapered the edges of the side bars with a grinding wheel (WEN, 4276 2.1 amp 6 inch) to a shallow angle (Extended Data Fig. 2c). Metal was then cleaned with a wire brush and double-distilled $H_2O$, then autoclaved at 250 °C for 20 min before implantation procedures. The tapered edge fits under the articular processes of the T12–L1 vertebra and rests against the vertebral wall. Note, if the angle of the side bars' taper is not steep enough, then additional V-groove cuts can be made near the locations where the spinous process needle will be placed. We laser cut the stabilizing plate from 0.75-mm (~1/32 inches) thick mild steel, outsourced to Laser Alliance LLC, using the design files provided in the GitHub repository. Owing to its ferromagnetic properties, we used mild steel, which made it possible to attach magnetic devices, such as the protective cover. We designed iterations of the metal stabilizing plate for custom handling and clamping during imaging and to maximize the working area around vertebrae during surgery (Extended Data Fig. 1f). The stabilizing plate is critical; without it the side bars have a high chance of snapping off, due to the lack of proper load distribution when the animal moves while fixed in the imaging setup. Further, the plate provides a platform to attach other devices, such as the miniature microscope (Extended Data Fig. 9e–q) or electrophysiology devices.

To protect the glass coverslip window from scratching and damage, we 3D printed covers (Stratasys, uPrint ABS and MakerBot, Nylon 12 Carbon Fiber (375–0061A) or ABS-R (375-0071A)) to which we attached two neodymium magnets (McMaster, 5862K141) using cyanoacrylate glue (Henkel, Loctite 4311) or optical adhesive (Norland Products, NOA 81) (Extended Data Fig. 1i,j). The cover snapped on top of the ferromagnetic stabilizing plate, which we removed during imaging, and is concave to provide space in case devices are placed at the imaging site or if the final window is not flush with the stabilizing plate. Usually, we placed a piece of masking tape on top of the stabilizing plate to keep the prep free from dust. We placed the 3D-printed magnetic cover over the tape in this case. The cover and tape are easily removed when the stabilizing plate of the animal is clamped before imaging.

To perform microCT imaging, we 3D printed side bars and the stabilizing plate with biocompatible nonmetallic materials (FormLabs, BioMed Clear Resin) (Extended Data Figs. 1b and 3a–c) using a Formlabs 3D printer located at the KAVLI-PBBR Fabrication and Design Center. Owing to the reduced tensile strength of BioMed Clear compared with steel, we designed thicker side bars (1.0 and 2.0 mm thick) and stabilizing plates (1.5 and 2.0 mm thick).

We also manufactured side bars by metal 3D printing directly, using the stereolithography (STL) models provided on the GitHub repository. This option bypasses the need to manually taper the side bars. This approach allows for more precise control over the final angle, the addition of V-grooves to accommodate spinous process needles and other features customized for experimental conditions. We tested products from Protolabs, using direct metal stainless steel 316 L (CL 20ES) with 20 µm layers, and i.materialise (Materialise NV) using titanium and high-detail stainless steel. We found that both work well and additional options are available from other 3D metal printing manufacturers (for example, shapeways and xometry).

## Spinal chamber, laminectomy and window surgical procedures

**Implant of spinal chamber (first procedure).** We began surgical procedures by inducing and maintaining mice with 2% isoflurane and administered a nonsteroidal anti-inflammatory drug, carprofen (5.0 mg $kg^{-1}$, subcutaneous injection). We depilated and disinfected a 1-cm × 1.5-cm area around the hump of the back (betadine and 70–75% ethanol). We then applied sterile ointment (Alcon, SYSTANE, white petrolatum–mineral oil) to the eyes. We then transferred mice to a custom surgical table featuring bilateral side posts that are micro-manipulatable in three axes and lined up to the lumbar enlargement. We incised the skin above the T12–L1 vertebrae using surgical scissors (Fine Science Tools (FST), 14060-11 or 14060-10), followed by intra-incisional 0.5% lidocaine. We used a gelatin sponge (Ethicon, Surgifoam) soaked in sterile saline as needed for hemostasis. We only cut the paraspinal muscle and fascia overlying each lamina, starting at the midline, and resected using microscissors (FST, 15023-10). To visualize and separate the tendinous attachments to T13, we temporarily retracted the incised muscle laterally (Roboz, RS-6504).

We then scraped the dorsal surfaces of the T12–L1 laminae (FST, 10075-16) and wiped them free of remaining connective tissue (Beaver-Visitec International, Cellulose spears, Weck-Cel). Next, we inserted dorsal spinous process needles (Accuderm Inc., 33G–1/2 inch) at the T12 and L1 vertebrae. We positioned the side bars under the needles, under the T12–T13 and T13–L1 facet joints and against the vertebral wall. We masked the intervertebral spaces using small amounts of Kwik-Sil (KWIK-SIL, WPI), and then sutured (Patterson Dental, 6-0 PGA 090-1660) and sealed (Vetbond, 3 M) the skin rostral and caudal to the side bars. We sequentially glued the needles, side bars and the stabilizing plate to each other using superglue (Henkel Adhesives, Loctite, ethyl 2-cyanoacrylate). In most circumstances, we pretreated the laminar surfaces with a dentin activator (Parkell, FeCl, C&B Metabond kit).

To secure the implant in place, we then cemented (Parkell, PMMA, C&B Metabond kit) the entire working area, except the T13 lamina. After the cement set, we covered the open area above the T13 lamina

bone with Kwik-Sil. We removed the animal from anesthesia and monitored it with supplementary heat during recovery. We administered one dose of sustained-release buprenorphine, ethiqa (3.25 mg $kg^{-1}$), by subcutaneous injection when the mice awoke. When fully ambulatory, we returned the mice to their home cage. The next day, we gave a second and third dose of carprofen (5.0 mg $kg^{-1}$) by subcutaneous injection. On day 3, we redosed with the carprofen if necessary. We monitored the health of the mice twice daily for signs of lethargy, immobility, poor grooming or weight loss. Mice with implants recovered from surgery for at least 1 week before proceeding to the laminectomy.

**Laminectomy and PRECLUDE application (second procedure).** Under 2% isoflurane anesthesia, we performed a T13 laminectomy using microscissors (FST, 15010-09) or a crescent blade (FST, 10317-14). If required, we used a high-speed bone drill (Foredom, K.1070) to clear cement over the T13 laminectomy area. After laminectomy, we immediately covered the exposed spinal cord with a gelatin sponge (Ethicon, Surgifoam) soaked in sterile saline. Using dual fine forceps, we pulled any remaining dura laterally to expose the spinal cord. We inhibited fibrosis with GORE PRECLUDE Pericardial Membrane, which we purchased from a third-party medical vendor (dotmed.com). Next, we cut the GORE PRECLUDE Pericardial Membrane to the size of the laminectomy opening using microscissors and placed it directly over the exposed spinal cord. To limit ingrowth, we placed small pieces of Surgifoam around the membrane. We blotted these small pieces dry with an absorbent spear (Beaver-Visitec International, Weck-Cel). Next, to protect and hold the PRECLUDE membrane in place, we spread Kwik-Sil over the laminectomy site and wider working area. We removed mice from anesthesia and monitored them closely postoperatively until they began to ambulate. We administered one dose of carprofen (5.0 mg $kg^{-1}$, subcutaneously) for postoperative analgesia. Mice with implants recovered from laminectomy for at least 1 week before proceeding to the window placement.

**Teflon AF and window placement (third procedure).** Under general anesthesia (2% isoflurane), we removed the Kwik-Sil and PRECLUDE Pericardial Membrane that was placed during the laminectomy procedure. Then, we immediately covered the spinal cord with a saline-soaked sponge (Ethicon, Surgifoam). We cut a Teflon AF film (VICI Metronics, Teflon AF 2400, 50 µm thick) to the size of the exposed spinal cord and placed it directly over the exposure. We placed Kwik-Sil above the Teflon AF, then adhered a 3.0-mm glass coverslip (#0, CS-3R-0, Warner Instruments) on top, forming a multilayered tier above the spinal cord and we allowed it to harden for 10 min. To reduce the chance of bubbles, we dispensed the Kwik-Sil without the mixer tip onto Press'n Seal or wax paper, which we then manually mixed using a metal microspatula (FST10167-11). We then used the microspatula to deliver the Kwik-Sil to the surgical field. The Kwik-Sil syringe is kept upright when not in use. We then added a supportive coat of bone cement (Parkell, PMMA, C&B Metabond kit) or Norland UV-curable optical adhesive (NOA 81) from the base of the implant to the coverslip. We administered carprofen (5.0 mg $kg^{-1}$, subcutaneously) for postoperative analgesia.

**Teflon AF sourcing.** The Teflon AF 2400 (33 or 50 µm thickness) used in this study was obtained from Amos Gottlieb at Random Technologies LLC. VICI Metronics commercially offers Teflon AF film of different thicknesses (https://www.vicimetronics.com/products/teflon-af-films-1) including 50 µm (SKU: AF-050-025-025).

### Additional surgical procedures

**Retro-orbital injections.** We delivered AAV-PHP.eB-CAG-NLS-GFP (Addgene, 104061-PHPeB) and AAV-PHP.S-CAG-tdTomato (Addgene, 59462-PHP.S) via retro-orbital injections. We briefly anesthetized mice (2% isoflurane) and placed them on a covered heating pad (Kent Scientific, RT-JR-15). We pulled back the skin surrounding the to-be injected eye, which forced the eye to partially protrude. For analgesia, we applied a drop of 0.5% proparacaine HCl (Medline Industries, 24208-730-06) or Alcaine (Medline Industries, 0998-0016-15) onto the to-be injected eye, then dabbed away excess fluid using a gauze placed at the medial canthus. We then slowly guided the needle at a ~30° angle, with the bevel facing medially, until the needle contacted the underlying bone. We confirmed the absence of blood and then injected 100 µl of of the following viral titers: $2.3 \times 10^{11}$ vg per mouse for AAV-PHP.S-CAG-tdTomato ($2.3 \times 10^{13}$ GC $ml^{-1}$) and $2.2 \times 10^{11}$ vg per mouse for AAV-PHP.eB-CAG-NLS-GFP ($2.2 \times 10^{13}$ GC $ml^{-1}$). Afterward, we applied eye ointment (Alcon, 02444062 Systane) and transferred the mice to a new heated cage.

**Intraspinal injections.** We drove expression of Cre pan-neuronally in the spinal cord via intraspinal injection of AAV2retro-hSyn-Cre (Addgene, 105553-AAVrg) (Fig. 4a). Briefly, we pulled a glass micropipette (WPI, 1B100F-4, 1 mm borosilicate glass capillaries) using a puller (WPI, PUL-100) and cut it to a tip diameter of 50–100 µm. We attached the glass micropipette to a 10-µl syringe (Hamiton, 7653-01) using compression fittings (Hamilton) and filled it with mineral oil. We then aspirated the virus into the micropipette using an automated pump (Harvard Apparatus, 70-4507 Pump 11 Elite) attached to a stereotactic arm. We injected 50 nl at 10 nl $min^{-1}$ into the dorsal horn ~500 µm ventral to the surface of the meninges and held the micropipette in place for 3 min after injection. We made two injections on the same side of the spinal cord.

**Neuropathic pain model.** We performed SNI[36,46] in a subset of $CX_3CR1$–EGFP mice. We anesthetized mice (2% isoflurane for both induction and maintenance) and transferred them to a stereotaxic surgical station (Kopf Instruments, model 942). To remove hair from the hindlimb, we used a shaver (Wahl Professional, 8685) rather than hair removal cream, due to the risk of chemical burn and any of the substance getting into the open wound, which would alter the pain model. We then cleaned the surgical site using 70% ethanol then betadine followed by 70% ethanol. We made a small incision in the skin along the mediolateral axis, then widened the hole by inserting and spreading scissors (FST, 14072-10), rather than performing additional cuts. This exposed the biceps femoris muscle that, along with the artery genus descendes, we use as a landmark to begin incision to expose the sciatic nerve. To avoid the possibility of accidentally cutting the nerve, we parted the overlying muscle using forceps (FST, 11231-20 and 11223-20). After exposing the sciatic nerve, we identified the common peroneal (CP), tibial (T) and sural (S) branches. We performed a CP and T ligation near the CP–T–S branch point using 8-0 silk sutures (S&T, 03192), then transected (FST, 91500-09) the CP and T branches at two locations about 1 mm distal to the ligation site. We closed the muscle using 6-0 silk sutures (Henry Schein, 101-2636) and sealed the skin using cyanoacrylic glue (3M, Vetbond 084-1469SB).

To account for the fact that some $CX_3CR1$–EGFP mice had different pre-injury EGFP fluorescence ($F$) between left and right dorsal horns, we performed SNI surgeries on either the left ($n = 3$) or right ($n = 1$) sciatic nerves after we measured the spinal cord microglia bulk fluorescence bilaterally and divided into groups of mice that had either $F_{ipsi} > F_{contra}$ or $F_{ipsi} < F_{contra}$.

### Optical imaging through the spinal window

**Stereoscope validation of window optical clarity.** Under anesthesia (2% isoflurane), we periodically checked the clarity of the window using a stereo microscope (Leica, MZ12.5 stereoscope), a large sensor camera (The Imaging Source, DFK 33UX183c) and vendor-provided image acquisition software (The Imaging Source, IC Capture 2.5). We strove to maintain optical imaging parameters (zoom, white balance and other properties) across real-color image acquisition sessions.

### In vivo spinal cord imaging

**One-photon imaging setup.** Throughout the study, in both anesthetized and awake imaging, we acquired in vivo imaging data using a 3i VIVO multiphoton movable objective microscope with phasor equipped, which permitted switching between one- and two-photon imaging in the same animal and microscope without touching the animal or altering the setup (Fig. 3c,g). We suppressed vibrations with an optical vibration control air table (TMC, 14-416-45). The one-photon light path consists of an LED light source (Excelitas, X-Cite 110 light-emitting diode (LED)) directed into a vertical illuminator (Olympus) containing a green (Semrock, GFP-3035D-OMF-ZERO) or red (Semrock, TxRed-4040C-OMF-ZERO) filter set. Emitted fluorescent light reflected back through the illuminator through a tube lens (Olympus, U-TLU) onto a charge-coupled device (CCD) or scientific Complementary Metal–Oxide–Semiconductor (sCMOS) camera. We used an alternative setup in the same microscope to allow simultaneous multicolor one-photon imaging. This setup involved a multiband dichroic (Semrock, GFP/DsRed-A-OMF) to simultaneously excited green and red fluorophores, emitted fluorescent light passed back through this dichroic and into a dual camera image splitter (Photometrics, TwinCam). The splitter contained a dichroic beamsplitter (Semrock, FF560-FDi01-25 × 36) that passed >560 nm light to a red bandpass filter (Semrock, FF02-641/75-25) before reaching the sCMOS camera 1 (Photometrics, Kinetix) while the beamsplitter passed <560 nm light to a green bandpass filter (Semrock, FF01-520/35-25) before reaching the sCMOS camera 2 (Photometrics, Kinetix).

We used several cameras for widefield fluorescence imaging: Photometrics CoolSNAP EZ, Photometrics Kinetix, Hamamatsu Fusion BT, Hamamatsu Prime BSI, PCO pco.edge 4.2 bi USB and Zeiss AxioCam 712. We acquired videos for in vivo spinal cord imaging of awake mice at 10- or 20-ms exposure time across all cameras. Each camera had the following specifications and settings during use. The read noise range is given as several cameras had high sensitivity and dynamic range modes. We used a Photometrics CoolSNAP EZ with a quantum efficiency (QE) of 60–65% and read noise of 6–8 $e^-$ root mean square (r.m.s.). We used Photometrics Kinetix cameras with a QE of ~95% and read noise of 0.7–1.3 $e^-$ r.m.s. using sensitivity or dynamic range modes. For the imaging sessions using the Kinetix, to accommodate large differences in brightness between animal lines and fluorescent proteins, we used dynamic range mode for mice in Figs. 3 and 6 and sensitivity mode for mice in Fig. 5. We used a Hamamatsu Fusion BT with a QE of ~95% and read noise of 1.0–1.4 $e^-$ r.m.s. We used a Photometrics Prime BSI with a QE of ~95% and 1.1–1.8 $e^-$ r.m.s. read noise. We used a PCO pco.edge 4.2 bi USB with a ~95% QE and 1.1–1.8 $e^-$ r.m.s. read noise. We used a Zeiss AxioCam 712 with a QE of ~72% and read noise of 1.29–2.2 $e^-$ r.m.s.

We collected most data used in this study from a Photometrics CoolSNAP EZ CCD and Photometrics Kinetix sCMOS cameras. To simultaneously image the left and right spinal cord, we used low-magnification objectives: 4×/0.16 numerical aperture (NA) (Olympus, UPLXAPO4X), 5×/0.16 NA (Zeiss, 420630-9900) and 5×/0.25 NA (Zeiss, 440125-0000-000). We conducted the majority of imaging using the Fluar 5×/0.25 NA objective. Additionally, a 2×/0.08 NA (Olympus, 1-U2B921) objective provided an overview for a very large FOV, but at the cost of reduced signal. We used high-magnification objectives, 20×/1.0 NA (Zeiss, 421452-9600) and 20×/0.45 NA (Olympus, LCPLN20XIR) to conduct high-resolution imaging of cells, axons or glial morphology (Fig. 6b–d). To compare intensity across time, we maintained the LED power at a constant level on a per animal basis and periodically checked the power output using a light meter positioned at the focal point of the objective (see the LED power output for one-photon imaging section). Additional details on optimizing the setup can be found in Supplementary Notes 7–9.

**Two-photon imaging setup.** The two-photon light path of the movable objective microscope scope consisted of an excitation laser (Coherent, Chameleon Discovery Ti:Saph) and a phasor laser (Spectral-Physics, FemtoTrain laser) that are directed to a three-galvo Vector RS+ module, allowing for either dual-galvo (Cambridge Technology, 6215H) or resonant scanning. The latter enabled 30 frames per second (FPS) full-frame scanning. Emitted light is reflected to the photomultiplier tubes (PMTs) through a long-pass dichroic (Chroma, 670 LP Dichroic) above the objective and through an infrared blocking filter (Semrock, FF01-750/SP-25). We split emitted light to the PMTs with a red/green PMT dichroic (Chroma, 565 dcxr), then placed green (Chroma, ET525/70 m-2pm) and red (ET605/70 m-2p, Chroma or FF02-641/75-25, Semrock) filters in front of each PMT (Hamamatsu, H11706P-40 GaAsP). We controlled focus and the axial position of the objective using a micromanipulator system (Sutter Instrument, MPC-200 and ROE-200). We set the laser to 920 nm when collecting images from mice expressing GCaMP6s/f, EGFP ($CX_3CR1$–EGFP) or GFP (Thy1–GFP). For mice expressing tdTomato, we set the excitation laser to 920 or 1,050 nm. We controlled laser power with a Pockels cell set to 40% (4 V, for a subset of experiments) and normally to 50–80% (5–8 V) of maximum power. We measured laser power, using a near-IR compatible light sensor and power meter (Thorlabs, S121C and PM100D), delivered at the focal plane to be 64.27 mW (40%) and for the majority of experiments at 88.73–135.3 mW (50–80%). We set the gain of red and green PMTs to 65–80%, and held this gain constant for each animal for longitudinal cross-session imaging experiments.

**LED power output for one-photon imaging.** To ensure the reliability of our fluorescence imaging measurements, we periodically tested the LED power output using a visible light sensor (Thorlabs, S120C) and power meter (Thorlabs, PM100D). For consistent power measurements across time, we centered the illumination profile on the center of the sensor and by directly focusing on the surface using the microscope's software (SlideBook 6), we ensured that the sensor surface was in the focal plane of the microscope. We then used custom MATLAB scripts to create a calibration curve between the software's arbitrary power scale and power (milliwatts) or irradiance (milliwatts per square centimeter). For all one-photon imaging experiments, we acquired data with LED power set to 30–40 in SlideBook, which corresponded to total power (at given SlideBook power) of blue excitation light at the focal plane of 3.52 (30) and 4.28 (40) mW with the Zeiss Fluar 5×/0.25 NA, 2.3 (30) and 2.78 (40) mW with the Zeiss 5×/0.16 NA, 5.47 (30) and 6.61 (40) mW with the Zeiss 20×/1.0 NA, and 3.71 (30) and 4.49 (40) mW with the Olympus 20×/0.45 NA.

**Microsphere measurements with and without Teflon AF.** To confirm that Teflon AF 2400 did not affect optical imaging quality, we estimated the point spread function with and without Teflon AF using microsphere measurements. We serially diluted and sonicated 1-µm yellow–green fluorescent microspheres (Invitrogen, F8765) to a final concentration of $1{:}10^6$ from stock in distilled $H_2O$, then placed the resulting solution on a standard glass slide and placed a #0 coverslip on top. We stored beads in the dark at 4 °C. We conducted one-photon imaging with a water-immersed Zeiss 20×/1.0 NA at 5.47 mW (30 power in SlideBook) at 100 ms exposure followed by two-photon imaging at 920 nm with 7.43× zoom and power delivered ~64 mW (PMT gain 90%) or ~135 mW (PMT gain 65%). We placed the Teflon AF on top of the coverslip and repeated the imaging procedure on the same regions. To correct for any residual bidirectional scanning pixel shift errors, we used the 'Correct X Shift' plugin within ImageJ. To plot the profile through individual beads, we selected individual beads, then used the 'Plot Profile' built-in ImageJ tool followed by normalizing the profile intensity $I$ at each location $x$ by $I(x) = \frac{I(x)-\min(I)}{\max(I)-\min(I)}$. The results are shown in Extended Data Fig. 2m–o.

**Setup for spinal cord recording.** To reduce the strain of the animal's lateral movements on the implant, we placed the mice in an imaging apparatus with blinders (Figs. 4c and 5d and Extended Data Fig. 9a).

These blinders underwent several iterations, starting with solid 3D printed materials (MakerBot, nylon 12 carbon fiber 375–0061A or ABS-R 375-0071A). We settled on an infrared transmitting acrylic (ePlastics, ACRY31430.125PM 11.555 × 11.850), which is optically transparent at wavelength ($\lambda$) > 700 nm, visibly black, faster to manufacture using laser cutting and less likely to break than the prior 3D printed materials. The blinder reduced the mice's ability to see both the surroundings and the experimenters, while allowing us to use infrared 850 nm LED lights (Waveform Lighting, 7031.85; LIYUDL, B071KPSGCT; and Shenzhen Jing Cheng Digital Surveillance Co, IRINB04L) and cameras to monitor animal behavior. We prevented the mice from twisting and reaching for the objective by placing a 3D-printed top blinder that we could slide in and out as needed. We fixed mice in the apparatus using either one or two standard clamps (Thorlabs, PC2), either on the side bars or on the rostral or caudal wings of the stabilizing plate. By the final iteration we found that we only needed to use a single clamp—this simplified the design of the apparatus and allowed more flexibility, and made it possible to mount mice more rapidly. We used a goniometer (Thorlabs, GNL20), which gave us freedom to adjust the tip and tilt of the spinal window for each animal with the focal plane of the microscope. We first aligned the planes by eye, then conducted further adjustments while imaging until we determined that we had the maximum amount of the FOV in focus. It should be noted that due to the large rostrocaudal and mediolateral size of our window, the spinal cord in both orientations has a curvature that can at times prevent the entire FOV being in focus, requiring acquisition of 3D stack videos. We raised or lowered the animal with a jack (Thorlabs, L490) or mounting bracket (Thorlabs, C1515).

We used the same infrared transmitting acrylic to custom cut a 21.8-cm diameter circular gridded floor (see design files in the GitHub repository). This design provided a visibly opaque surface for the animal to run on during imaging sessions, while we monitored limb movement with an IR-capable camera and delivered peripheral stimuli (Fig. 5d and Supplementary Video 14). A prior version of the running wheel used an aluminum (to avoid rusting) grid (McMaster-Carr, 92725T51) with the same spacing and hexagonal pattern cut to fit into the circular running wheel. With either design, we attached them onto custom 3D printed parts that connected to a rotary encoder (Signswise, LN11-ERGA) that measured animal locomotion. We held the rotary encoder in place using a custom-designed 3D printed part that attaches onto standard half inch Thorlabs optical posts for integration into the setup.

We monitored animal behavior using two to four cameras in four configurations: (1) cameras monitoring the left and right side of the body; (2) cameras monitoring the face or rear of the animal; (3) cameras monitoring the left, right, and bottom of the animal; and (4) a camera zoomed in on the face. We synchronized these cameras with the microscope via transistor–transistor logic signals (TTLs) delivered to each camera, via Bayonet Neill–Concelman (BNC) and Hirose (The Imaging Source, CA-x2-HIR-OE/1.5) cables. Using a BNC splitter, we sent the same TTLs to a logic analyzer (Saleae, Logic 8) for synchronization with sensory stimuli, sound and other experimental devices. To protect the bottom camera from animal waste, we laser cut a slot into a plastic cover (Corning, 07-200-600) that allowed it to slide into the space between the rotary encoder and 3D printed running wheel connector.

**Awake imaging of the spinal cord.** Before initiating awake recordings, we habituated mice to the imaging room and/or apparatus for 1–3 days. The room was 53.0–53.3 dBA with all instruments off and 59.7–60.4 dBA with all instruments on, measured with a sound meter (Tadeto, SL720) at the location where the animal would be located during imaging. For experiments in which no stimulation is given, we imaged with all lights off, at an effective 0–1 lux. To facilitate visualization of hindpaw and accurate experimenter delivery of stimuli along with minimizing change in illumination for the mouse, we provided ~4-lux red light using LEDs (ALITOVE, AL5RWPBK12V) controlled by a flicker-free LED dimmer (Waveform Lighting, 3081). At the beginning of each imaging session, we loaded mice onto the apparatus (while we lit the room with ~280-lux white light) using the clamps and allowed them to habituate for several minutes with the lights off. We then collected the following one-photon widefield images or videos: (1) reference images in green and red channels with either no or with 2 × 2 binning, (2) a 3D stack in the green and, where applicable, red channel with 10-µm spacing over a range that started at the glass coverslip surface and extended into the spinal cord until we lost focus and (3) ~13.9 or 20 Hz videos in the green and, when applicable red, channel with either no or with 2 × 2 binning (normally for 1,000 and 300 frames, respectively). For mice that underwent two-photon imaging, such as for the Thy1–GFP and $CX_3CR1$–GFP studies, we collected (1) maximum FOV (1× zoom) time series with no frame averaging, (2) a 3D stack (for $CX_3CR1$–GFP mice) with 1 µm spacing (for example, for $CX_3CR1$–GFP, 361 ± 49 planes (mean ± s.d.)) and (3) 2.0736× and 3.58318× magnification time series videos.

For GCaMP6s/f imaging, we used a modified protocol for the final widefield imaging step. We collected a ~2 min baseline period in which we did not intentionally present any peripheral stimuli. We then delivered two to five blocks of stimuli to the hindpaw: noxious cold (~4 °C water), noxious mechanical (pinch with forceps), noxious heat (~55 °C water), air puff (gas duster) or loud sound (93.4–94.1 dBA noise, aimed at the face). For certain mice, we also delivered a noxious mechanical (pin prick, 25G needle), innocuous mechanical (2.0-g von Frey hair) or brush (NicPro, MG015, Flat 1 and Round 1) stimulus to the hindpaw.

**Sensory stimuli delivery during awake recordings.** We delivered sensory stimuli to the left and right hindpaws or the face. Owing to their favorable heat capacity and thermal conductivity compared with plastic, we used 2-ml glass syringes (Synthware Glass Syringes, S371202) to deliver noxious cold and heat stimuli. We preheated or precooled the syringes in water baths at the set temperature, which reduces the drop in temperature of the applied liquid during the time it takes to transfer to the animal's hindpaw. We cooled water to 4 °C (Yeosen, PH-F3) and heated water to ~55 °C using a hot plate (Fisher Scientific, HP88854200) set to 170 °C. We concurrently monitored the temperature. For certain mice (Fig. 4e–g) we measured the force applied during the pinch, using a force-sensitive resistor (Adafruit, 166) attached midway along the forceps (AVEN, 18434). For these studies, we did not convert the force measurements from arbitrary to real units, as this approach was used solely to automatically synchronize stimuli with fluorescence imaging data and the behavior camera videos. As we periodically observed bursts of $SCPN^{Phox2a}$ neural activity (GCaMP6s/f) without applying a stimulus and to address the possibility that it was locomotion or other behaviors that drove $SCPN^{Phox2a}$ neural activity (GCaMP6s/f) even during application of a noxious stimuli, we also delivered a loud sound directed at the animal's face using a piezo buzzer (Intervox, BRP3018L-12-C). At the animal, the sound would be ~93.4–94.1 dBA with an intensity in the 2,000 ± 500 Hz range. For certain mice, we used a small infrared LED placed in the FOV of one of the behavior cameras to indicate when we had activated the sound stimulus. This allowed further confirmation when synchronizing with video files. We sent a TTL to the logic analyzer, on a unique channel, whenever we triggered the sound. We used a 25G needle to deliver a noxious pin prick from below the animal through the floor grating. We considered this a 'light' pin prick, as we tried to slowly bring the pin to the animal's hindpaw and withdrew the pin on first contact, in contrast to a 'heavy' pin prick in which a stabbing motion is made. The latter is more likely to puncture the animal's skin and cause bleeding, which can alter interpretation of any subsequently delivered stimuli.

Using a custom-made clicker, we manually annotated each time we delivered a stimulus. The clicker synchronized this timing by sending a TTL into the same logic analyzer (Saleae, Logic 8) data stream as the microscope TTLs. To align the exact frame when each stimulus was delivered, we conducted post hoc analysis by going through behavior videos for a given imaging session, frame by frame, near times when

stimuli were indicated to have been delivered. We then annotated when the forceps, needle, von Frey fiber or liquid first touched the animal's hindpaw. We used these frame times in downstream analysis.

**Recording during virally mediated gene expression.** Compared with expression of NLS–GFP in cell bodies, we observed dimmer tdTomato expression in axons, which took longer to be detected, probably owing to the increased time to synthesize and transport the fluorescent protein from the sensory neurons' somas to their axons and the more diffuse localization of the tdTomato compared with nuclearly localized GFP. Near daily imaging afforded by our preparation identified the expected logistic-like curve in expression of both proteins (Fig. 3m and Extended Data Fig. 7e), which had a time course to maximal fluorescence that was similar to prior fiber photometry measurements of AAV-driven fluorescent protein expression in the brain[72].

**Anesthetized animal recordings.** We anesthetized mice (2% isoflurane) inside an induction chamber and transferred them to the same setup as used for awake imaging, but with modifications for anesthetized recording. We provided heat (Stoelting, 50300) while we delivered 2% isoflurane via a nose cone (Kent Scientific, SOMNO-0801) and removed excess isoflurane using a vacuum line connected to the nose cone or with a 3D printed scavenger placed around the nose cone. We monitored breathing throughout imaging. To prevent liquid spilling onto the heating pad and other devices, we placed a thermoplastic (high-density polyethylene, HDPE) sheet below the animal's hindpaws. We applied noxious thermal stimuli (~4 °C for cold and ~55 °C for heat) using a liquid drop, then rapidly removed it with a syringe attached to a vacuum line, which avoided tissue damage. We delivered a noxious mechanical pinch to the hindpaw or tail using forceps (AVEN, 18434) for ~1–2 s. We delivered air puff for ~1–5 s using a compressed gas duster (Dust-off 8541677532 and 8541677551). We only delivered this stimulus with the canister facing in the upright orientation to avoid delivery of liquified gas, which can cause tissue damage (frostbite). For a subset of experiments, we delivered sound toward the face, as previously described. After experiments, we returned the mice to the home cage and monitored them until they awoke.

**Recording in anesthetized and awake states in the same session.** For the session shown in Fig. 3p and Extended Data Fig. 8c–e, we mounted the animal as described above. We then recorded the animal for ~4 min before manually bringing a nose cone to the animal's face while delivering 2% isoflurane at a higher than normal flow rate (~4.0 l $min^{-1}$ $O_2$), until the animal became unresponsive and stopped moving. Then we reduced the flow rate to a normal maintenance rate (0.8 l $min^{-1}$ $O_2$). We continued imaging and finally removed the nose cone and allowed the animal to gradually wake up. For the experiments in Fig. 3p, there is a 05:36.9 min gap in data collection between the end of isoflurane and the return to the awake state.

**Multiplane recording of monocytes in $CX_3CR1$–EGFP mice.** We recorded multiple planes in $CX_3CR1$–EGFP mice under general anesthesia (2% isoflurane) using the imaging setup described above. To maintain optical clarity when using the 20×/1.0 NA water objective during long-term recordings, we used ultrasound gel (Parker Labs, 638632490755), which has a similar refractive index as water, but is resistant to evaporation. We collected 9 or 11 planes from the spinal cord meninges to parenchyma consisting of slices spanning 212 and 159 µm, respectively. We manually set the spacing for the slices (Fig. 6d) based on planes with maximal difference in features (for example, types of cells). For two-photon imaging, we recorded at 920 nm for ~21 (~0.24 Hz) and ~15 (~0.2 Hz) min delivering 61.05 ± 3.26 mW, Pockels cell set to 35% (3.5 V) and green PMT gain set to 67%. For multiplane data collected in an awake animal, we collected 324 planes spaced 0.9 µm apart (291.6 µm thickness) and Pockels cell set to 30% (3.0 V).

**Freely moving spinal cord imaging with miniature microscopes.** We mounted mice that already had the spinal cord chamber and window under anesthesia (2% isoflurane) on a stereotaxic surgical station (Kopf Instruments, Model 942) or in our one-photon setup described in 'One-photon imaging setup' section. Alternatively, we mounted awake mice using a custom setup using previously described methods[26]. Briefly, we lowered a miniature microscope attached to a holder (Inscopix, Commutator System) using a micromanipulator until the dorsal vasculature or fluorescently labeled cells became visible. We then attached a layer of dental composite (Pentron Clinical, Flow-It A2/N11VB) onto the stabilizing plate surrounding the miniature microscope baseplate (Inscopix, 1050-004638 and Open Ephys, Miniscope V4 Base Plate Variant 2) and cured it using blue light (BoNew, ~1,500–2,000 mW LED light). We then attached the baseplate to the composite using UV-curable glue (Loctite, 4310). In subsequent sessions, we attached the animal to a clamp and mounted the miniature microscope in the baseplate while the animal was awake.

We recorded multicolor signals from a miniature microscope (Inscopix, LScape module for nVue 2.0 nVue LScape; Inscopix, nVista; and Open Ephys, Miniscope V4.4) at 10, 20 or 30 Hz (100, 50 and 33.3 ms exposures, respectively). For nVue LScape imaging, the LED illumination alternated between green and red leading to an effective single channel acquisition rate of 5, 10 or 15 Hz. We set the gain to 15 and normally delivered 0.2–0.4 mW $mm^{-2}$ of green (455–480 nm) or red (545–580 nm) light during prolonged imaging. We converted imaging data to TIF or HDF5 using custom MATLAB codes and the Inscopix data processing software application programming interfaces (APIs). We processed movies as outlined in '$Ca^{2+}$ imaging data preprocessing with downsampling and detrending'. We conducted open field recordings using a setup as described in 'Assaying locomotion in the open field' section. To deliver noxious stimuli, we placed mice in a setup similar to that described in 'Mechanical sensory thresholds' section and stimuli as described in 'Sensory stimuli delivery during awake recordings' section.

## MicroCT imaging and data processing

We conducted microCT imaging of naive and spinal chamber implanted mice using standard imaging protocols approved by UCSF Institutional Animal Care and Use Committee at UCSF China Basin. We induced and maintained mice under 2% isoflurane while scanning mice using the microCT component of the MILabs U-SPECT VECTor4/CT (MILabs B.V.) preclinical imaging system (MILabs B.V., Rec 12.00-st). To set the scanning bounds, we used built-in optical cameras followed by CT acquisition using X-ray tube parameters of 50/55 kV and 0.24/0.19 mA, 75-ms exposure per step and 360° (0.375° step, 960 projections) scan acquired in step-and-shoot mode. We did not apply any binning during data acquisition. We created an isotropic reconstruction of microCT data using vendor-provided MILabs reconstruction software v12.00 at a voxel size of 0.02 mm × 0.02 mm × 0.02 mm with cone-beam filtered back-projection using the Feldkamp algorithm[73].

We used a custom pipeline to process microCT data (Extended Data Fig. 3g), by first downsampling the raw image stack files 2× in $x$ and $y$ (for example, coronal) spatial dimensions, which facilitated faster processing. For data from whole-body scans of mice, we manually went through each slice and removed scan artifacts where possible. For display purposes in Fig. 1h only—to allow easier reader visualization of bone, soft tissue and spinal chamber implant as the quantitative difference in intensity is not critical for interpreting that data—we applied successive gamma corrections ($V_{out} = V_{in}^{\gamma}$) with $\gamma = 0.78$ and $\gamma = 0.70$. By visually setting thresholds in ImageJ (version 1.53d) or Invaleus (version 3.1), we segmented bone, soft tissue and (where applicable) 3D printed components and glass. In ImageJ, we then used the volume viewer method to construct a 3D mesh. In Invaleus, we used built-in methods for setting masks and creating surfaces. We exported the resulting meshes from ImageJ or Invaleus and imported them into MeshLabs (version 2020.07).

Within MeshLabs we manually removed vertices, faces and edges that are due to scan and other artifacts. We then cleaned up the model, for example, using Laplacian smoothing (three iterations), and ran quadric edge collapse decimation to reduce the number of vertices and faces to reduce computational load during 3D rendering. For Fig. 1a and surgery videos (Supplementary Videos 2–4), see Supplementary Note 10 for details in producing the model and video renders.

### Scanning electron microscopy of Teflon AF 2400 and PRECLUDE

We loaded Teflon AF 2400 and PRECLUDE samples onto stubs (12.64 mm diameter) using double-sided tape and coated samples with a 4-nm layer of gold/palladium using a coater (Leica EM ACE600). We imaged samples in a scanning electron microscope (Zeiss, FESEM Sigma-500) at 3.00 keV and detected secondary and backscattered electrons with in-lens (SE1) and SE2 detectors. We collected images at multiple magnifications as specified in Extended Data Fig. 2j,k. Due to the electron beam damaging Teflon AF 2400 samples, we were unable to collect images at as high of a magnification as PRECLUDE.

### Generation and sources for 3D models

We created 3D models using a mix of our own microCT generated data, our own models (for example, for side bars and stabilizing plates) and publicly available designs. We downloaded the following models and used them in either Fig. 1a or Fig. 4c. We downloaded Thorlabs parts from their respective product web pages as STEP files. The 4× objective in Fig. 4c is https://www.thorlabs.com/thorproduct.cfm?partnumber=RMS4X-PF. McMaster-Carr provides design files for many of their components, we downloaded and used STEP files for screws (McMaster, 91781A350) and Neodymium magnets (McMaster, 5862K141). We downloaded the following GrabCad SOLIDWORKS files from https://grabcad.com/library/incremental-optical-rotary-encoder-400-pulse-1. For camera models, we used STEP files provided by The Imaging Source at https://www.theimagingsource.com/en-us/product/industrial/37u/dfk37bux252/. We converted all STEP and other formatted files into PTC Creo Parametric PRT files to integrate into our assemblies.

### Histology

We perfused mice with phosphate-buffered saline (PBS), followed by 4% formaldehyde (FA) (10% formalin (Thermo Fisher Scientific, 119690010) in 1× PBS), dissected out the spinal column and left the spinal column overnight in 4% FA. We manually dissected the spinal cord after the removal of overlying vertebrae and then switched samples to either further fix in 4% FA or PBS, followed by cryoprotection with 30% (w/v) sucrose. We cut sections on a freezing microtome (Microm, HM 440E) at 100 µm thickness. We then washed samples three times with PBS in 0.3% or 0.8% Triton-X100 and with a normal goal serum (NGS) blocking solution. In Fig. 1r and Extended Data Fig. 3, we identified astrocytes by immunohistochemistry (IHC) with anti-GFAP (1:2,000, Agilent Dako, Z0334). In Fig. 1r, Extended Data Fig. 4 and Supplementary Fig. 4a, we imaged microglia using the endogenous EGFP signal of $CX_3CR1$–EGFP mice. In Figs. 4b and 5b and Supplementary 4b, we acquired images of Ai162;Ai9 samples using the endogenous GCaMP6s/f or tdTomato signals. We counterstained cells or their nuclei using Neurotrace (1:500, Thermo Fisher, N21479) or 4,6-diamidino-2-phenylindole (DAPI) (1:1,000, 1 µg $ml^{-1}$), respectively. Confocal-acquired, representative images are shown as max intensity projection of a $z$-stack with axial sections spanning the section's thickness. We acquired all histological images using an Olympus FV3000 equipped with 405, 488, 561 and 640 nm OBIS Coherent lasers along with 4×/0.16 NA UPlanXApo and 10×/0.4 NA UPlanXApo objectives.

### Behavioral testing

**Assaying locomotion in the open field.** The open field arena consisted of a custom-built 2-ft-diameter white base (TAP Plastics, HDPE) and 15.5–16-inch tall white walls (Mr. Plastics, WHT POLYSTYRENE). We provided overhead lighting using either two LED lamps (Barrina, INWT504005650Fc and JOOFO, clipper0722-54) or LED light strips (Waveform Lighting, 3004.40 (5,000 K)) controlled by flicker-free LED dimmer (Waveform Lighting, 3081). We acquired videos of animal locomotion using cameras (The Imaging Source, DMK 21AU04 and DFK 42BUC03) and image acquisition software (The Imaging Source, IC Capture 2.4 or 2.5 or Mathworks MATLAB, Image Acquisition Toolbox). Before each experiment, we measured light power (JRLGD, LX1010B) and adjusted lighting to deliver ~100 lux of light. We cleaned the arena with 70% ethanol before and after each animal's session. We placed mice in the center of the open field arena and allowed them to freely locomote for the duration of the recording session (30 min, 15 Hz). We ran up to three mice simultaneously in three arenas in the same room. For miniature microscope experiments, as in Fig. 4m, we ran the recordings for various lengths of time as indicated in the figures or legends, for example, 124.8 min for Fig. 4m.

**Motor control using rotarod.** We tested locomotor control using an accelerating rotarod assay (Ugo Basile, 7650 and 47650) that consisted of a 30-mm-diameter rod elevated above a floor that automatically detected when an animal fell. We habituated mice in the behavior room for 30 min to 1 h before testing. For each day of behavior testing, we recorded videos of three trials with a rod going from 4 to 30 rotations per min over 5 min that then maintained 30 rotations per min for the rest of the trial. We then monitored mice until they fell off. Additional details and considerations about the rotarod assay can be found in Supplementary Note 11.

**Mechanical sensory thresholds.** We measured mechanical sensory thresholds using von Frey filaments (Stoelting, 58011) and the simplified up-down method (SUDO)[74]. We habituated mice for 30 min to 1 h on a custom von Frey rack[26] inside clear circular tubes (6-inch H × Ø3.75-inch ID) spray painted white (McMaster, 2571N11) with a transparent section facing the experimenter. We started with the 0.6 g-force (gf) hair and then tested subsequent trials at lower or higher gf hair if the animal did or did not exhibit responses, respectively. We used the following series of von Frey hairs, numbered 1–9 for SUDO threshold calculations: 0.04, 0.07, 0.16, 0.4, 0.6, 1, 1.4, 2.0 and 4.0 gf. We defined responses as any of the following that occurred while the von Frey hair contacted the hindpaw: hindpaw lifting (withdrawal), shaking, licking or guarding. We did not count toe spreading—splaying or other movements of the toes in response to contact with the von Frey hair that were not followed by withdrawal behaviors—as a response nor did we count responses occurring right after the offset of the von Frey hair, so as to avoid behaviors due to flicking of the hairs during offset or related artifacts. We pressed the von Frey hair until it bent to ensure consistent force application across trials and mice.

We calculated the SUDO PWT 50% mechanical threshold using $\mathrm{PWT} = 10^{xF+B}$, where $x = 0.24$, $B = -1.54$ and $F$ is the final filament number, along with a +0.5 or −0.5 adjustment factor depending on whether the animal did not or did respond to the final filament, respectively. The estimated 50% threshold using the Chaplan up-down method is calculated as $T_{50\%} = 10^{\log_{10}(F)+\kappa\delta}$, where $F$ is the force (gf) of the final filament hair, $\kappa$ is the lookup value based on the sequence of responses and $\delta$ is the mean difference in gf (in log units) between adjacent hairs in the sequence (here $\delta = 0.25$). We used the lookup table as in the original up–down method[75]. As we did not observe a difference between PWT and Chaplan up-down calculations, we present Chaplan up-down values. The von Frey hair estimated gf from the manufacturer can vary; thus, for each von Frey hair used we confirmed the gf using a balance (Ohaus, Adventurer SL).

### Data analysis

**Fibrosis onset analysis.** To directly demonstrate the expected probability that an animal will develop fibrosis with either the PRECLUDE + Teflon

AF or Kwik-Sil only methods, we constructed Kaplan–Meier survival curves using onset of fibrosis as the prognosis, for example, once we are no longer able to image the dorsal horn gray matter or extract usable data. To construct the Kaplan–Meier curves, we used ecdf in MATLAB and calculated the survivor function as $\hat{S}(t) = \prod_{t_i<t} \frac{r_i - d_i}{r_i}$, where $r_i$ is the number of mice at time $t_i$ and $d_i$ is the number of fibrosis mice at time $t_i$. We used censoring, where an animal's data are censored if either (1) the animal was perfused or died before the FOV was no longer visible due to fibrosis or (2) for animals that are still being imaged when we performed the Kaplan–Meier analysis and still did not have FOV covering fibrosis. We plotted the full Kaplan–Meier curves with censored data, indicated as the time the animal exited the study, in Extended Data Fig. 1l.

For Kwik-Sil-only mice, implant surgeries were performed exactly as for PRECLUDE + Teflon AF mice. One week after chamber implant during laminectomy operation, instead of placing the PRECLUDE membrane, we added Kwik-Sil over the exposed spinal cord, adhered a 3-mm glass coverslip to the Kwik-Sil and allowed 10 min to cure. Then we sealed the Kwik-Sil layer with cement or optical adhesive similar to the 'Window placement' procedure.

**Histological quantification.** For counts of microglial cells, we used a graphical user interface (GUI) (FIJI, ImageJ) to define a 300 × 300 μm$^2$ area that contained superficial and deep laminae of the dorsal horn. We used the Cell Counter plugin (FIJI) to count all EGFP+ cells within this area. We quantified four to eight spinal cord cross-sections spanning rostrocaudal segments of the implant for each animal. Quantified images had submicrometer pixel lateral resolution (0.62 μm per pixel).

**Open field analysis.** To analyze open field behavior, we trained a DeepLabCut (version 2.2.3) model using 20 manually annotated frames from three mice (60 total frames) with spinal chambers implanted. We selected frames based on visual appearance by using *k*-means clustering. We manually annotated the nose, torso (center, left and right) and tail (base, mid and tip). Training parameters were as follows: 600,000 iterations (Extended Data Fig. 3k); net type, resnet101; dataset augmentation, imgaug; global scale, 0.8; batch size, 1; fully connected parts; and GPU, NVIDIA A5000 (24 GB RAM). Model training and test errors, with a likelihood cutoff of 0.1, are 1.37 and 4.73 pixels. To confirm the accuracy of the model, we visually inspected by scrolling through annotated movies in our open field movie dataset, collected from the same arenas but using mice with and without spinal chamber implants. We imported body part locations from DeepLabCut comma-separated values (CSV) files into MATLAB using a custom CIAtah function. For a subset of videos we used an alternative ImageJ- and MATLAB-based algorithm for tracking mice that we previously developed and validated[76].

To evaluate locomotor speed, we calculated the speed between ($x$, $y$) point pairs between successive frames using the formula $v(t) = \frac{1}{r}\sqrt{(x(t) - x(t-1))^2 + (y(t) - y(t-1))^2}$, where $t$ is the frame, $r$ is the mean interframe interval time (s), and $x$,$y$ are the animal's position coordinates. We set the first frame's speed to zero to ease downstream computational analysis. We converted speeds to real units by calculating a pixel per cm conversion factor using a custom CIAtah GUI in which we selected a 60.96-cm distance for each video that corresponded to the diameter of the circular arena. To produce Fig. 1o, we took the mean speed over all the frames in a session.

**Behavior video analysis.** To track body parts in multicamera behavior videos, as in Fig. 5d,g, we trained a separate DeepLabCut (version 2.2.3) model for each camera, rather than a generalized model across all cameras. We used 20 manually annotated frames from each movie/camera for each model. We selected frames based on visual appearance by using *k*-means clustering to select frames from distinct clusters. Model training errors, with a likelihood cutoff of 0.1, are 1.04, 1.19, 1.1 and 1.14 pixel for bottom, face, left and right cameras, respectively. Model test errors, with a likelihood cutoff of 0.1, are 4.06, 7.66, 7.36, and 5.78 pixel for bottom, face, left and right cameras, respectively. Training parameters were as follows: 500,000 iterations (Extended Data Fig. 9b); net type, resnet101; dataset augmentation, imgaug; global scale, 0.8; batch size, 1; fully connected parts; and GPU, NVIDIA A5000 (24 GB RAM). We visually inspected the tracking afterward to confirm the general accuracy of the model, including when noxious stimuli were applied. For details on choosing body parts, see Supplementary Note 12.

We used the same method to calculate the speed as described in 'Open field analysis' section. To reduce the chance that we are using frames with suboptimal tracking, we only used frames with likelihood >0.1. We used objects (for example, objectives and blinders) with known size in the cameras' FOVs to calculate the estimated pixel to cm conversion factor, which we used to convert the $x$ and $y$ tracking from camera pixel to real units (cm). In certain cases—such as in Fig. 5g—to reduce the influence of small discrepancies in the frame-to-frame tracking, we smoothed the estimated body part speeds using a moving mean with a window of 5 s (100 frames).

**Calculating locomotor speed using rotary encoders.** The rotary encoder (Signswise, LN11-ERGA) outputs a signal (pulse) on two channels, A and B, each time it is moved in a clockwise (CW) or counterclockwise (CCW) direction. We calculated both directions of motion independently using the equations $\mathrm{CW} = (A > B) > (A(t+1) - A(t))$ and $\mathrm{CCW} = -1 \times ((B > A) > (B(t+1) - B(t)))$ where $A$ and $B$ are the vectors of rotary encoder pulses over all time points. We then combined them to obtain the total speed (that is, pulses output by the encoder) with $v(t) = |\mathrm{CW}(t) + \mathrm{CCW}(t)|$ over all frames. To calculate a conversion factor of 0.0691144 cm per pulse, we determined the circumference at the position on the running wheel, where the animal would be and divided it by the 600 pulses per 360° rotation of the rotary encoder or as a formula $C_p = \frac{2\pi r}{600}$ where $r$ is ~6.6 cm (radius from the center of running wheel to animal position). For display purposes, on some locomotor traces we downsampled the vector in time by binning the speed vector $v$ into evenly spaced groups of four frames and taking the mean within each group.

**Calculating locomotor speed in freely moving mice using accelerometers.** For miniature microscope imaging, we used the Inscopix data processing software 1.9.2 to convert accelerometer data in inertial measurement unit (IMU) files to CSV files. We imported CSV files into MATLAB, then calculated total acceleration using a previously described method[26], where the total acceleration is calculated as $A_t = \sqrt{(a_x)^2 + (a_y)^2 + (a_z)^2}$, where $a_x$, $a_y$ and $a_z$ indicate the $x$, $y$ and $z$ accelerometer output channels, respectively. We then reduced noise using a zero-phase low-pass filter (butterworth, 1 Hz cutoff, third order).

**$Ca^{2+}$ imaging data preprocessing with downsampling and detrending.** We processed $Ca^{2+}$ imaging data using CIAtah[36] and custom scripts in MATLAB (2022b, 2023b). In general, we performed the following steps: spatially downsampling (for a subset of movies), detrending, calculating motion transformation coordinates, spatial bandpass filtering, registering each frame to reference frame, adding fixed borders across all frames, fixing any problematic frames by setting their values to NaN, calculating relative fluorescence change and temporally downsampling (for a subset of movies). We detail each step below.

To increase the SNR and improve the processing speed, we spatially downsampled each frame in the $x$ and $y$ lateral dimensions by conducting 2 × 2 or 4 × 4 bilinear interpolation. To account for photobleaching during imaging, we detrended the $Ca^{2+}$ movies by calculating the mean for each frame, temporally ordered them from the first to last frame and then fit a first- or third-order polynomial curve to the fluorescent values. We then subtracted all pixels values in a given frame from the

fitted values at each time point and added the mean of all pixels in the movie, which detrended the movie while keeping the intensity values in a similar range as the raw movie and prevented the introduction of negative values.

**$Ca^{2+}$ imaging data preprocessing with motion correction and spatial filtering.** For movies that used rigid motion correction, we registered all frames to a reference frame using TurboReg[16]. We selected a subsection of the FOV with high-contrast features, such as dorsal veins and ascending venules, and minimal artifacts (such as bubbles or dust) that would affect registration. To improve motion correction, for each frame we subtracted the mean and then normalized the frame by subtracting it by a circular averaging filter (pillbox) of radius, one-tenth the minimum row or column length (whichever was smaller). Subsequently, we cross-correlated the entire frame with a circular average filter of disk radius 3 pixels. We then performed an image complementation by subtracting each pixel from the maximum value in the frame; this inverted the image making blood vessels used for registration more prominent. We obtained two-dimensional (2D) spatial translation coordinates for each frame from TurboReg by comparing it with a reference frame kept constant for all frames in the movie. To improve cell extraction, we divided each frame of the raw movie by a bandpass-filtered version of that frame (cutoff frequency of 0–10 cycles) that suppressed background fluctuations, such as occurs with neuropil. To avoid issues with filtering frames containing NaN values, we performed this step before movie registration. We then registered each frame using the 2D translation coordinates obtained for each frame from TurboReg. Due to differing amounts of motion correction across frames, which causes variable borders across frames, we added a fixed border for each frame in the movie by calculating the maximum motion and using that or 14 pixels, whichever is smaller. We calculated relative fluorescence using the following formula: $\frac{\Delta F(t)}{F_0} = \frac{F(t)-F_0}{F_0}$ where $F_0$ is either the mean image of the entire movie or the soft minimum image calculated as the value equivalent to the bottom 0.1% of pixels. Finally, for a subset of movies we temporally smoothed the movie by downsampling the temporal dimension fourfold. For an $x \times y \times t$ movie, this entailed bilinearly downsampling in $x \times t$ to minimize memory usage and improve processing times. This procedure is equivalent to performing a one-dimensional linear interpolation in time of the fluorescence intensity values of each pixel value. For a subset of movies that included areas outside the spinal cord in the imaging FOV, such as cement, we manually selected areas to keep and set all other areas to zero, which eliminated them from consideration during cell extraction. This method often improved the quality of extracted cells and reduced the number that needed to be manually curated post hoc.

For movies that used LD-MCM or displacement field motion correction, we performed similar preprocessing steps. Any deviations from the standard preprocessing are noted in their respective sections. To compare to LD-MCM and displacement field motion correction, we processed a subset of movies with NoRMCorre using our modified version of the repository (https://github.com/bahanonu/NoRMCorre) that only refactors the code into a namespace-safe package for integration into our codebase. We processed NoRMCorre motion corrected movies identically as described above and used default NoRMCorre parameters, as defined in the CIAtah function ciapkg.motion_correction.getNoRMCorreParams (from commit a2e72a8) with the following modifications: d1 and d2 are the input movie tensor dimensions and grid_size of (64 64 1) for a subset of movies.

**Motion correction of the spinal cord.** The spinal cord can experience several types of motion (Fig. 2a), including rapid, subsecond (Extended Data Fig. 5h) motion along with overlying features that contain no or different motion (for example, nonspinal vasculature, bubbles and so on). Our proposed workflow addresses these different situations and consists of a mixture of existing and new approaches that are within our CIAtah software or require use of external software for specific steps. The main decision points are whether the spinal cord movie is within or cross-session (Fig. 3d,e) and contains large rostrocaudal displacements (Fig. 2c) or nonuniform deformations (Fig. 2h). To handle large rostrocaudal displacement, especially when there are other overlying features, our LD-MCM fixes the large motion and subsequently uses rigid motion correction to fix smaller or subpixel motion. To handle deformation-based motion, we adapt existing displacement field-based motion correction methods followed by rigid registration. Note that if there is residual deformation or nonrigid motion after LD-MCM, then users can subsequently run the displacement field-based motion correction steps. We handle cross-session imaging via manual and automated alignment using our CS-MCM. The subsequent sections will give a detailed overview of each step in the workflow along with step-by-step procedures for performing each.

**Deep learning- and feature-based motion correction in LD-MCM.** The basis for LD-MCM is identification of movie features followed by control point motion correction. The use of deep learning-identified control points addresses a challenging situation for prior motion correction methods, both for applications to spinal cord imaging and to other situations in which optical windows are used to gain access to the body. These concerns include contamination of the FOV by objects that directly overlay the FOV and move differently from the primary tissue of interest—such as vasculature due to angiogenesis (Extended Data Fig. 8a), bubbles in silicone or other adhesives (for example, Kwik-Sil), cement or dust particles and other objects. For example, neovascularization or light fibrosis that overlaps with the FOV can impede motion correction as it can lead to algorithms using those as fiducials instead of the spinal cord. Although this limitation can be reduced by focusing down slightly more than desired to cause these elements to be further out of focus, this is not ideal and not possible in certain cases, while still collecting usable, high-quality data. LD-MCM helps mitigate the need to do this and provides superior performance. To consistently identify the same features (and without needing to conduct feature matching[77]), we took advantage of advances in deep learning that allow training of models with few examples to classify features. We use DeepLabCut[21] in this paper, but LD-MCM is agnostic to the feature identification method employed, except that it has the requisite accuracy to consistently identify features and generalize from the training set. Although these deep learning algorithms are often used to track animal body parts or items in the environment, most of these algorithms do not contain priors that would preclude their use for tracking vasculature or other features in the imaging data. These algorithms are thus agnostic to the feature being identified, as long as it has a consistent spatial structure across frames in a movie.

**The step-by-step procedure in LD-MCM.** The procedure for LD-MCM consists of the following procedures in MATLAB (using a mix of CIAtah and MATLAB built-in functions) and Python (for DeepLabCut analysis). To maintain consistency of pixel values and improve the accuracy of feature tracking, we used custom MATLAB scripts to convert raw $Ca^{2+}$ or Thy1–GFP movies from HDF5 (16-bit unsigned integer, uint16) to AVI (8-bit unsigned integer, uint8) format compatible with DeepLabCut. To avoid giving too much weight to outlier pixels, we calculated the soft maximum and minimum for each movie as the value equivalent to the 99.99th and 1th percentile of all pixel intensity values. We then convert using the following formulas: $M_1(t) = \frac{M(t)-\min(M)}{\max(M)-\min(M)}$ and $M_f(t) = (M_1(t) \times 2 - 0.01) \times 255$, where $M$ is the $x \times y \times t$ movie tensor. This creates a normalized movie that we then convert to uint8 units after shifting all values upward to avoid dark values that reduce feature identification accuracy. As we collected imaging data for some mice across multiple imaging cameras, which led to transformed FOVs, for certain movies we performed a 90° rotation and flipped the FOV to

align the FOV with the imaging session used for training data. To increase SNR, reduce training and analysis processing times and reduce file sizes, for a subset of mice we spatially downsampled their movies by the *x* and *y* lateral dimensions using 2 × 2 or 4 × 4 bilinear interpolation. We found that running on downsampled movies and then upsampling the feature tracking *x* and *y* lateral coordinates was faster and often worked better than running the downsampled movie-trained model on raw movies, probably owing to the decreased SNR of the raw movies. We then exported these movies as AVI files for use with DeepLabCut.

To consistently identify vascular features across frames and imaging sessions—see Supplementary Note 13 for details on feature selection and exclusion—we selected frames from a single imaging session for mice with large rostrocaudal motion based on visual appearance. Here we used *k*-means clustering to select frames from distinct clusters along with manual selection to include frames when the maximal motion occurs in the movie. The latter is due to their sometimes infrequent occurrence and we wanted to include those frames to have a robust training set. We then manually annotated key, stable vasculature within ~20 frames and used these to train a DeepLabCut (version 2.2.3) model. For mice used in Fig. 2 and Extended Data Figs. 5 and 10d, we used the following DeepLabCut training parameters: 500,000 iterations (Extended Data Fig. 5c); net type, resnet50 or resnet101; dataset augmentation, imgaug; global scale, 0.8; batch size, 1; fully connected parts; and GPU, NVIDIA A5000 (24 GB RAM). Model training errors with a likelihood cutoff of 0.1 are 0.96, 0.87, 0.96, 1.36 and 0.81 pixel across each of five mice. Model test errors with a likelihood cutoff of 0.1 are 2.45, 2.34, 3.97, 19.66 and 2.87 pixel across each of five mice. We used the resulting models to annotate the same vasculature in model-naive frames and movies (Fig. 3d and Extended Data Fig. 5a,b,f,g), then conducted visual inspection of tracking-annotated movies to additionally verify model accuracy across a variety of conditions, including those outside the training data (Extended Data Fig. 5f).

We imported feature locations from DeepLabCut CSV files into MATLAB using a custom CIAtah function. To compensate for rotated or flipped FOVs across imaging sessions, in certain mice due to the use of multiple cameras, for a subset of animal's videos we rotated and flipped the movie tensor as needed to match the orientation used for DeepLabCut tracking. We treated the resulting vascular tracking as control points. To reduce the influence of low-quality tracking on resulting translation matrix estimation, for each frame we only accepted features with tracking likelihood >0.99. We corrected for large shifts using point feature matching algorithms that estimates a 2D transformation matrix (*D*, using estgeotform2d in MATLAB). Although there is often nonrigid motion on top of the large rostrocaudal shifts, we used a rigid transformation—in contrast to similarity, affine or projective—as that allowed us to correct for the large shifts and then handle residual motion with other methods, while preserving the mass of the image and minimizing distortions. Using the other transformation types often produced warping (shear or tilting) and scaling of the motion-corrected frame, which are undesirable. We used 1,000 trials and used inliner pairs by only including those reference and motion frame point pairs that are within 20 pixels after applying the transformation. This method eliminates outliers that can otherwise reduce the accuracy of the registration. Before registration and to avoid issues with NaN value pixels, we correct for photobleaching and background fluorescence in $Ca^{2+}$ movies by detrending and spatially filtering movies as described in '$Ca^{2+}$ imaging data preprocessing with motion correction and spatial filtering' section. We then registered frames (imwarp in MATLAB) using *D* with linear interpolation.

We checked the stability of the resulting registered movie and then fixed residual motion owing to slight frame-to-frame variability in feature localization. To do this, we calculated the rigid transformation matrix (TurboReg) on a subsection of the FOV that was most stable and minimized overlapping features. We used TurboReg to estimate an affine transformation with no rotation or skew along with each frame being normalized as described previously (mean subtraction, image inversion and subtracting the movie by a 2D low-pass version of itself). We then registered the nonnormalized frames to the reference frame using the 2D transformation matrix (imwarp, to avoid issues with NaNs in the existing output). To improve registration in a subset of movies, we separately conducted LD-MCM motion correction of the left and right spinal cord and then combined the results before further downstream analysis.

**Performance of LD-MCM compared with the number of features used.** To determine the relationship between the number of features used with LD-MCM and the motion correction performance, we re-ran the control point registration while limiting the number of features available to LD-MCM. For all movies used in Fig. 2f, we gave LD-MCM from 2 to 13 features. We ran three rounds of LD-MCM for each movie and feature number while randomly subsampling the available features each round. We outputted the resulting movies and tracked the features across all frames. We then calculated the median, mean and standard deviation displacement from the median location of the feature for each feature in the movie. We then took the mean of each measure across all features for each parameter sweep movie to produce Extended Data Fig. 5j.

**An overview of the deformation correction using diffeomorphic registration.** The spinal cord can sometimes have nonrigid motion, such as motion where separate areas of the spinal cord move semi-independently of one another (Fig. 2a). Nonrigid motion correction can fix these issues but raises additional challenges as it is computationally more challenging compared to rigid movement. We take advantage of demons algorithm-based methods[15] that use displacement fields to minimize errors between a reference and motion image (Fig. 2g). To reduce artifacts induced by spatial or other filtering after motion correction, we then incorporated these methods within our existing motion correction pipeline for preprocessing before motion correction. By testing these methods with our spinal imaging dataset, we demonstrated that these methods can help correct motion in the spinal cord (Fig. 2h). It should be noted that many deformation correction algorithms can be much slower than rigid or patch-based motion correction and thus it is advisable to run motion correction on a subset of movies or frames before running on an entire dataset.

**Step-by-step deformation correction using diffeomorphic registration.** We load movie tensors (MATLAB) and detrend as previously described in '$Ca^{2+}$ imaging data preprocessing with downsampling and detrending' section. To reduce the influence of background fluctuations, we then normalized each frame by subtracting the frame by a version of the image cross-correlated with a circular averaging filter (pillbox) of radius, one-tenth the minimum row or column length (whichever was smaller). The resulting modified frame matrix was then cross-correlated by a circular average filter of radius 3 pixels. We calculated the *x* and *y* lateral displacement fields (imregdemons in MATLAB) using existing demons algorithm-based methods to estimate the displacement fields[15]. Parameters for imregdemons are three pyramidal levels, with 2,000, 400 and 100 iterations for each level and accumulated field smoothing of 1.5. We then discarded the modified movie tensor. To improve cell extraction, we then divided each frame of the raw movie by a bandpass-filtered version of that frame (cutoff frequency of 0–10 cycles) that suppressed background fluctuations, such as neuropil. We performed this step before registration to avoid issues with filtering frames containing NaN values. Visual inspection and quantitative feature tracking with LD-MCM indicated that in our movies the majority of spinal cord motion is rostrocaudal (Fig. 2c,e and Extended Data Fig. 5e). Thus, we set the mediolateral displacement fields to zero before image registration. This method reduced the introduction of improper mediolateral shifts, especially during times

of high neural activity. We applied the modified displacement field to the processed movie using linear interpolation (imwarp in MATLAB), resulting in a movie that closely matched the template (Fig. 2g). We visually checked the resulting movies and then reduced residual motion in the movies with rigid (TurboReg) motion correction.

Beyond comparing displacement field motion correction with NoRMCorre and TurboReg, we further tested using another recent patch-based nonrigid registration method PatchWarp[78]. We used our slightly modified implementation that reduced memory overhead and improved parallelization performance (https://github.com/bahanonu/PatchWarp). However, we found that PatchWarp introduced blurring and the patches were visible after taking the standard deviation of the temporal dimension of each movie (Extended Data Fig. 6a). As the blurring would function as a low-pass filter and artificially raise the 2D correlation coefficient, we omitted PatchWarp from correlation-based analysis. We used the default PatchWarp parameters in patchwarp_demo (commit a4a69ed) with the following changes: rigid_template_tiffstack_num = 1, rigid_template_block_num = 1, warp_template_tiffstack_num = 1 and network_temp_copy = 0.

Displacement field motion correction can be applied after LD-MCM for cases in which, after large shifts are corrected, there is still residual nonrigid motion that needs to be corrected. However, care must be taken as the prior issue of obstructive overlying layers can lead to suboptimal displacement field motion correction results.

**Extraction of neuronal shapes, locations and activity traces from calcium imaging data.** After processing each session's $Ca^{2+}$ imaging videos, we extracted the neuronal shapes and activity traces using existing cell extraction algorithms. We first attempted to use the widely used PCA-ICA (PCA, principal component analysis; ICA, independent component analysis) algorithm[79] using $\mu = 0.1$, a termination tolerance of $5 \times 10^{-6}$ and maximum iterations of 1,000. We found that, when using PCA-ICA, many of the ICA spatial filters included spatial information from multiple cells in the movie. This is probably due to the highly correlated activity of $SCPN^{Phox2a}$ recorded during stimulus application, especially under anesthesia, where the baseline activity is reduced, and neuron cell bodies are close to one another. To minimize the potential confounds that this causes, we also tested two other cell extraction methods: CELLMax based on maximum likelihood[80,81] and EXTRACT based on robust statistics[82]. These methods reduce cross-talk and produce spatial filters that closely match the shape of the recorded cells. In the figures herein, we display CELLMax spatial filters and neural activity (GCaMP6s/f) traces. We used the following CELLMax parameters (listing major ones changed from default): percent frames per iteration, 0.5–0.7; gridSpacing, 18; gridWidth, 10; movieImageCorrThreshold, 0.2; and downsampleFactorTime, 10–40. To transform CELLMax-scaled probability activity trace outputs to estimated GCaMP6s/f $\Delta F/F$ activity traces (or more generally movie units), we multiplied each scaled probability output by the maximum pixel intensity value of its corresponding spatial filter.

Cell extraction algorithms produce false positives—such as other sources of signal within the movie (neuropil, blood vessel artifacts and so on) or noise—that need to be eliminated (Extended Data Fig. 10b). Although it is possible to calculate certain parameters (SNR of activity trace, rise and decay times of $Ca^{2+}$ transients and so on) and apply heuristics to eliminate cells, this can lead to many false negatives for cells that do not meet prior assumptions. As we are interested in capturing as many true cells as possible, we manually classified every output cell throughout the paper, unless otherwise specified, using a custom GUI in CIAtah. We used criteria, such as algorithm source image shape (for example, solid circular 2D Gaussian blob for one-photon imaging), existence of identifiable events in the $Ca^{2+}$ imaging movie that matched transients within the algorithm's output cell activity trace and other features. Future work can use CLEAN (cell extraction automated classification) or other automated cell classification methods[81].

**Calculating blood vessel diameter and fluorescence in anesthesia and awake imaging experiments.** To calculate the blood vessel diameter during the transition from awake to anesthesia (Fig. 3p and Extended Data Fig. 8c–e), we first bandpass filtered the data to remove fluctuations in background intensity during imaging. We normalized each frame between zero and one using the formula $M(t) = \frac{M(t) - \min(M(t))}{\max(M(t)) - \min(M(t))}$. To improve consistency of vessel estimates across frames, we matched the histograms between each frame and a reference image and then multiplied all values by 150. To enhance the dorsal vein and ascending venules, we used Hessian-based Frangi vesselness filtering with FrangiFilter2D in MATLAB (https://www.mathworks.com/matlabcentral/fileexchange/24409-hessian-based-frangi-vesselness-filter). This method highlights the blood vessels in the movies and suppresses other nonvascular signals[83,84]. Parameters used: sigma range of 1–20, step side between sigmas of 2, Frangi $\beta_1$ correction constant of 0.5, Frangi $\beta_2$ correction constant of 15 and detect blade ridges. We exported movies for processing in ImageJ.

For a subset of the movies, we applied a $2 \times 2$ median filter. We then thresholded each frame (setThreshold $(0.03, 1 \times 10^{30})$ and 'Convert to Mask') and then selected a subsection of the FOV around the dorsal vein to process. We passed the resulting movie to the FIJI plugin Local Thickness (see https://imagej.net/imagej-wiki-static/Local_Thickness and ref. 85), with a threshold of 40 or 80, depending on the movie. To avoid the algorithm introducing temporal correlations into the local thickness calculations, we calculated local thickness for each frame independently. Otherwise the method will interpret the third-order spatiotemporal tensor with dimensions $x \times y \times t$ as a third-order spatial tensor with dimensions $x \times y \times z$. We then manually selected a region of the dorsal vein or ascending venules and calculated the mean thickness. To display diameter relative to the start of the imaging session for the animal in Fig. 3p and Extended Data Fig. 8d,e, we normalized both fluorescence and blood vessel diameter to the first 4 min of the imaging session during which time the animal was awake.

To calculate the cross-session registration correlation, we used Frangi vesselness filtering previously described on the Thy1–GFP-M and $CX_3CR1$–EGFP mice. This method made it possible to obtain a representation of each session's frames that are less influenced by changes in baseline or other (for example, neural activity) fluorescence.

**Analysis of spinal cord somatotopy.** To create the mean contour map and to reduce noise, easing visualization, we median filtered the mean projection image. To calculate contour lines, which indicate the relative location of fluorescence, after thresholding images we used two ImageJ plugins, https://imagej.nih.gov/ij/plugins/contour-plotter.html (now https://imagej.net/ij/plugins/contour-plotter.html) and https://imagej.net/imagej-wiki-static/Contour_Lines. We only included contour lines that mapped onto the outermost edge of the bulk GCaMP6s activity and used GIMP (2.10.22), so as to create transparent overlays.

**An overview of CS-MCM.** CS-MCM involved a single manual and multiple automated steps. We performed the manual correction primarily to reduce the search space and complexity of the motion correction for the automated portions. Thus, the manual alignment is normally only needed in situations where there are large translational or rotational shifts with obstructing elements (or reorientations of the FOV, such as vertical or horizontal axis flips due to camera changes) that might make it difficult for automated motion correction to fix or if there are more biologically relevant areas of the FOV that need correction. To manually correct for large shifts that occurred, sometimes due to shifting of the spinal cord across sessions, which resulted in a permanent change in the FOV through the laminectomy area, we developed a custom manual motion correction GUI within CIAtah. The GUI displays a mean frame for a reference and the current movie and allows for translations (rigid using imwarp in MATLAB on each click by users) as well as the ability

to rotate and flip the FOV to accommodate changes in the FOV due to acquiring movies with multiple cameras for certain mice. To improve cross-session correction, we then perform within-session motion correction, which first reduces any motion within a movie. This correction leads to higher contrast (less blurry) mean frames for each movie, which we then use for cross-session motion correction. As we also demonstrated that we can use LD-MCM for feature identification and initial motion correction across sessions (Fig. 3d, Extended Data Fig. 5g and Supplementary Video 10), it is possible to automate the manual step. When attempting cross-session experiments, it is preferred that the camera, objective, LED/laser power and other settings are maintained to improve the chance of successful registration and allow quantitative comparison across imaging sessions. We then conducted multiple rounds of rigid registration both within and across imaging sessions, followed by a final round of motion correction across all frames in all sessions. These final steps create the desired cross-session motion-corrected movie (Supplementary Video 10).

**The step-by-step process for CS-MCM.** To correct for differences in frame size across cameras, which can introduce computational difficulties, we padded the $x$ and $y$ lateral dimensions of each frame with zero-value pixels. Thus, all frames across all imaging sessions matched the frame with the maximum $x$ and $y$ dimensions. The matrix is loaded into the manual CIAtah GUI and we manually corrected the motion using vasculature or other biological features (for example, axons in Thy1–GFP mice) as references. We then performed rigid motion correction within each session using TurboReg on a subsection of the FOV as described in '$Ca^{2+}$ imaging data preprocessing with motion correction and spatial filtering' section, leading to a stable movie for each imaging session. Next, to speed up registration, we conducted cross-session motion correction between frames consisting of the mean frame, calculated across all temporal pixels, for the current and a constant reference session (Fig. 3d). To further improve registration, we performed affine-based registration without rotation or skew followed by an additional affine-based registration with rotation and no skew. We used the following TurboReg parameters: 30-pixel $x$ and $y$ smoothing, 6 pyramid levels, normalization with mean subtraction followed by pillbox disks of radii 20 (for subtraction) and 10 (on post-subtraction frame) and used the transfturboreg function (instead of imwarp) for image transformation. Lastly, to further refine the alignment, we concatenated the $x \times y \times t$ movie tensors from all $N$ imaging sessions into a $x \times y \times (t \times N)$ movie tensor, then conducted TurboReg motion correction on the combined movie, using the same reference frame for all frames (Fig. 3e). These movies were then used to conduct downstream analysis, such as calculating changes in $CX_3CR1$–EGFP fluorescence over time (Fig. 6h–j).

**Cross-session cell identification.** To align cells across imaging sessions in the most computationally efficient manner, after performing cell extraction and manual curation, we performed motion correction and cross-session alignment. We have previously shown that this is a fast and reliable method of cross-session alignment and reduces the computational complexity and memory requirements that occur with directly registering the movie tensors[26,36]. We used the computeMatchObjBtwnTrials module within CIAtah to align cells across sessions with the following parameters: TurboReg motion correction with affine transformations (rotation enabled and skew disabled) or nonrigid displacement field-based motion correction (see the displacement field motion correction section), one or five rounds of motion correction consisting of sequential centroid- and cell shape-based registration, centroids greater than 5 or 15 pixels distance are not matched and cell shapes must have an image correlation >0.6 to be matched.

With months-long imaging, the spinal cord can grow and deform, leading to a difference in the distance between the strip of cells on the left and right side of the spinal cord. When registering cells from both sides simultaneously, this shift can reduce the accuracy of cross-session registration. To get around this issue, we registered the left and right sides of the spinal cord separately by removing cells on the contralateral spinal cord using a custom GUI added to the computeMatchObjBtwnTrials CIAtah module. To allow visualization of cross-session matched cells, we then colored coded matched cells based on their global cell identification number across imaging sessions, and cells without cross-session matched data are colored gray. For Fig. 5i, we display the −8 to 8 s interval around stimulus onset taken as the mean response of each global cell across all applicable stimuli, excluding stimuli with another stimuli given within 8 s before to allow for a more consistent baseline period. For the summary charts, we display the $\Delta F/F_0$ difference between the post- (0 to 2 s) and pre- (−4 to 0.25 s) stimulus time periods for each cell on each day. We sorted cells based on total post noxious heat $\Delta F/F_0$ intensity across all days identified, then sorted the top 30 cells based on the number of sessions they were active for; this was repeated for the remaining cells for noxious cold and the combined cell ordering maintained across both stimuli heat maps.

**Cross-session fluorescence intensity.** To demonstrate the consistency of imaging over time, we used fluorescence intensity as this will change as optical clarity is reduced, for example, fibrosis is anticipated to and often caused a drop in fluorescence intensity. For each animal, we took six frames from the 2 × 2 binned widefield imaging movie and then calculated the mean intensity over all pixels in all frames. For certain sessions, where no movie is available, we used the single frame 2 × 2 binned widefield reference image collected during each day of imaging. To compensate for changes in fluorescence intensity values across multiple CCD and sCMOS cameras used in the study during one-photon imaging, we attempted two methods. For the first, main method used, we normalized each curve by calculating the mean fluorescence intensity for each animal for each camera (and the camera mode used for that animal, for example, sensitivity versus dynamic range) and divided all intensity values associated with each camera to its own mean intensity to produce the final displayed curves (Figs. 3f, 5c and 6e). The second method is described in Supplementary Note 14.

**Microglial analysis after nerve injury.** To calculate relative changes in microglia activity before and after nerve injury, we performed CS-MCM on each animal, as described in prior sections, using five frames taken from each imaging session's 2 × 2 binning acquired movies. We then manually selected rectangular regions on the left and right side of the spinal cord, excluding areas that were outside the FOV or were substantially blocked by cement or other overlying features. We cropped the movie to these left and right side regions, then calculated the mean of all pixels on each $x \times y$ frame, which created a $1 \times (tN)$ vector, where $N$ is the number of imaging sessions. Next, we calculated the mean on each $1 \times t$ vector for each movie. For injured mice, we calculated the ratio of the ipsilateral and contralateral side, using the formula $R(t) = \frac{F(t)_{\text{ipsi}} - F(t)_{\text{contra}}}{F(t)_{\text{ipsi}} + F(t)_{\text{contra}}}$ for each frame (Fig. 6i,j). For naive mice, we arbitrarily chose a side as 'ipsi' and used the same calculation. To compare across mice that had different baseline ratios between the fluorescence on the left and right spinal cord, we normalized curves in Fig. 6i,j by subtracting all values for a given animal by the mean value of all baseline sessions for that animal.

## Statistics and reproducibility

We conducted statistical analysis in RStudio (1.4.1106) using R (4.1.0). We created Figs. 1o–q and 6f, and Extended Data Fig. 3l using the R library ggplot2. We indicate significance in figures using the following nomenclature: $^{***}P < 0.001$, $^{**}P < 0.01$ and $^{*}P < 0.05$.

To assess impact on general locomotion (Fig. 1o), we performed a one-way analysis of variance (ANOVA) ('aov' in R) on the mean locomotor speed in the open field, with groups consisting of

pre- and postsurgery mice. We saw a significant effect of surgical state ($F_{4,48} = 3.53$, $P = 0.0133$*). We then performed post hoc analysis with a Dunnett's test comparing each postsurgery condition with the presurgery baseline and found a significant decrease after implant ($P = 0.0186$) but not after laminectomy ($P = 0.9368$) or early ($P = 0.6016$) and late ($P = 0.2176$) after window placement. To assess the impact on coordinated locomotor behavior (Fig. 1p and Extended Data Fig. 3l), we performed a two-way ANOVA, which evaluated the effect of surgery state and trial on latency to fall. We found an effect only on trials ($F_{2,118} = 4.03$, $P = 0.0203$*) but not on surgical state ($F_{7,118} = 1.981$, $P = 0.0633$) or interaction between surgical state and trials ($F_{14,118} = 0.378$, $P = 0.9786$). We then performed a one-way ANOVA within each trial so as to only compare the surgical states, followed by a post hoc Dunnett's test comparing each surgical state with presurgery baseline. We excluded mice that exhibited signs of leg paralysis and were thus unable to perform the task. To determine whether spinal chamber implantation impacted mechanical sensitivity (Fig. 1q), we performed a two-way ANOVA comparing interaction between surgical state and hindpaw, finding both to be nonsignificant ($F_{4,98} = 0.140$, $P = 0.967$ and $F_{1,98} = 0.007$, $P = 0.932$). We then performed a one-way ANOVA, where we found no effect on either hindpaw ($F_{4,49} = 0.495$, $P = 0.739$ and $F_{4,49} = 0.694$, $P = 0.599$ for left and right, respectively), followed by a post hoc Dunnett's test comparing each group with presurgery baseline. We excluded data points for $CX_3CR1$–EGFP mice after they had nerve injury as that would confound interpretation due to hypersensitivity. For trial 3 shown in Fig. 1p, we found no significant difference between baseline and implant ($P = 0.7571$), laminectomy ($P = 0.7383$) and the window at days 0–30 ($P = 0.8640$), 30–60 ($P = 0.8180$), 60–90 ($P = 0.1736$), 90–120 ($P = 0.1537$) or 120+ ($P = 0.0587$). We did find a significant decrease in trial 2 comparing baseline to post window day 120+ ($P = 0.01$*) but did not find a significant change comparing baseline with other postsurgery time periods in trials 1 and 2.

To compare LD-MCM rostrocaudal displacement with other methods (Fig. 2f), instead of having to perform a statistical test of difference in variance between samples (for example, Levene's test), we transformed the data by computing the absolute difference in distance for each feature and time point from its mean location for that animal's imaging session. We then computed the mean over all frames for a given session and performed statistics on these values. Next, we performed a one-way repeated measures ANOVA, finding a significant effect of algorithm ($F_{3,8} = 5.68$, $P = 0.0221$*), followed by a post hoc Dunnett's test comparing each method with LD-MCM. We found LD-MCM to have significantly reduced motion compared with raw ($P < 0.0001$***), TurboReg ($P < 0.0001$***) and NoRMCorre ($P < 0.0001$***). To compare displacement field motion correction mean frame correlation coefficient, used as a measure of the reduction in spinal cord nonrigid motion (Fig. 2k), we took the mean of all frames for each imaging session and then conducted a one-way ANOVA by method, finding a significant effect ($F_{3,8} = 16.14$, $P = 0.000936$***), followed by a post hoc Dunnett's test comparing each method with displacement field motion correction. We found LD-MCM to have significantly reduced motion compared with raw ($P = 0.0002$***), TurboReg ($P = 0.0105$*) and NoRMCorre ($P = 0.0009$***).

To directly assess von Frey mechanical sensitivity (Fig. 6f), we performed a two-way ANOVA looking at the interaction between the surgery groups (for example, SNI or sham and contra- or ipsilateral hindpaw) and surgical state, finding a significant interaction ($F_{2,5} = 29.9$, $P = 0.00165$**). We then conducted a paired *t*-test comparing before and after surgery across each hindpaw and surgery group (SNI or sham) with multiple comparisons correction using the Holm–Bonferroni method. We found only the SNI group on the ipsilateral hindpaw showed a significant change ($P = 0.005025$**) but no change for SNI contralateral ($P = 0.7617$), sham contralateral ($P = 0.348$) or sham ipsilateral ($P = 0.874$).

We ran or compiled code in MATLAB (2022b, 2023b and occasionally 2021b), Python (3.9.12) using the Anaconda (4.12.0) environment, RStudio (1.4.1106), R (4.1.0 and 4.0.2), ImageJ (1.53d), FIJI (1.53q), Saleae Logic (various iterations of version 2, for example, 2.4.6) and the Arduino IDE (1.8.13 and 2.0). We converted between file containers (for example, AVI to MP4) using ffmpeg (version 2020-10-21-git-289e964873). We created surgery videos using Adobe Premiere Pro (version 24.1.0, build 85). We ran image acquisition and conducted data analysis on computers running Windows 10 and, for a subset of histological images, using macOS. We acquired imaging data using 3i SlideBook 6, Zeiss Zen (3.2.090), µManager 2.0.0 or Olympus LSM FV3000 (2.3.2.169).

### Reporting summary

Further information on research design is available in the Nature Portfolio Reporting Summary linked to this article.

## Data availability

The 3D STL and STEP files of the side bars and stabilizing plate along with a 3D model and TIFF stack of the entire mouse body from one of our microCT scans (Fig. 1a) can be found via GitHub at https://github.com/basbaumlab/spinal_cord_imaging and Zenodo at https://doi.org/10.5281/zenodo.11660130 (ref. 86). Any future updates to the design or additional files will be published on those repositories. Due to dataset size, raw imaging data are available from the authors upon request.

## Code availability

Code for processing $Ca^{2+}$ imaging data is available as part of the CIAtah software package under an MIT license (see LICENSE file) via GitHub at https://github.com/bahanonu/ciatah. Code for LD-MCM (feature identification followed by control point motion correction), deformation correction using displacement fields and CS-MCM (cross-session motion correction) is integrated into CIAtah and any future updates will be published on that repository.

## References


71. Feng, G. et al. Imaging neuronal subsets in transgenic mice expressing multiple spectral variants of GFP. *Neuron* **28**, 41–51 (2000).
72. Fenno, L. E. Comprehensive dual- and triple-feature intersectional single-vector delivery of diverse functional payloads to cells of behaving mammals. *Neuron* **107**, 836–853.e11 (2020).
73. Feldkamp, L. A., Davis, L. C. & Kress, J. W. Practical cone-beam algorithm. *J. Opt. Soc. Am. A* **1**, 612–619 (1984).
74. Bonin, R. P., Bories, C. & De Koninck, Y. A simplified up-down method (SUDO) for measuring mechanical nociception in rodents using von Frey filaments. *Mol. Pain* **10**, 26 (2014).
75. Chaplan, S. R., Bach, F. W., Pogrel, J. W., Chung, J. M. & Yaksh, T. L. Quantitative assessment of tactile allodynia in the rat paw. *J. Neurosci. Methods* **53**, 55–63 (1994).
76. Li, Y. et al. Neuronal representation of social information in the medial amygdala of awake behaving mice. *Cell* **171**, 1176–1190.e17 (2017).
77. Liu, W. et al. Fast and accurate motion correction for two-photon $Ca^{2+}$ imaging in behaving mice. *Front. Neuroinform.* **16**, 851188 (2022).
78. Hattori, R. & Komiyama, T. PatchWarp: corrections of non-uniform image distortions in two-photon calcium imaging data by patchwork affine transformations. *Cell Rep. Methods* **2**, 100205 (2022).
79. Mukamel, E. A., Nimmerjahn, A. & Schnitzer, M. J. Automated analysis of cellular signals from large-scale calcium imaging data. *Neuron* **63**, 747–760 (2009).
80. Kitch, L. J. *Machine Learning Meets Mammalian Learning: Statistical Tools for Large-Scale Calcium Imaging and the Study of Changing Neural Codes*. PhD thesis, Stanford Univ. (2015).

81. Ahanonu, B. O. *Neural Ensemble Dynamics in Behaving Animals: Computational Approaches and Applications in Amygdala and Striatum*. PhD thesis, Stanford Univ. (2018); https://doi.org/10.25740/vh359hb5216
82. Dinc, F. et al. Fast, scalable, and statistically robust cell extraction from large-scale neural calcium imaging datasets. Preprint at *bioRxiv* https://doi.org/10.1101/2021.03.24.436279 (2021).
83. Frangi, A. F., Niessen, W. J., Vincken, K. L. & Viergever, M. A. in *Medical Image Computing and Computer-Assisted Intervention—MICCAI'98* (eds Wells, W. M. et al.) 130–137 (Springer, 1998).
84. Longo, A. et al. Assessment of hessian-based Frangi vesselness filter in optoacoustic imaging. *Photoacoustics* **20**, 100200 (2020).
85. Dougherty, R. & Kunzelmann, K.-H. Computing local thickness of 3D structures with ImageJ. *Microsc. Microanal.* **13**, 1678–1679 (2007).
86. Long-term optical imaging of the spinal cord in awake, behaving animals: design files and microCT data. *Zenodo* https://doi.org/10.5281/zenodo.11660130 (2024).

## Acknowledgements

We thank the following colleagues for materials and assistance. A. Nimmerjahn and D. Duarte (Salk Institute) for demonstrating their spinal cord setup. A. Gottlieb and Random Technologies for generously gifting Teflon AF material. D. Bernards and T. Desai (UCSF) for helping with the plasma treatment of Teflon AF. Y. Seo and R. Tang (UCSF) for help conducting microCT experiments in the MicroPET/CT, MicroSPECT/CT, MicroCT and Optical Imaging center. MicroCT experiments reported in this publication were supported in part by the Office of the Director, NIH under grant S10OD012301. D. Larson (UCSF) for help optimizing one- and two-photon imaging and microscope maintenance. Data were collected at the Center for Advanced Multiphoton Microscopy with support from the Kavli Institute. K. Herrington and S. Yeon Kim (UCSF) for microscope testing and maintenance help. B. Tiret, P. Schuette and Inscopix, a Bruker company, Mountain View provided the LScape module for nVue 2.0 system. We thank S. Ho (UCSF, Biomaterials and Bioengineering Correlative Microscopy Core) and B. Lee (UCSF) for helping collect scanning electron micrographs of Teflon AF 2400 and PRECLUDE. E. Lam (UCSF) provided help and advice on machining and 3D printing. We thank the following people for reagents and mice. D. McDonald and P. Baluk (UCSF) provided low-magnification objectives. S. Puente and I. Delgado of VICI Metronics helped distribute Teflon AF. W. Xin and J. Chan (UCSF) provided Thy1–YFP-H mice. H. Su and R. Liang (UCSF) provided Thy1–GFP-M mice. B. Roome (McGill University) sent the Phox2a–Cre mouse line. This work was supported by NIH NSR35097306 (A.I.B.), Open Philanthropy (A.I.B.), DARPA 9691 (A.I.B.), HHMI Hanna H. Gray Fellowship (B.A.), NIH R35 NINDS Supplement Funding (B.A.), NIH F32 5F32DE029384 (A.C.), Canadian Institutes of Health Research (PJT-162225, MOP-77556, PJT-153053 and PJT-159839) (A.K.) and NSF Graduate Research Fellowship 2034836 (M.R.C.).

## Author contributions

B.A., A.C. and A.I.B. designed the project and wrote the manuscript. A.C. and B.A built the instrumentation for surgery and imaging and developed the surgical and imaging protocols. A.C. and B.A. performed surgeries, histology, imaging, image processing and data analysis. B.A. developed and tested the motion correction algorithms and performed animal behavior. M.R.C. assisted with experiments and manuscript preparation and created the supplementary surgery videos. A.K. provided the Phox2a–Cre mouse line.

## Competing interests

The authors declare no competing interests.

## Additional information

**Extended data** is available for this paper at https://doi.org/10.1038/s41592-024-02476-3.

**Supplementary information** The online version contains supplementary material available at https://doi.org/10.1038/s41592-024-02476-3.

**Correspondence and requests for materials** should be addressed to Allan I. Basbaum.

**Peer review information** *Nature Methods* thanks the anonymous reviewers for their contribution to the peer review of this work. Primary Handling Editor: Nina Vogt, in collaboration with the *Nature Methods* team.

https://doi.org/10.1038/s41592-024-02476-3

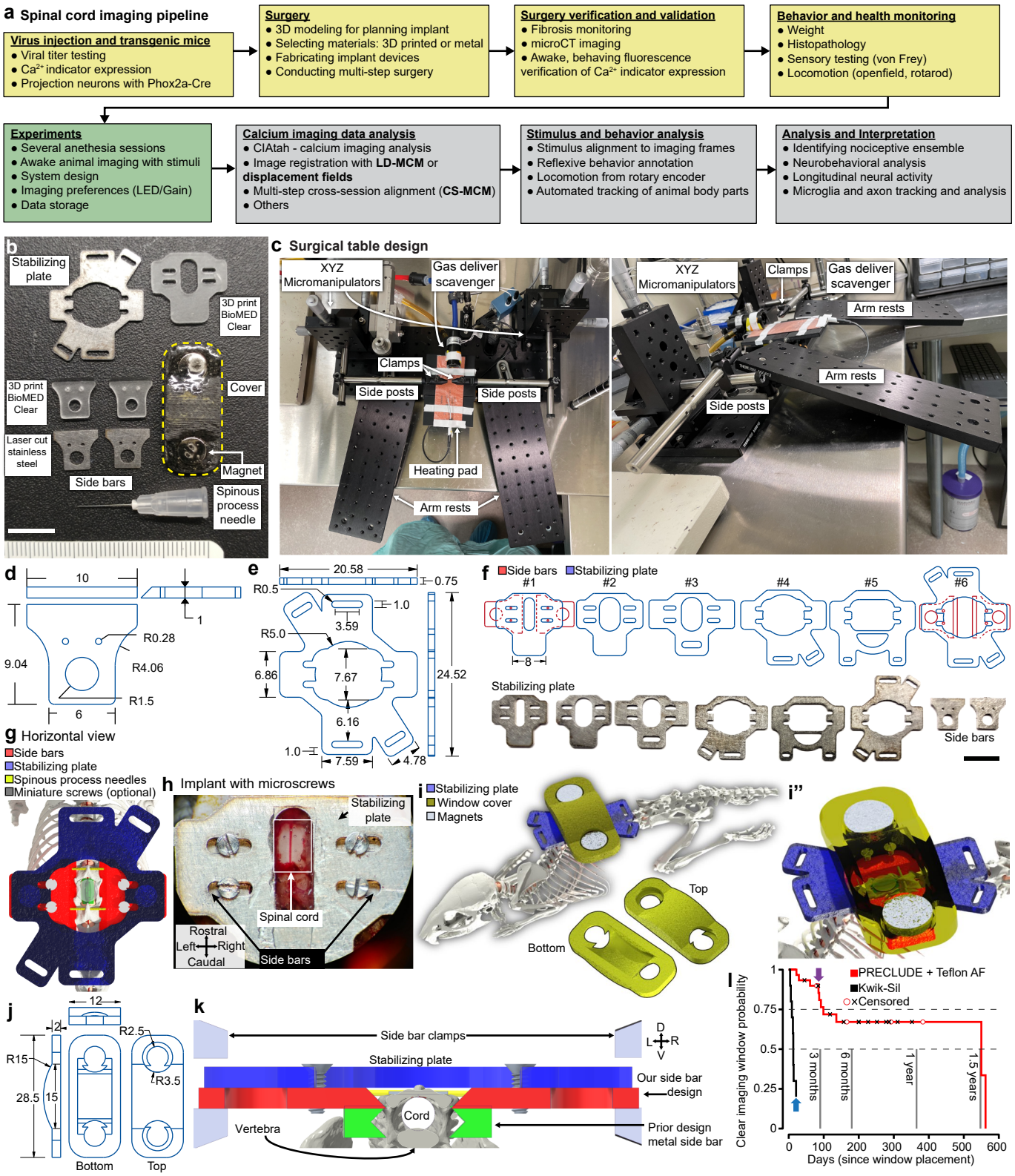


**Extended Data Fig. 1 | See next page for caption.**

https://doi.org/10.1038/s41592-024-02476-3

**Extended Data Fig. 1 | Awake spinal imaging experimental overview and designs. a**, Spinal cord imaging workflow. Several steps, such as microCT validation, are optional. **b**, Spinal implant chamber components: 3D printed and laser cut stainless or mild steel side bars, stabilizing plates, and the protective snap-on cover. Scale bar, 1 cm. **c**, Spinal cord surgery setup made from commercially available components and 3D printed parts, see Supplementary Table 4 for a parts list. **d**, Side bars technical diagram; units in mm. **e**, Stabilizing plate technical diagram; units in mm. **f**, Several (#1–6) iterative designs (top row, CAD; bottom row, real image) of the stabilizing plate with different positioning of the clamping/handling tabs. Side bars are included for size comparison. Scale bar, 1 cm. **g**, Horizontal view of the spinal cord implant chamber and optional screws (3D model). **h**, Spinal implant chamber (see **f**) with miniature screws. **i**, Protective cover for the spinal window (3D model); colors as in Fig. 1a. **i"**, magnified view of the cover (semi-transparent for visualization) on the spinal implant. **j**, Technical diagram of side bar cover; units in mm. **k**, Coronal view of an implant. Screws are optional. Note the dorsal-oriented attachment of the metal chamber components (red and blue pieces) to the T12-L1 vertebrae, compared to prior strategies (green pieces). Side clamps are used to manipulate the chamber during surgery and imaging. Colors for items are the same as in Fig. 1a. **l**, Survival curves (Kaplan-Meier estimator), as in Fig. 1g, illustrate the fibrosis onset probability PRECLUDE + Teflon AF (n = 36) or only Kwik-Sil (n = 10) surgeries; Kwik-Sil curve is not at zero (blue arrow) as n = 2 mice were fibrosis free or deceased at time of analysis. Censored data points indicate mice that died (X) or are still alive (circle) at the time of analysis. The purple arrow indicates time points with multiple alive mice.

https://doi.org/10.1038/s41592-024-02476-3

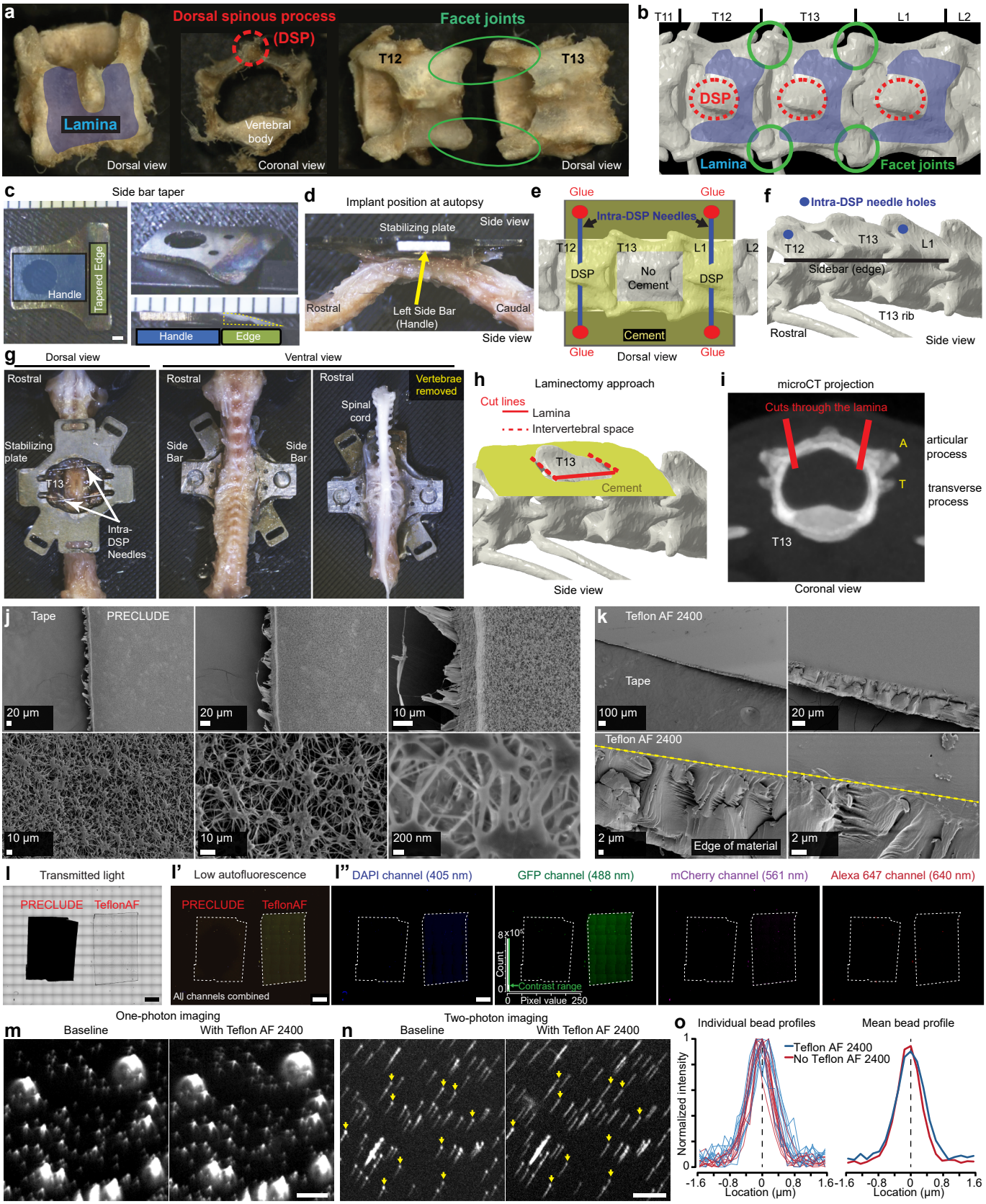


**Extended Data Fig. 2 | See next page for caption.**

https://doi.org/10.1038/s41592-024-02476-3

**Extended Data Fig. 2 | Blueprint of chamber implantation and fluoropolymer characterization. a**, Vertebral anatomy, using actual mouse vertebrae, critical to the chamber implantation procedure, including the lamina (blue shading), dorsal spinous process (DSP, red circle), and facet joint (green circle). **b**, Horizontal view of the T12-L1 vertebrae of the spinal column (3D microCT reconstruction). Note: only the two circled facet joints are surgically exposed and rest above the side bars after correct placement. **c**, Side bar edges are manually tapered by a grinding wheel before implantation. Scale bar, 1 mm. **d**, Side view showing an implant. Note the dorsal-oriented attachment of the side bar. **e**, Spinal process needles are superglued to the side bars (red dots) and dental cement covers the implant (yellow) with the T13 lamina kept cement free for laminectomy. **f**, Spinal process needles bore through the DSP of T12 and L1 (solid blue circles). **g**, Spinal column dissection of a chamber-implanted mouse showing chamber components placement at T13. **h**, The lateral offset (solid red line) of the laminectomy is critical for dorsal horn imaging. **i**, Cross-section of the T13 vertebra (microCT micrograph). Red lines: lateral extent to which the T13 lamina is transected during laminectomy, to access the dorsal horn. **j**, Scanning electron micrographs (SEM) of PRECLUDE. Magnifications (top-left to bottom-right): 136X, 281X, 1180X, 3400X, 8850X, 30830X. **k**, SEM of Teflon AF 2400. Yellow line: edge of Teflon. Magnifications (top-left to bottom-right): 42X, 387X, 1490 K X, 4460X. Each micrograph (**j**-**k**) is from a single piece of PRECLUDE (**j**) or Teflon AF 2400 (**k**). We observed a similar Teflon AF 2400 texture across 5 other independent samples. **l**, PRECLUDE and Teflon AF confocal micrographs demonstrate transparency and minimal autofluorescence of Teflon AF. Brightness and contrast matched across images in **l”**. Scale bar, 2 mm. **m**, Mean projection image from one-photon imaging of 1-µm yellow-green microspheres with or without Teflon AF; brightness and contrast matched. Scale bar, 20 µm. **n**, Two-photon imaging of the same microsphere slide as in **m**. Arrows indicate the beads used for the measurements in **o**. Scale bar, 20 µm. **o**, Profile through 10 beads matched in two-photon imaging (as in **n**) with and without Teflon AF.

https://doi.org/10.1038/s41592-024-02476-3

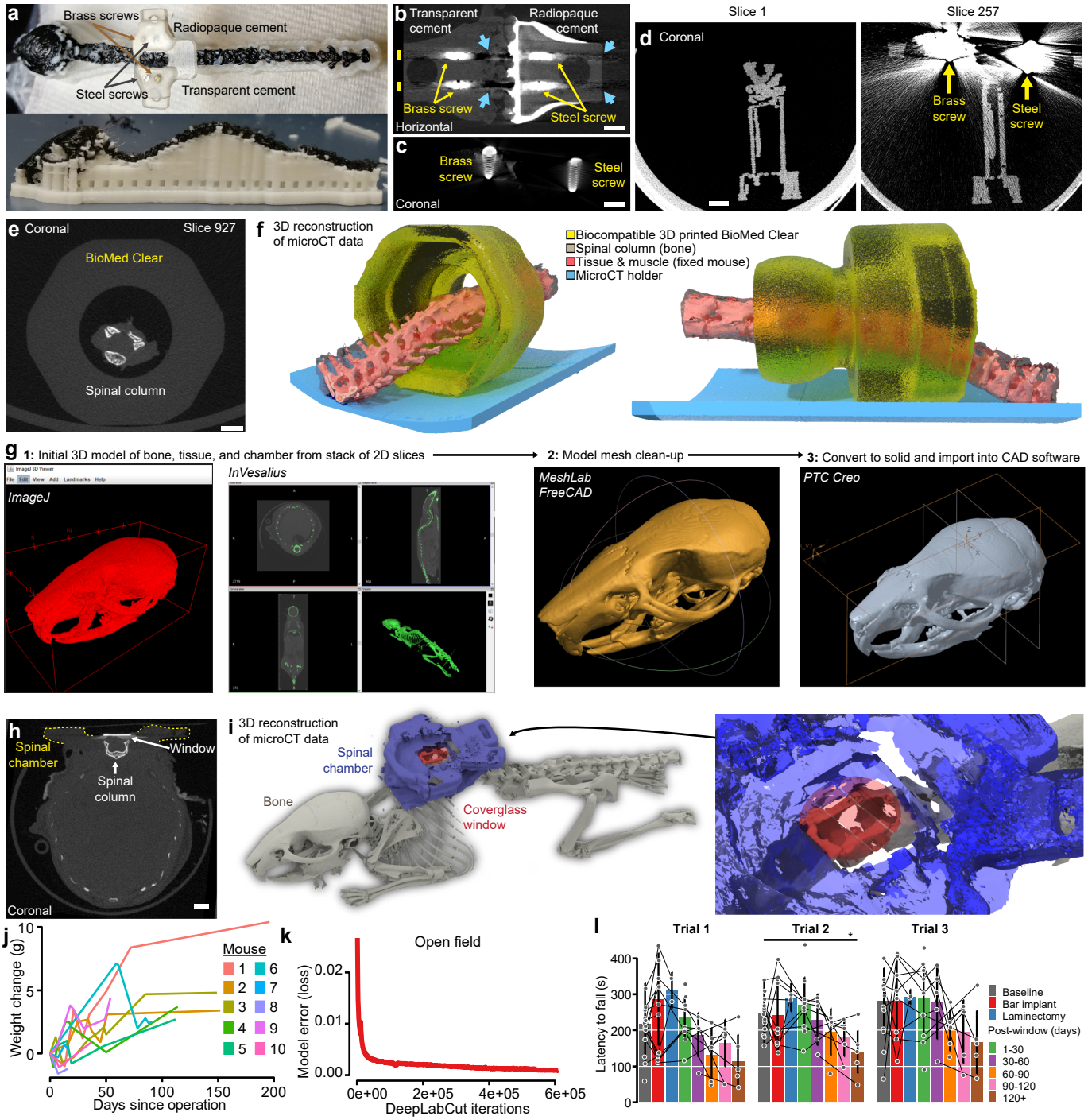


**Extended Data Fig. 3 | Validation of spinal implant with microCT, animal health, and behavior. a**, 3D printed phantom of skull and spinal column. To evaluate impact on microCT scans, a 3D printed spinal chamber (Surgical Guide) is implanted with different cements and metallic screws. **b**, Horizontal view from microCT scan of phantom in **a**. Yellow bars: acquisition planes with reconstruction artifacts due to metallic screws; cyan arrows highlight reduced reconstruction of spinal chamber and column. Scale bars, 2 mm. **c**, Coronal view of scan as in **b** shows metal screw details and artifact scan lines. Scale bars, 2 mm. **d**, Coronal sections of the phantom without (left) and with (right) metal screws in the acquisition plane. Scale bar, 2 mm. **e**, Coronal section from microCT scan (resolution: 20 µm) of a dissected mouse spinal column, placed inside a 3D printed test piece, using the same material (BioMED Clear) as for the 3D printed spinal chamber. Scale bar, 2 mm. **f**, Off-axis and sagittal views of 3D reconstructed microCT scan as in **e**. **g**, Pipeline for 3D reconstruction of microCT scans. **h**, Coronal view of mouse with 3D printed spinal chamber showing an acquisition plane at the T13 laminectomy location. Scale bar, 2 mm. **i**, 3D reconstruction of the mouse in Fig. 1h-j and h with bone (gray), spinal chamber (blue), and glass coverslip (red). Inset: magnified view highlights the T13 laminectomy and spinal chamber. **j**, Change in weight of an additional cohort of individual animals after chamber implant. Two mice, '2' and '3', are replotted from Fig. 1l. **k**, Model error (sum of score map cross-entropy and body part location L1-distance losses) as a function of DeepLabCut iterations for model trained (600,000 iterations) using data from 3 mice in an open field. **l**, Mean (per animal) latency to fall in all three trials on an accelerating rotarod, comparing naïve (n = 14) and different post-surgery times (n = 12/8/8, 2, 10, 5, 5, 5, 5). Error bars are mean ± SD. Two-way ANOVA including all trials followed by one-way ANOVA with Dunnett post-hoc per trial (one star, $P < 0.05$).

https://doi.org/10.1038/s41592-024-02476-3

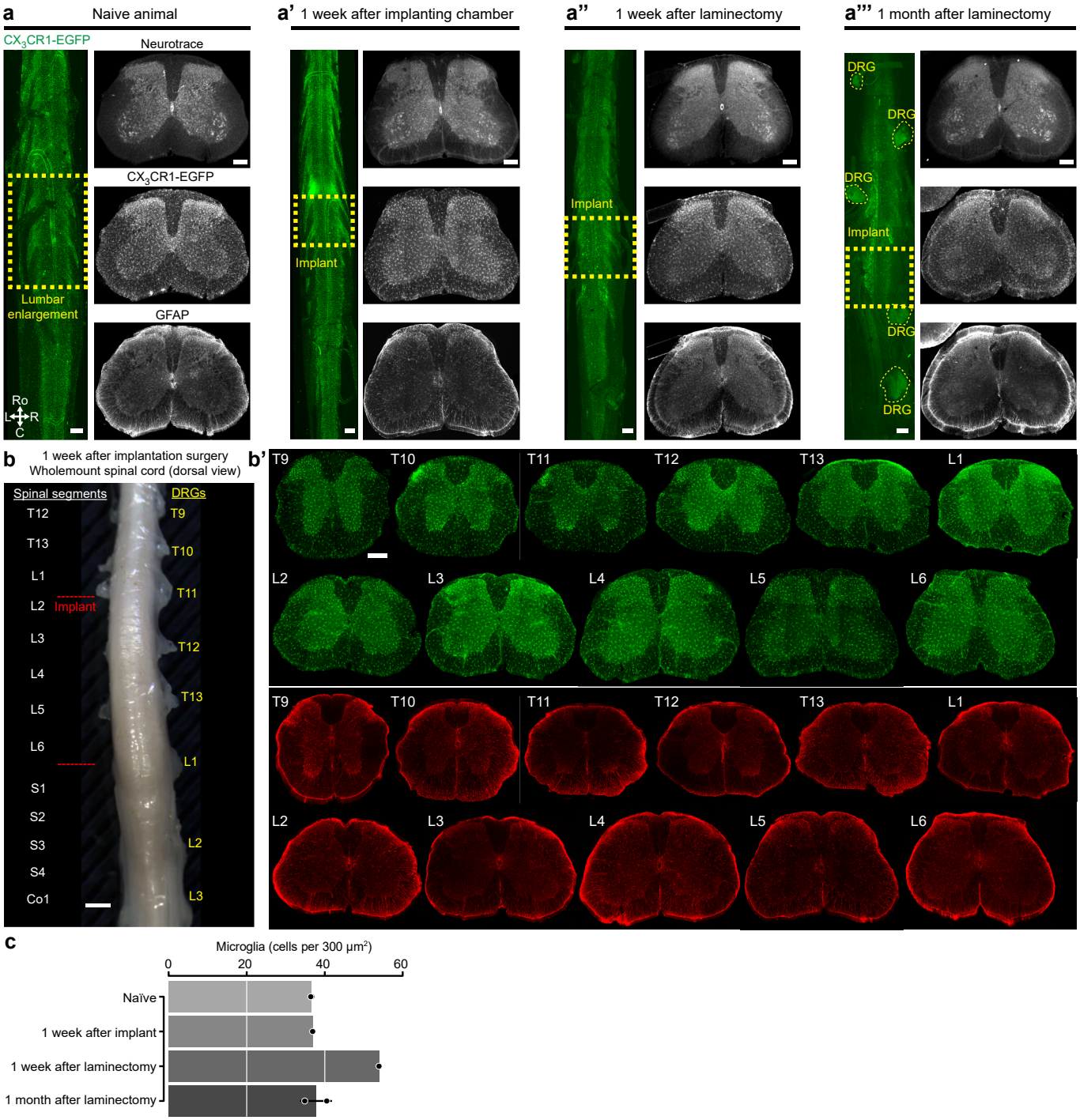


**Extended Data Fig. 4 | Histological analysis post chamber implant and laminectomy. a**, Examples of EGFP+ fluorescence in naïve (**a**) and post-surgical (**a'**, **a''**, and **a'''**) $CX_3CR1$-EGFP mouse spinal cord whole mounts and immunohistochemistry (coronal sections) with Neurotrace and anti-GFAP. Scale bars, 500 µm (whole-mount) and 200 µm (coronal slices). **b**, Spinal cord dissection and histology of a $CX_3CR1$-EGFP mouse 1 week after chamber implantation. The whole-mount image (left) shows dorsal root ganglia in relation to the implant and the associated spinal segments. **b'**, cross-sectional views of EGFP (green) and GFAP staining (red) show minimal gliosis near the implant. Scale bars, 1 mm (whole-mount) and 200 µm (coronal slices). **c**, Quantification of microgliosis in naïve mice (n = 2) along with those after spinal chamber implant (1 week, n = 1) and laminectomy (1 week, n = 1 and 1 month, n = 2).

https://doi.org/10.1038/s41592-024-02476-3

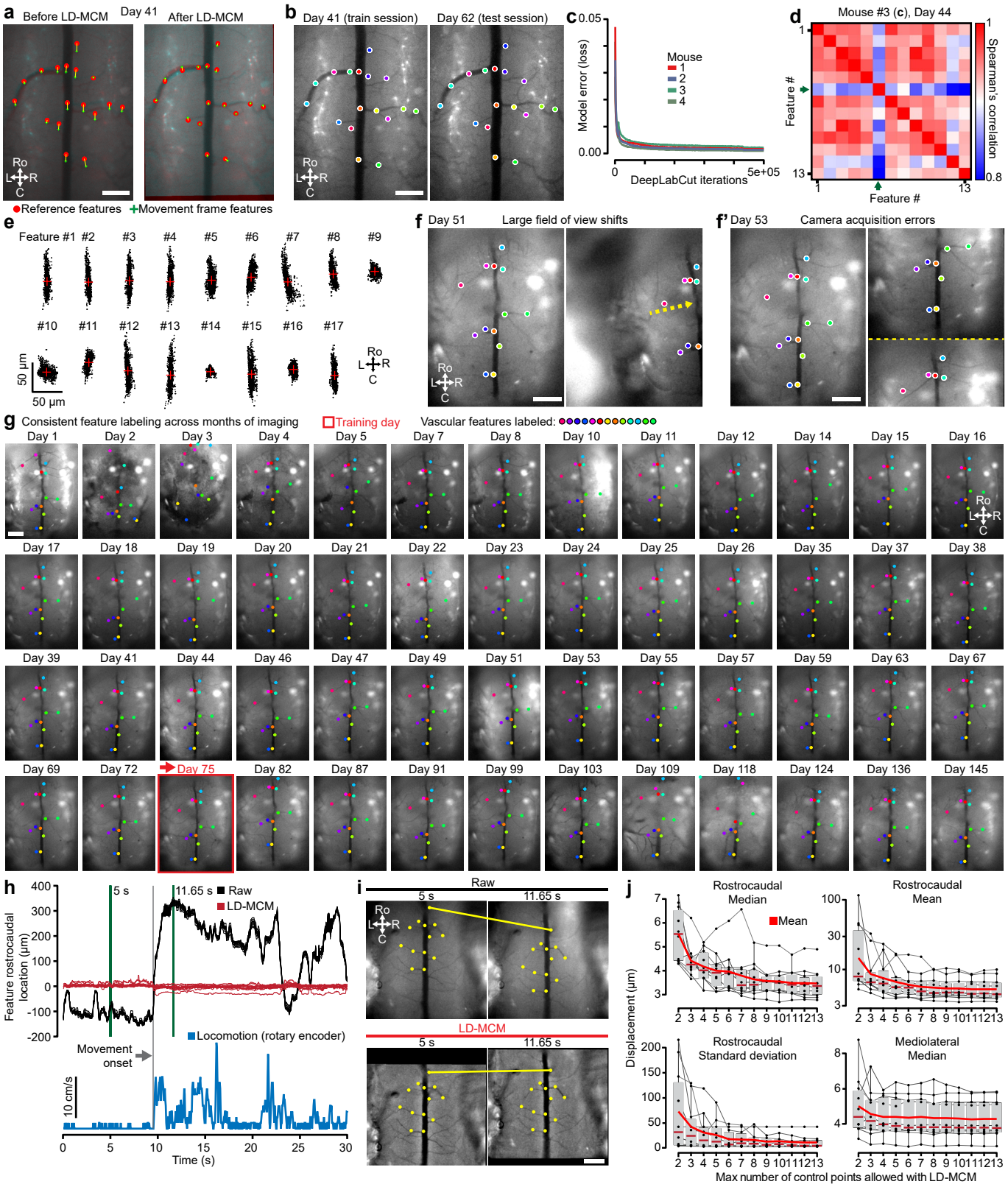


**Extended Data Fig. 5 | See next page for caption.**

https://doi.org/10.1038/s41592-024-02476-3

**Extended Data Fig. 5 | Deep-learning feature detection and control point motion correction. a**, Comparison of reference frame 42 (cyan) to movement frame 804 (red, overlaid on cyan image) before and after LD-MCM motion correction. Scale bar, 300 µm. **b**, Example of DLC-identified vascular features used for cross-session registration (DLC model trained using day 41). Scale bar, 300 µm. **c**, Model error as a function of DLC iterations (500,000 iterations, n = 4 mice). **d**, Spearman's correlation of each feature to other features in a movie from a Phox2a-Cre; Ai162 mouse. Green arrow, a feature that has reduced correlation with all other features and can thus be removed to improve motion correction. **e**, Point clouds with each dot (2001 frames) represents the rostrocaudal and mediolateral location of that feature on an individual frame during an imaging session (~6 min, 13.9 Hz, mouse from **a**). **f**, DLC tracks (1) large mediolateral shifts in the field of view (yellow arrow) and (2) camera errors that result in a split of the field of view (yellow line). Only showing features with confidence >0.1. Scale bar, 300 µm. **g**, Labeling (DeepLabCut, 20 frames from day 75) of vascular features in a Phox2a-Cre; Ai162 (GCaMP6s) mouse across 52 neural activity imaging sessions, spanning nearly 5 months. Scale bar, 300 µm. **h**, Feature locations (normalized to the session mean location) across 13 features tracked in raw and LD-MCM motion corrected movies.Green lines, frames shown in **i**. **i**, Frames before and after LD-MCM motion correction. Yellow dots: tracked features with the line showing connected features indicating improvement with LD-MCM. Scale bar, 300 µm. **j**, Performance of LD-MCM as a function of the number of features used for control point registration (n = 10 movies, n = 2 mice). Mean, median, and standard deviation calculated per movie for each combination of imaging session, parameter value, trial, and feature. Then the mean is taken across all features for the final displayed values (each data point). Boxplots in all figures display the 1st, 2nd (median), and 3rd quartiles with whiskers indicating 1.5*IQR; outliers are omitted.

https://doi.org/10.1038/s41592-024-02476-3

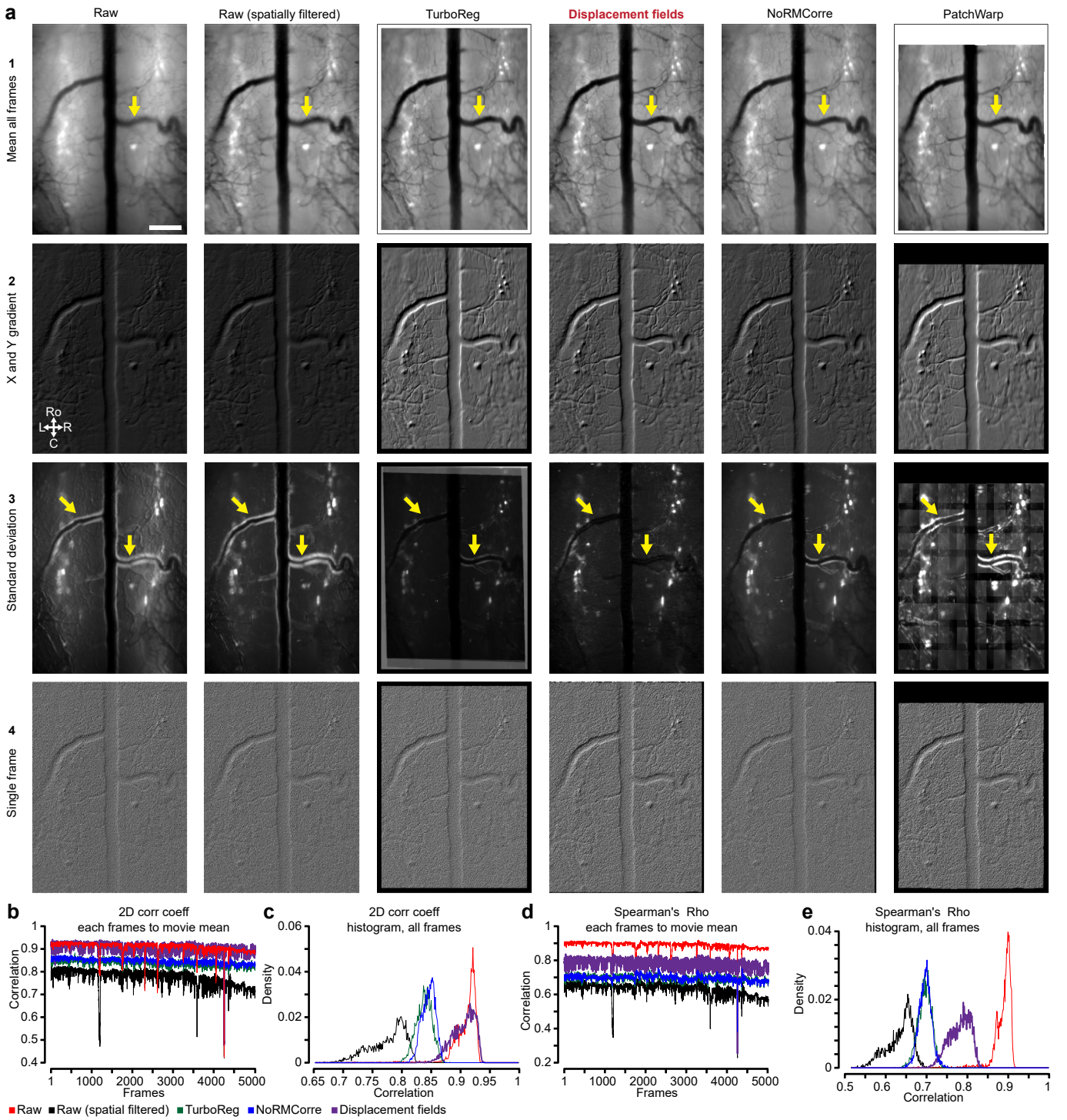


**Extended Data Fig. 6 | Deformation-based motion correction using displacement fields. a**, Each motion correction method run on the movie (5,000 frames, 13.9 Hz) from a Phox2a-Cre; Ai162 (GCaMP6s) mouse displays 1: the mean of all movie frames, 2: combined numerical gradient in both lateral directions on the mean frame, 3: the standard deviation over all movie frames (hence visibility of neurons on left and right side of the spinal cord), and 4: $\Delta F/F$ frames. Arrows indicate areas of interest where differences between methods are most evident. **b**, 2D correlation coefficient of all frames to the mean frame of the movie (as in **a**) for displacement field motion correction compared to raw, TurboReg, and NoRMCorre. All movies (except raw) were spatially filtered to remove large magnitude, low-frequency changes in fluorescence, which artificially enhances correlations. **c**, Histogram of 2D correlation coefficients over all frames from **b**. **d**, Spearman's rho of all frames to the mean frame of the movie (as in **a**) for displacement field motion correction compared to raw, TurboReg, and NoRMCorre. All movies (except raw) were spatially filtered to remove large magnitude, low-frequency changes in fluorescence, which artificially enhances correlations. **e**, Histogram of Spearman's rho values over all frames from **d**.

https://doi.org/10.1038/s41592-024-02476-3

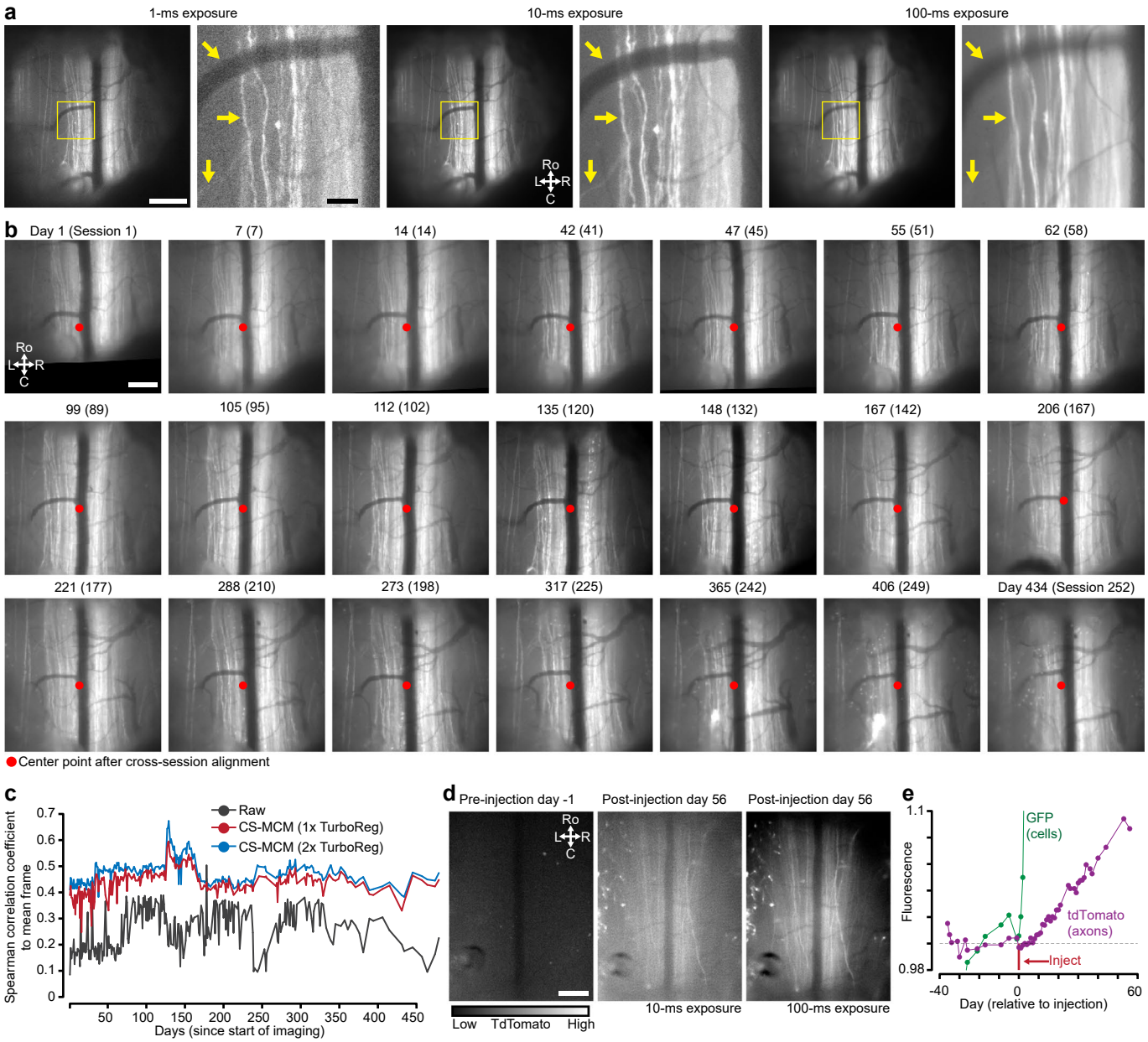


**Extended Data Fig. 7 | Long-term imaging of cell bodies and axons in the spinal cord of awake mice. a**, Clarity of GFP+ axons (Thy1-GFP mouse) with increasing sCMOS camera exposure times (LED power held constant). Yellow box: magnified section on the right. Yellow arrows: features with increased signal and minimal blur at 10-ms exposure. As a trade-off between SNR and clarity, we used 5–20-ms exposure times. Scale bars, 300 and 50 µm. **b**, Frames cropped to highlight cross-session matched areas from individual imaging sessions from a Thy1-GFP animal. Scale bar, 200 µm. **c**, Spearman correlation coefficient to the mean frame of a raw movie from a Thy1-GFP mouse (as in **b**). **d**, Increase in tdTomato expression in the dorsal columns after retro-orbital injection of AAV-PHP.S-tdTomato. Day 56, shows 10- and 100-ms exposure. Scale bar, 300 µm. **e**, Near daily imaging of GFP and tdTomato fluorescence normalized to baseline (pre retro-orbital injection). Magnified view of Fig. 3m highlights tdTomato signal increase from baseline.

https://doi.org/10.1038/s41592-024-02476-3

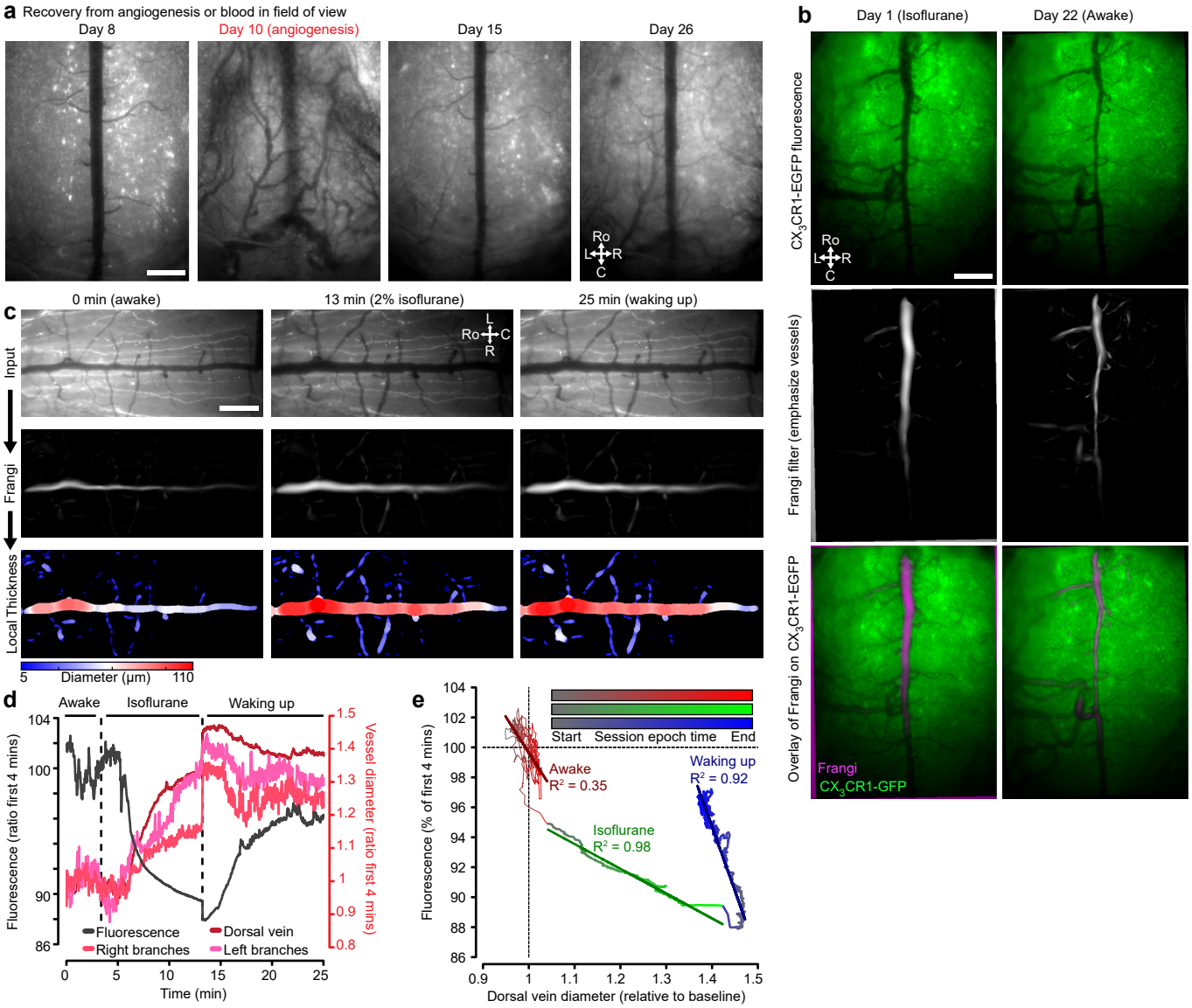


**Extended Data Fig. 8 | Transient angiogenesis and vascular dynamics in awake and anesthetized states. a**, Individual frames across imaging sessions show onset and reversal of angiogenesis in the spinal cord of a $CX_3CR1$-EGFP mouse. Scale bar, 300 µm. **b**, Change in spinal cord vessel diameter between general anesthesia and awake states in a $CX_3CR1$-EGFP mouse. Middle row illustrates the same frames after application of a Hessian-based Frangi vesselness filter that highlights the dorsal vein and a subset of dorsal ascending venules. These filtered images are used to calculate changes in vessel diameter. Scale bar, 300 µm. **c**, Procedure for determining diameter of dorsal vein and ascending venules: a Frangi filter was applied to highlight vessels and their local thickness was then calculated to determine vessel diameter. Example frames are illustrated across three major behavioral states of a Thy1-GFP mouse during a 25-min imaging session. Scale bar, 300 µm. **d**, Temporal change of vessel diameter and whole-frame fluorescence (normalized to 4-min awake baseline) within a single imaging session in a Thy1-GFP mouse before and after induction of general anesthesia (2% isoflurane). Same as Fig. 3p, but here additional right and left dorsal ascending venules are shown. **e**, Correlation of dorsal vein diameter and fluorescence during a 25-min imaging session across several behavioral states: awake (red), induction and maintenance of general anesthesia (green, isoflurane 2%), and waking up (emergence) from general anesthesia (blue). First order polynomial best-fit lines and $R^2$ indicated by darker colored lines and associated text, respectively.

https://doi.org/10.1038/s41592-024-02476-3

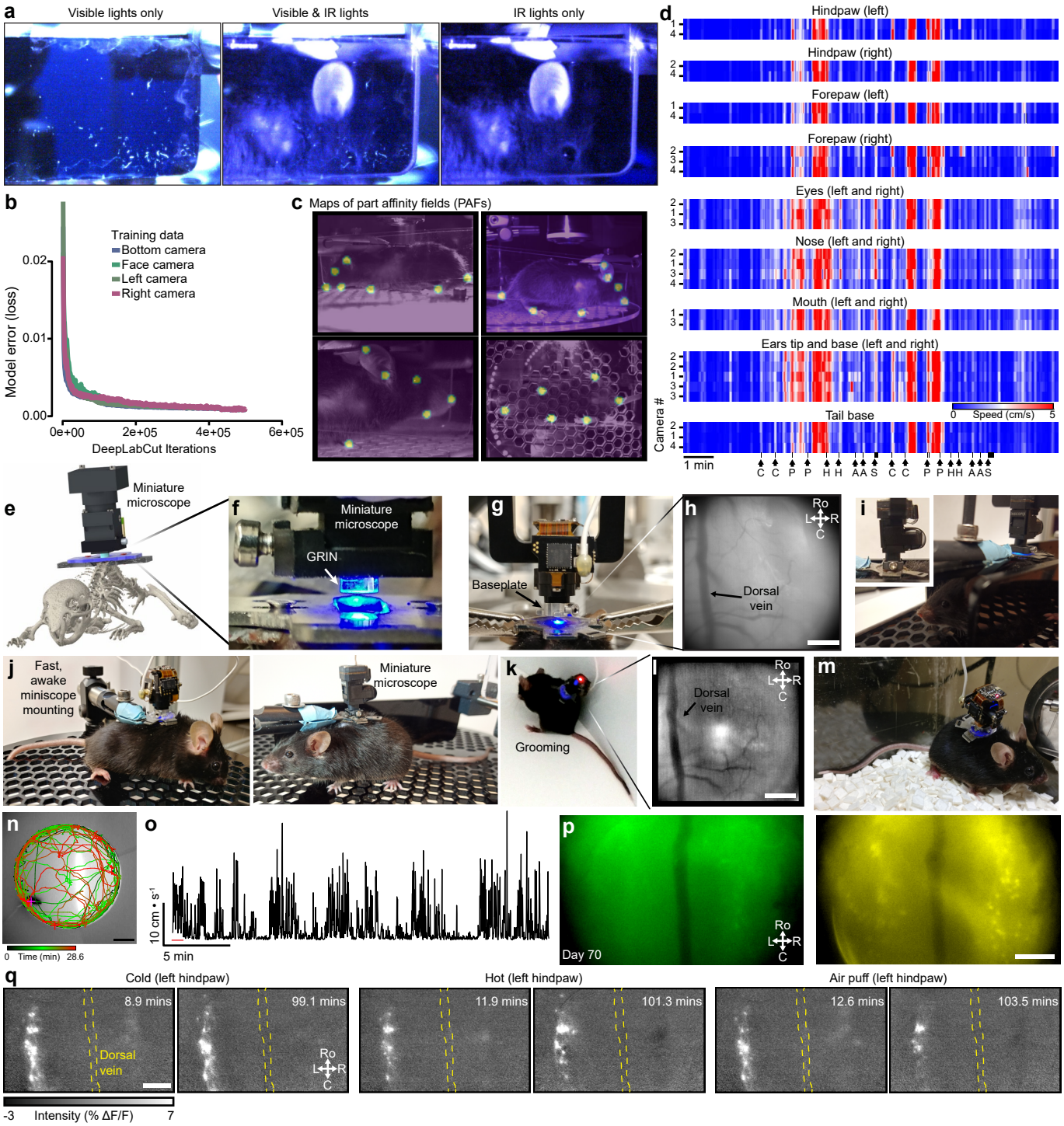


**Extended Data Fig. 9 | See next page for caption.**

https://doi.org/10.1038/s41592-024-02476-3

**Extended Data Fig. 9 | Behavior tracking of spinally fixed mice and freely moving spinal cord imaging with miniature microscopes. a**, Visibly opaque (black) infrared transmitting acrylic allows imaging of animal behavior using near-IR light sources and cameras, while blocking animal observation of experimenters (for example during stimulus delivery). **b**, Model error as a function of DeepLabCut iterations for a model trained using data from one mouse for each camera. Model training is terminated after 500,000 iterations, when the loss asymptotes. **c**, Part affinity fields for DeepLabCut networks across multiple cameras. **d**, Speed of individual body parts shows correlation of body part movement across cameras (#1–4). The mean speed across all cameras for each body part is used for display in Fig. 5g. Camera locations correspond to 1, left side of the body; 2, right side of the body; 3, right face; and 4, below the animal. Letters below each black arrow indicate the stimulus presented (C: cold; P: pinch; H; heat; A: air puff; S: sound); black bar denotes duration of the sound stimuli. **e**, 3D CAD of miniature microscope positioning above spinal implant chamber. **f**, Image of miniature microscope mounting (Inscopix, nVista). **g**, Image of miniature microscope mounting (Open Ephys, Miniscope V4.4). **h**, View of dorsal vein after procedure in **g**. Scale bar, 200 µm. **i**, Image of miniature microscope mounting in an awake animal (Inscopix, LScape module for nVue 2.0). **j**, Image of a miniature microscope mounted on the mouse using a clamp. **k**, Example of normal grooming behavior. **l**, Field of view from mouse in **k**. Scale bar, 200 µm. **m**, Ambulating mouse after mounting procedure in **g**. **n**, Locomotion of a mouse moving freely in an open field during spinal cord imaging (30 min, 10 Hz). Scale bar, 10 cm. **o**, Locomotor trace during the open field session in **n**. **p**, Multi-color miniature microscope imaging of both sides of the spinal cord 70 days after window placement in a Phox2a-Cre; Ai162 (GCaMP6s); Ai9 (tdTomato). Scale bar, 300 µm. **q**, Responses of $SCPNs^{Phox2a}$ (Phox2a-Cre; Ai162 [GCaMP6s]) to cold, hot, and air puff stimuli delivered to the left hindpaw during a ~1.8-hr continuous imaging session. Max projection of 5 s post-stimulus. Scale bar, 300 µm.

https://doi.org/10.1038/s41592-024-02476-3

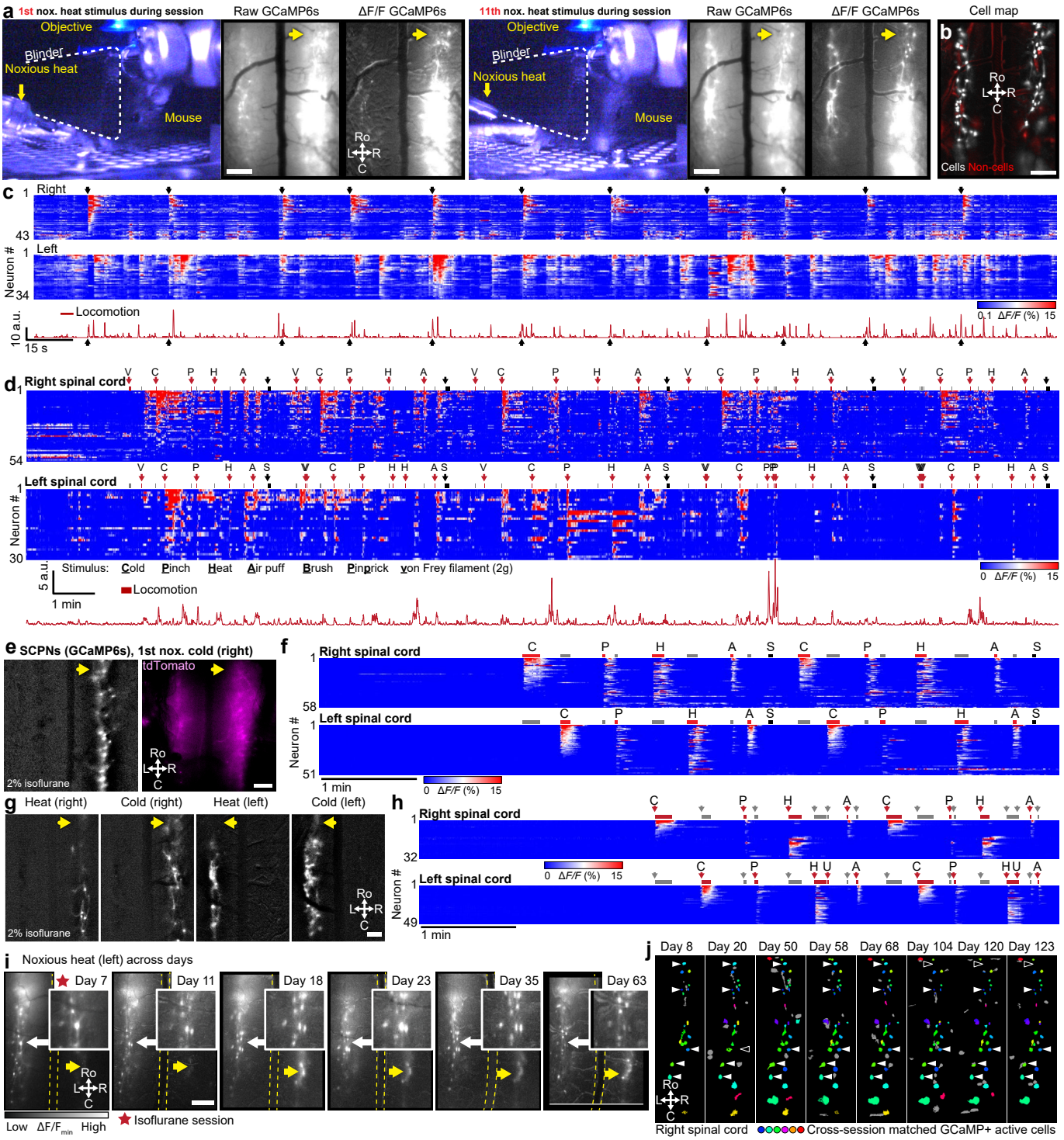


**Extended Data Fig. 10 | See next page for caption.**

https://doi.org/10.1038/s41592-024-02476-3

**Extended Data Fig. 10 | Imaging of spinal cord neuronal activity in awake and anesthetized animals. a**, Noxious stimulus-evoked SCPN$^{Phox2a}$ GCaMP6s activity in Phox2a-Cre; Ai162 (GCaMP6s) after 1st and 11th stimuli presentations in the same imaging session. Scale bar, 300 µm. **b**, Cell extraction outputs show cell (white, after manual sorting) compared to non-cell (red) outputs; the latter are excluded from further analysis. Scale bar, 300 µm. **c**, Activity of individual SCPNs$^{Phox2a}$ (GCaMP6s $\Delta F/F$), as in **a**-**b**, on the left or right spinal cord during a single imaging session (5.61 min, 13.9 Hz). Black arrows point to noxious heat applied to the right hindpaw. **d**, Extended recording session (25.47 min, 20 Hz) for mouse as in Fig. 5d–g shows SCPN$^{Phox2a}$ stimulus-evoked activity (GCaMP6s) in response to 5 blocks of stimulus applications. **e**, $\Delta F/F$ processed GCaMP6s and raw tdTomato frames from Phox2a-Cre; Ai162 (GCaMP6s); Ai9 (tdTomato) mouse under general anesthesia (2% isoflurane) shows overlap in expression. Yellow arrows in **e** and **g** indicate the side that is stimulated. Scale bar, 300 µm. **f**, Activity of individual SCPNs$^{Phox2a}$ (GCaMP6s $\Delta F/F$), as in **e**, on the left and right spinal cord during a single imaging session (7.74 min, 20 Hz) during application of various noxious and non-noxious stimuli. There is a ~2 min baseline period at the start of the session, prior to stimulus presentation. **g**, Same as **e**, except from a Phox2a-Cre; Ai162 (GCaMP6s) as in Fig. 5d-g. Scale bar, 300 µm. **h**, Same as **f**, but for the animal in **g**, during a single imaging session (6.72 min, 13.9 Hz). **i**, SCPN$^{Phox2a}$ activity (mean projection of $\Delta F/F_{min}$ post-stimulus) after noxious heat applied to the left hindpaw across imaging sessions. Yellow dotted lines: dorsal vein. Yellow arrows: consistent SCPN$^{Phox2a}$ activity contralateral to the stimulated hindpaw. Insets: white arrows indicate enlarged areas showing consistent response of the same neurons across multiple imaging sessions. Scale bar, 300 µm. **j**, SCPNs$^{Phox2a}$ extracted (CELLMax) from individual awake animal imaging sessions (except day 8, which is under anesthesia) and aligned across days. Color indicates the same cell aligned across days; filled and open arrows indicate when that particular cell is or is not identified after cell extraction across imaging sessions, respectively. Scale bars, 100 µm.

nature portfolio

Corresponding author(s): Allan Basbaum

Last updated by author(s): Jul 19, 2024

# Reporting Summary

Nature Portfolio wishes to improve the reproducibility of the work that we publish. This form provides structure for consistency and transparency in reporting. For further information on Nature Portfolio policies, see our Editorial Policies and the Editorial Policy Checklist.

## Statistics

For all statistical analyses, confirm that the following items are present in the figure legend, table legend, main text, or Methods section.

| n/a | Confirmed | |
|---|---|---|
| ☐ | ☒ | The exact sample size (*n*) for each experimental group/condition, given as a discrete number and unit of measurement |
| ☐ | ☒ | A statement on whether measurements were taken from distinct samples or whether the same sample was measured repeatedly |
| ☐ | ☒ | The statistical test(s) used AND whether they are one- or two-sided<br>*Only common tests should be described solely by name; describe more complex techniques in the Methods section.* |
| ☒ | ☐ | A description of all covariates tested |
| ☐ | ☒ | A description of any assumptions or corrections, such as tests of normality and adjustment for multiple comparisons |
| ☐ | ☒ | A full description of the statistical parameters including central tendency (e.g. means) or other basic estimates (e.g. regression coefficient) AND variation (e.g. standard deviation) or associated estimates of uncertainty (e.g. confidence intervals) |
| ☐ | ☒ | For null hypothesis testing, the test statistic (e.g. *F*, *t*, *r*) with confidence intervals, effect sizes, degrees of freedom and *P* value noted<br>*Give P values as exact values whenever suitable.* |
| ☒ | ☐ | For Bayesian analysis, information on the choice of priors and Markov chain Monte Carlo settings |
| ☒ | ☐ | For hierarchical and complex designs, identification of the appropriate level for tests and full reporting of outcomes |
| ☐ | ☒ | Estimates of effect sizes (e.g. Cohen's *d*, Pearson's *r*), indicating how they were calculated |

*Our web collection on statistics for biologists contains articles on many of the points above.*

## Software and code

Policy information about availability of computer code

| | |
|---|---|
| Data collection | We acquired one- and two-photon microscopy data using 3i SlideBook 6, Zeiss Zen (3.2.090), or µManager 2.0.0. We acquired confocal images using Olympus LSM FV3000 (2.3.2.169). Data synchronized with Saleae Logic (various iterations of version 2, e.g. 2.4.6). |
| Data analysis | We ran or compiled code in MATLAB (2022b and occasionally 2021b), Python (3.9.12) using the Anaconda (4.12.0) environment, RStudio (1.4.1106), R (4.1.0 and 4.0.2), ImageJ (1.53d), Fiji (1.53q), the Arduino IDE (1.8.13 and 2.0), and CIAtah (4.x.x). We converted between file containers (e.g. AVI to MP4) using ffmpeg (version 2020-10-21-git-289e964873). We created surgery videos using Adobe Premiere Pro. We ran image acquisition and conducted data analysis on computers running Windows 10 and, for a subset of histological images, using macOS. Code related to this study can be found at https://github.com/basbaumlab/spinal_cord_imaging and https://github.com/bahanonu/ciatah. |

For manuscripts utilizing custom algorithms or software that are central to the research but not yet described in published literature, software must be made available to editors and reviewers. We strongly encourage code deposition in a community repository (e.g. GitHub). See the Nature Portfolio guidelines for submitting code & software for further information.

## Data

Policy information about availability of data

All manuscripts must include a data availability statement. This statement should provide the following information, where applicable:

- Accession codes, unique identifiers, or web links for publicly available datasets
- A description of any restrictions on data availability
- For clinical datasets or third party data, please ensure that the statement adheres to our policy

The 3D STL and STEP files of the side bars and stabilizing plate along with a 3D model and TIFF stack of the entire mouse body from one of our microCT scans can be found at GitHub online: https://github.com/basbaumlab/spinal_cord_imaging and Zenodo (https://zenodo.org/doi/10.5281/zenodo.11660130). Any future updates to the design or additional files will be published on those repositories. Other data generated in this study are available from the authors upon request.

## Research involving human participants, their data, or biological material

Policy information about studies with human participants or human data. See also policy information about sex, gender (identity/presentation), and sexual orientation and race, ethnicity and racism.

| | |
|---|---|
| Reporting on sex and gender | N/A |
| Reporting on race, ethnicity, or other socially relevant groupings | N/A |
| Population characteristics | N/A |
| Recruitment | N/A |
| Ethics oversight | N/A |

Note that full information on the approval of the study protocol must also be provided in the manuscript.

# Field-specific reporting

Please select the one below that is the best fit for your research. If you are not sure, read the appropriate sections before making your selection.

☒ Life sciences ☐ Behavioural & social sciences ☐ Ecological, evolutionary & environmental sciences

For a reference copy of the document with all sections, see nature.com/documents/nr-reporting-summary-flat.pdf

# Life sciences study design

All studies must disclose on these points even when the disclosure is negative.

| | |
|---|---|
| Sample size | Our sample size determinant was based on prior studies (Farrar, 2012; Sekiguchi, 2016) in which similar analyses were performed. |
| Data exclusions | If an animal manifested post surgery health deterioration it was excluded from further analysis. These criteria were pre-established in our IACUC approval. |
| Replication | For the Phox2A-Cre, CXC3R1-EGFP (2 cohorts), and Thy1-GFP (2 cohorts) studies, several cohorts were studied and the results were consistent. The surgeries and experiments for each cohort were separated in time. |
| Randomization | Animals were pseudo-randomized in the few studies in which there was an experimental manipulation introduced. |
| Blinding | Blinding is not applicable in the generation of this recording method. The analysis code was run the same way across all groups. |

# Reporting for specific materials, systems and methods

We require information from authors about some types of materials, experimental systems and methods used in many studies. Here, indicate whether each material, system or method listed is relevant to your study. If you are not sure if a list item applies to your research, read the appropriate section before selecting a response.

## Materials & experimental systems

| n/a | Involved in the study |
|---|---|
| ☐ | ☒ Antibodies |
| ☒ | ☐ Eukaryotic cell lines |
| ☒ | ☐ Palaeontology and archaeology |
| ☐ | ☒ Animals and other organisms |
| ☒ | ☐ Clinical data |
| ☒ | ☐ Dual use research of concern |
| ☒ | ☐ Plants |

## Methods

| n/a | Involved in the study |
|---|---|
| ☒ | ☐ ChIP-seq |
| ☒ | ☐ Flow cytometry |
| ☒ | ☐ MRI-based neuroimaging |

# Antibodies

Antibodies used: Anti-GFAP (1:2000, #Z0334, Agilent Dako)

Validation: The following validation details for the Anti-GFAP antibody are provided by the manufacturer at https://www.agilent.com/en/product/immunohistochemistry/antibodies-controls/primary-antibodies/glial-fibrillary-acidic-protein-(concentrate)-76683.

"The antibody shows one distinct precipitate (GFAP) with cow brain extract. In indirect ELISA, the antibody shows no reaction with human plasma and cow serum."

# Animals and other research organisms

Policy information about studies involving animals; ARRIVE guidelines recommended for reporting animal research, and Sex and Gender in Research

Laboratory animals: Mice: C57BL6, Phox2a-Cre, Ai162 (JAX #031562), Ai148 (JAX #030328), Ai9 (#007909), CX3CR1-EGFP (JAX #005582), Thy1-YFP-H, and Thy1-GFP-M. Mice used in this study were ~4.9 ± 2.2 months (mean ± SD). Mice were individually or group housed with ad libitum food and water access on a 12-hr light-dark cycle at a room temperature of ~19–23°C and relative humidity of 30–70%.

Wild animals: No wild animals were used in the study.

Reporting on sex: Studies were performed in both male and female mice.

Field-collected samples: No field collected samples were used in the study.

Ethics oversight: UCSF Institutional Animal Care and Use Committee

Note that full information on the approval of the study protocol must also be provided in the manuscript.